2019

Novel strategies and multiscale modeling in respiratory mechanics

BOSTON UNIVERSITY

COLLEGE OF ENGINEERING

Dissertation

NOVEL STRATEGIES AND MULTISCALE MODELING IN RESPIRATORY MECHANICS

by

SAMER BOU JAWDE

B.E., American University of Beirut, 2013
M.S., American University of Beirut, 2014

Submitted in partial fulfillment of the

requirements for the degree of

Doctor of Philosophy

2019

Approved by

First Reader

Béla Suki, Ph.D.
Professor of Biomedical Engineering

Second Reader

Dimitrije Stamenović, Ph.D.
Professor of Biomedical Engineering
Professor of Materials Science and Engineering

Third Reader

Joe Tien, Ph.D.
Professor of Biomedical Engineering

Fourth Reader

Katherine Yanhang Zhang, Ph.D.
Professor of Mechanical Engineering
Professor of Biomedical Engineering
Professor of Materials Science and Engineering

Fifth Reader

Jason Bates, Ph.D., DSc.
Professor of Medicine, Pulmonary/Critical Care Division
University of Vermont

Knowledge: a passage through a human-constructed uneven reality

and a journey into the realm of scientific imagination.

DEDICATION

I dedicate this work to my most loving and devotional mother, Alice Joseph Rizkallah who always reminded me that "*grades are your passport*". Indeed, this journey and this thesis would not have been possible without her sacrifices, support, love and wisdom.

ACKNOWLEDGMENTS

I would like to thank the individuals who made this journey possible and enriching. First, I would like to thank Boston University's Biomedical Department for its kind and supportive community and primarily for allowing this journey to begin through accepting me to their prestigious program. No matter what words I express, I cannot describe how this acceptance and the special people I met along the journey changed my life. I will forever be grateful to: Christen Bailey, Fallon Fernandes, Alexandria Gustin, and Mathew Barber for all their administrative support, kindness, and patience with my ongoing inquiries and international student concerns. All of my first year colleagues who helped me to belong and acclimate to a world far away from home especially my sushi amigo Kavon Karrobi. My family who supported and motivated me to grow despite my long absence from home. My committee members, Professors Dimitrije Stamenović, Joe Tien, Katherine Yanhang Zhang, and Jason Bates for their constructive mentorship and feedback, and in the case of the latter, particularly for continuous in-depth feedback on manuscripts and model development. Professors and mentors including Dean Kenneth Lutchen, Bradford Smith, Francesco Vicario, and Phillip Allen for their intellectual insight and help. The Boston Dabke Troupe for the fun dancing outside research. All lab members old and new, grads and undergrads who have become part of my family for the past 5 years, and of course the two wise and devoted scientists who merged this caring family together, my research parents, Elizabeth Bartolak-Suki and Béla Suki whose passionate mentorship, relentless support, and indefinite kindness made me a better person and scientist, and last but not least Rana Akleh for her continuous patience, care, and love. Thank you!

NOVEL STRATEGIES AND MULTISCALE MODELING

IN RESPIRATORY MECHANICS

SAMER BOU JAWDE

Boston University College of Engineering, 2019

Major Professor: Béla Suki, Professor of Biomedical Engineering.

ABSTRACT

Despite tremendous technological and scientific advancements in the 20th century, clinically feasible assessment of detailed macroscopic respiratory mechanics is still limited. Additionally, a comprehensive understanding of macroscopic behavior in terms of microscopic description of alveolar mechanics and extracellular matrix properties is also absent. Combined together, these two limitations may explain why there has been a slow progress in optimizing mechanical ventilation for patients with lung disease. Addressing these two limitations, and, more importantly, linking macroscopic emergent phenomena to microscopic behavior could provide improved understanding and better health care. To this end, (1) a 3-D printed flow sensor was designed and evaluated to continuously measure airway opening flow and pressure in mice. (2) Using this sensor, we introduced a novel technique (ZVV) which provides continuous monitoring of the respiratory system's physiological condition through evaluating cycle-by-cycle respiratory impedance (Z_{RS}) during variable ventilation (VV). The feasibility and accuracy of ZVV was demonstrated by applying it in mice before and after inducing lung injury mimicking acute respiratory distress syndrome (ARDS), as well as in a computational study. Furthermore, when ZVV was applied to previously collected data, the analysis demonstrated for the first time that

VV improved lung mechanics in human patients with ARDS. Additionally, two analytical models were developed to relate macroscopic to microscopic mechanical behavior of the lung parenchyma. (3) The first alveolar-unit model related alveolar septal wall properties (i.e., thickness) and constituents (i.e., fibers) to alveolar pressure-volume relationship providing insight into the importance of calculating true stress, the role of the collagen waviness and elastic modulus in alveolar stability and protection from over distension, as well as the multiscale relation between fiber stresses and macroscopic pressures. (4) The second intermediate tissue-level model described the mechanics of alveolar wall alignment under uniaxial stretching and estimated alveolar wall stiffness and stress demonstrating its ability to extract fiber-level properties from tissue strip stress-strain relations. When applied to pressure-volume and stress-strain data from lungs of old subjects, both models predicted alveolar wall and collagen fiber stiffening in aging. In summary, this study, presented a novel technique which can assess respiratory mechanics in clinical settings and multiscale models to enhance our understanding of how macroscopic behavior is related to alveolar constituent properties.

TABLE OF CONTENTS

LIST OF TABLES

LIST OF FIGURES

LIST OF ABBREVIATIONS

ARDS	Acute respiratory distress syndrome
CV	Conventional ventilation
ECM	Extracellular matrix
FOT	Forced oscillation technique
FRC	Functional residual capacity
ID	Internal diameter
MTV	Minute ventilation
MV	Mechanical ventilation
OD	Outer diameter
OVW	Optimal ventilator waveform
PBS	Phosphate buffer solution
PEEP	Positive-end expiratory pressure
PIP	Peak inspiratory pressure
P-V	Pressure-volume
RV	Residual volume
TLC	Total lung capacity
VILI	Ventilation-induced lung injury
VV	Variable ventilation
WPI	World precision instruments
ZVV	Respiratory mechanical impedance assessed by VV

GLOSSARY OF MAJOR SYMBOLS

$CMRR$	Common model rejection ratio
δ_A	Area fraction
δ_V	Volume fraction
E_{RS}	Respiratory system elastance
F	Frequency
λ	Stretch ratio
P	Pressure
$\bar{r}^2$	Adjusted coefficient of determination
r	Deformed alveolar radius
R	Undeformed alveolar radius
R_{RS}	Respiratory system resistance
ε	Strain
σ	Stress
S	Ratio of R to inner undeformed alveolar radius (R_i)
T	Time period
V	Volume
$\dot{V}$	Flow
Z_{RS}	Respiratory system impedance
w	Collagen waviness
Y	Elastic modulus

Chapter 1: Introduction

1.1 Motivation

The human fascination in respiratory mechanics dates back as far as the 1st century AD [1]. However, it was not until the 20th century that the field greatly advanced due to technological innovations as well as the increased scientific interest [1,2]. Despite these, the optimal techniques of assessing lung mechanics, selecting ventilation settings, and describing comprehensively basic alveolar microscopic mechanics still presents several limitations. Clinically, for example, measuring respiratory impedance (Z_{RS}) is being carried out via the forced oscillation technique (FOT) which has several advantages [3] but requires special equipment, ventilation interruption, and provides measurements at nonphysiological respiratory rates and amplitudes. Furthermore, linking this macroscopic assessment to alveolar stresses and strains is key to avoiding ventilation-induced lung injury (VILI) [4]. However, establishment of such a multiscale relationship is still missing due to our limited and partial understanding of alveolar and extracellular matrix (ECM) mechanics despite decades of research [5]. As an example, the exact mechanics of how alveoli inflate are not fully comprehended and highly controversial [6–8]. Thus, the absence of a clinically personalized and optimized macroscopic assessment coupled with microscopic interpretation on one hand and the ever increasing demand and potential of mechanical ventilation (MV) on the other [9–11], motivates addressing the multiscale challenge. Therefore, in order to provide better respiratory healthcare, scientific endeavors should include a personalized strategy involving proper macroscopic assessment combined with the most informative estimation of the underlying microscopic behavior.

1.2 Hypothesis

We hypothesized that 1) an enhanced clinical assessment of respiratory mechanics at the macroscopic scale is possible using a novel analysis technique coupled with a specific ventilation modality, variable ventilation (VV), in which both frequency and tidal volume vary from breath to breath, and 2) a better understanding of how certain macroscopic lung mechanical behavior emerges from microscopic structure-function relationships, specifically from fibers embedded in the alveolar walls, could be achieved through mathematical models properly accounting for the properties of the constituents.

1.3 Aims

To test this hypothesis, four aims were set up with the primary objectives of first developing the tool needed to continuously measure respiratory mechanical variables, collecting and interpreting data during the conditions of acute respiratory distress syndrome (ARDS) and developing multiscale models that can link macroscopic mechanical behavior to microscopic structure and properties (Figure 1-1). The specific aims are:

Aim 1 (Flow sensor): To design a 3-D printed sensitive sensor for the continuous measurement of flow and tracheal pressure in mice and test the device via nonlinear modeling and subsequent experiments in mice (Figure 1-1A).

Aim 2 (ZVV): To assess respiratory mechanical impedance (Z_{RS}) during VV in a novel approach ZVV (ZVV=Z_{RS}+VV) and test ZVV in a computational study as well as in mice and human patients with ARDS (Figure 1-1B).

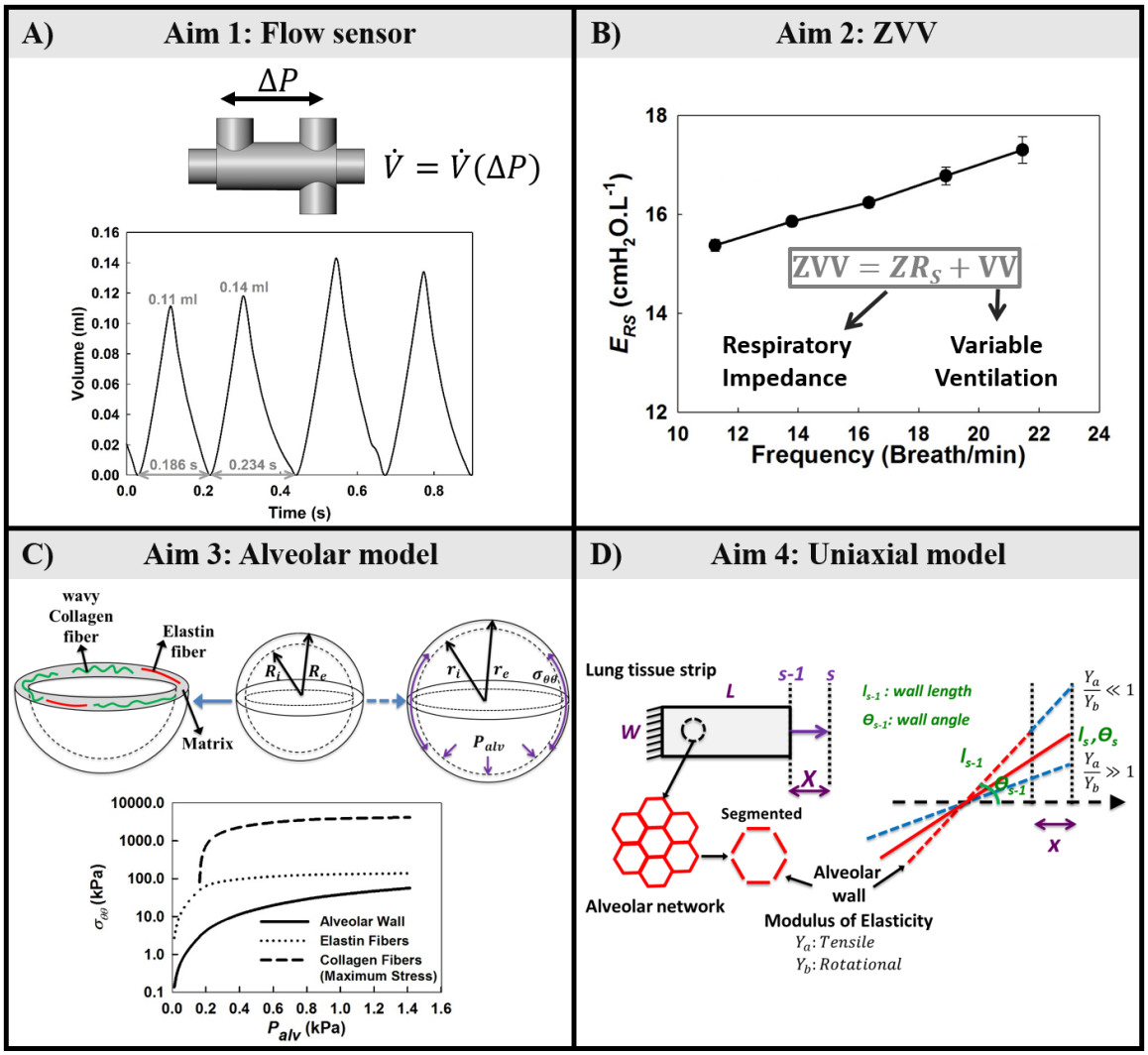

Figure 1-1: Summary of aims. A) Aim 1: Flow sensor. Given a pressure difference (ΔP) across a lab-designed and characterized flow sensor, flow ($\dot{V}$) is calculated continuously with time. An example recording of volume, obtained by integrating $\dot{V}$, is shown for the case of variable ventilation (VV) in which each breath has a different tidal volume and frequency or period. B) Aim 2: ZVV. Using the flow sensor measurements, our novel technique termed ZVV (ZVV=Z_{RS}+VV) assesses respiratory impedance (Z_{RS}) using VV. C) Aim 3: Alveolar model. The model captures how elastin (red) and wavy collagen (green) fibers embedded within the extracellular matrix (ECM) (gray) contribute to alveolar mechanics as an alveolus expands from the undeformed state with inner and outer radii R_i and Re to an arbitrary deformed state with inner and outer radii r_i and r_e respectively. The figure exemplifies the model's ability to relate microscopic alveolar and fiber circumferential stress ($\sigma_{\theta\theta}$) to alveolar pressure (P_{alv}). D) Aim 4: Uniaxial model. The model captures how an alveolar wall, embedded within a tissue of length L and width W and being stretched by incremental macroscopic displacement X from step s-1 to s, rotates and elongates based on its microscopic tensile and rotational modulus of elasticity following a microscopic displacement x.

Aim 3 (Alveolar model): To develop an analytical model of the pressure-volume (P-V) relation of a thick-walled alveolus with wavy fibers undergoing large deformation and determine key factors that protect the alveolus from over distention (Figure 1-1C).

Aim 4 (Uniaxial model): To develop an analytical model that can link alveolar wall alignment and stretching to the macroscopic uniaxial stress-strain curve and estimate separately alveolar wall tensile and rotational modulus of elasticity (Figure 1-1D).

1.4 Structure of thesis

The thesis consists of 7 chapters and 4 appendices. Chapter 1 is the introduction which presents the motivation behind this work pinpointing the need to relate respiratory microscopic mechanics to macroscopic clinical settings in order to optimize ventilation strategies. Chapter 2 provides a brief background on mechanical ventilation, the forced oscillation technique, variable ventilation, and alveolar mechanics. Chapters 3 to 6 are the 4 aforementioned aims presented in consecutive order. Chapter 3 will demonstrate the ability of a lab-designed flow sensor to accurately measure and continuously record pressure and flow in mice. Chapter 4 will present a novel strategy to assess macroscopic respiratory mechanics using data collected from the flow sensor as well as previously collected ARDS human data. Chapter 5 will transition to the microscopic scale and present a model of alveolar mechanics. It will be used to fit a P-V curve to demonstrate how the estimation of alveolar tissue and fiber stresses is plausible from macroscopic pressures. In addition, the chapter will present a new hypothesis related to the waviness of collagen fibers as key to protect the alveoli from over-distension. In support of this hypothesis

experimental waviness measurements from bovine lung tissue are presented. Chapter 6 will present a tissue-level model to separate and estimate microscopic tensile and rotational alveolar wall elastic modulus from uniaxially stretched tissue strips. The model's ability to provide physiologically-sound estimates will be achieved by computational comparison with another model and experimental fitting of controlled experiments. The model will then be used to study the effects of aging on these parameters in mice. Chapter 7 presents the final conclusions including future directions emphasizing the need of multiscale approaches towards enhancing mechanical ventilation of patients.

The four appendices, arranged in the same order as the aims, add detailed information to supplement the main chapters. Particularly, the detailed derivation of the presented models (chapters 5 and 6) are included in their respective appendices (Appendix C and D respectively).

Chapter 2: Background

2.1 Mechanical ventilation

In the early 1950s, 1500 medical students manually ventilated patients with paralytic poliomyelitis using rubber bands connected to endotracheal tubes [11,12]. After this incident decreased the mortality rate from 87% to 40% overnight [11,12], the need for mechanical ventilation (MV) motivated the invention of the first efficient ventilator in 1956 [13].

Today mechanical ventilators are readily available in the clinical setting [14], widely used [9], and the estimated need for MV is increasing [9,10]. MV is applied to assist patient breathing particularly in the case of patients with respiratory disease such as acute lung injury, chronic obstructive pulmonary disease, and acute respiratory distress syndrome (ARDS) [15,16]. Although MV has reduced mortality significantly [17,18], the rate is still high reaching 30% in 2017 in ARDS patients [18]. During MV of these patients, the lung is susceptible to ventilation-induced lung injury (VILI) due to alveolar over distension and/or cyclical opening and closing [16], which could at least in part explain the persistent high mortality rate. To minimize VILI, several different protocols rather than a unified strategy have been suggested in the literature [19–22]. This diversity is likely due to the complexity of the lung and especially its heterogeneity in diseased states [23]. Thus, there is no one-size-fits-all solution, and with the lack of personalized information to relate ventilator settings to microscopic information, avoiding VILI seems to be more of a subjective approach rather than an objective one.

2.2 Forced oscillation technique

The first step towards a personalized mechanical ventilation strategy is to diagnose the current state of the lung in the most accurate, noninvasive, and reproducible manner. Today, clinical ventilators are equipped with the ability to estimate mechanics based on several time-domain methods [24–27]. An alternative to the time domain is the frequency domain which could be a faster way to analyze respiratory mechanics without the need of any prior system modeling and the use of differential equations. Therefore, adopting such a technique can be useful. One of those strategies, which is very popular in Europe but rarely used in the United States despite demonstrating potential for measuring mechanics in children [28], is the forced oscillation technique (FOT).

In 1956, DuBois et al. [29] published the first FOT-based respiratory impedance (Z_{RS}) measurements, defined as the ratio of pressure to flow in the frequency domain, in human subjects. Using an oscillating air pump to generate sinusoidal pressure waves at the airway opening and measuring flows, Z_{RS} was reported over a frequency range of 2 to 15 Hz. It became gradually evident that Z_{RS} exhibits a strong frequency dependence at low frequencies (0.2-0.3 Hz) surrounding the spontaneous respiratory frequency (F_R) [30–34]. It is also well accepted that such data are sensitive to alterations in lung properties including heterogeneity of disease which is relevant for clinical decision making [35]. Unfortunately, while there was some success in measuring low-frequency Z_{RS} [36–38], it has remained difficult to translate it into clinical use and has rarely been utilized in mechanically ventilated patients [36,37].

Current FOT devices measure Z_{RS} utilizing low amplitude pressure oscillations at

frequencies far above F_R, usually between 2 and 32 Hz [3,39]. These FOT measurements do not provide an assessment of lung function at F_R limiting clinicians' ability to implement optimized ventilation settings and potentially hindering patient recovery. Thus, current clinical use of measuring Z_{RS} is not therapeutic, nonphysiological, intermittent, may involve patient apnea, and requires specialized FOT equipment. A technique that simultaneously addresses these limitations would significantly advance the personalized diagnosis and treatment of mechanically ventilated patients. In chapter 4, we present the development of such an approach that we term ZVV which is based on variable ventilation (VV).

2.3 Variable ventilation

VV is a relatively new approach to MV introduced in 1996 [40], where tidal volumes (V_T's) vary from one breath to another while keeping minute ventilation (MTV), defined as the product of F_R and V_T, constant. The human F_R is variable [41,42]. In fact, F_R variability is reduced during disease [43,44]. Thus, the original idea behind VV was to replicate the variability observed in human breathing [35]. Computationally, it has been shown to benefit and outperform conventional ventilation (CV), which delivers the same F_R and V_T for every breath cycle, by increasing arterial oxygenation and increasing surfactant production [45,46]. Previous studies have provided evidence of improvement in lung mechanics, gas exchange, as well as reduction in VILI injury following VV compared to CV in both healthy and injured lungs of many animal models including pigs, mice, rats, and sheep [47–60]. Clinically, VV was also shown to improve gas exchange and respiratory mechanics [61] , improve patient-ventilator synchrony [62], and reduce

inflammatory response [63]. The most likely mechanism by which VV improves lung mechanics is recruitment [46] and enhanced surfactant secretion [54,55].

Since its conception, VV has always been seen as a therapeutic method rather than a diagnostic tool, even though its potential in treating ARDS patients was recently computationally noted [64]. In chapter 4, we will demonstrate in mice and human ARDS data that VV can serve as a combined therapeutic strategy and diagnostic tool.

2.4 Alveolar mechanics

While assessing macroscopic respiratory mechanics can provide more representative clinical measurements, it remains a global one. Underlying this macroscopic measurement is an airway tree with an average of 23 generations [65] leading to an estimated 480 million gas exchange units, the alveoli [66]. Tissue mechanics at such a scale have been far less investigated due in part to the difficulty of visualizing deformations and measuring stresses and strains [67]. Consequently, it is not fully understood how the lung's macroscopic behavior relates to its microscopic constituents and, more importantly, how changes in the mechanical properties of the alveoli can lead to pathology such as VILI [68,69] or emphysema [70]. Therefore, in order capture the effects of VILI, one must understand these dynamics describing both the geometrical features as well as the constituent properties. While the alveoli are not perfectly spherical and do not have one consistent shape throughout the lung, Hansen and Ampaya [71] separated the several shapes into six different categories, and they reported that the most frequent one was three fourth of a spheroid. The inner walls of the alveoli are lined with surfactant produced by alveolar type 2 cells [72]. Below this thin liquid layer, in order, is a single layer of epithelial

cells, a basement membrane, an interstitial layer made of connective tissue, and endothelial cells which form the capillary. Particularly, it is within the interstitial layer where the elastin and collagen fibers exist. These fibers are the main load bearing elements within the alveoli maintaining the structural integrity of the alveoli and protecting it from VILI especially at high pressures. Based on their structural organization within the wall as well as their properties, these fibers will mainly dictate the alveolar stresses and strains that arise in the alveolar wall and which can cause VILI. In addition to these two load-bearing fiber networks, surfactant, by reducing surface tension, plays a role primarily in avoiding structural collapse [67,73,74].

Assessing macroscopic lung behavior, and linking it to microscopic properties, is not only needed for personalized MV, but it also provides a scientific ground to tackle several outstanding questions. In the growing field of mechanotransduction, which studies how cells respond to environmental mechanical cues, it is well documented that based on the level of stretch, the cells will behave differently [75,76]. Therefore, any cell- or tissue-based research must recreate the correct stretch magnitudes and patterns in order to accurately represent the in situ conditions. Furthermore, these stretch values that arise at the microscopic level should be connected to the static and dynamic pressure in MV since these are the settings controlled by the clinicians in medical settings or by the researchers who conduct animal experiments to develop optimized subject-specific ventilation strategies to minimize VILI. Quantitative modeling linking measurable variables during MV such as pressure and volume to stresses at the level of fibers in the alveolar walls provides the ability to better guide or find ventilation strategies. This, however, leads back

to the need of accurately measuring flow and pressure at the macroscopic level in order to access the state of the lung. With the current lack of continuous measurements from research-oriented ventilators, a necessary tool is required. Such a tool is presented in the next chapter.

Chapter 3: Flow sensor

3.1 Introduction

Measuring lung mechanical function in small animals is central to many investigations into the pathophysiology of pulmonary disease, yet it remains a challenge due to the very small gas flows involved [77,78]. For example, a key problem associated with the measurement of small flows using a pneumotachograph is the finite input impedance of any differential pressure transducer that is used to measure the resistive pressure drop across the device. This can give rise to a limited dynamic common mode rejection ratio (*CMRR*), which is a metric quantifying the ability of a device to reject common-mode signals, that causes a flow to be registered purely as a result of uniform pressure oscillations within the lumen of the pneumotachograph [79]. One approach to dealing with the problem is to use a different method for determining flow, such as from the rate of change of position of a piston within a cylinder which, with appropriate calibration for gas compression, leads to a knowledge of flow on purely geometric grounds [80]. The problem with this is that due to gas compression and pressure losses in the valves, the delivered flow into the mouse is different from the flow computed from piston motion. To estimate the delivered flow, a complex calibration procedure is required which however does not guarantee that the delivered flow is the same as the desired flow [81].

Nevertheless, the measurement of small flows with a pneumotachograph is still possible, in principle, provided any confounding dynamic and nonlinear characteristics of the device are accounted for with sufficient accuracy. Indeed, the design and implementation of flow sensors for rodents has already been shown to be feasible. For

instance, Giannella-Neto et al. [82] designed and calibrated an effective rat pneumotachograph based on rigorous design criteria considering laminar flow, measurable pressure difference, and minimal gas exchange and interference with the rodent's respiratory mechanics. In the characterization of the rat pneumotachograph, the nonlinear pressure-flow characteristics of the device were accounted for via a nonparametric polynomial model, and an important conclusion was the importance of nonlinear calibration for accurate flow measurements. To account for nonlinearities, Korenberg and Hunter [83] have shown that a Volterra series approach can be used to represent and identify a wide range of nonlinear systems. Importantly, this nonparametric modeling technique does not assume any model structure implying that nonparametric fitting does not limit the sensor model to any particular form. Furthermore, the Volterra series can account for both nonlinear as well as dynamic aspects of a small device such as a mouse pneumotachograph, providing even more precision. These properties, as well as the ability to use system memory, allows the Volterra series to provide system identification with high accuracy across a required dynamic range. Accordingly, we sought to develop a general approach to the empirical characterization of pressure-flow characteristics based on the Volterra series [83]. Furthermore, with the maturation of 3-D printing technologies, inexpensive and rapid implementation of arbitrarily detailed internal sensor structure can now be realized. This allows exploration of complex internal geometries so that sensor dead space, sensitivity, and flow resistance can be optimized. In the present study, we therefore applied the Volterra series to a 3-D printed custom-designed pneumotachograph and validated its use in measuring tracheal airflow in mice.

3.2 Methods

3.2.1 Sensor design

Figure 3-1 shows the flow sensor design, which is based on the common pneumotachograph concept where the pressure drop along a conduit is related to the axial flow within it. The conduit of our novel sensor is divided into several sections. The majority of the pressure drop along the conduit occurs across an inner core of diameter 0.5 mm and length of 5.8 mm. Outer sections having 2 mm internal diameter (ID) and 3.5 mm length allow the device to be conveniently connected into a ventilation circuit. The inner and outer sections are connected by conical sections with a diameter that increases linearly between the inner and outer sections over a length of 4.6 mm, creating an inclination angle of 9.26°. Two lateral ports (ID = 0.5 mm, outer diameter OD = 4.6mm, length = 3mm) are placed symmetrically near the wide end of each conical section to permit the measurement of differential pressure across the major resistive portion of the conduit. A single port on the outlet side of the conduit is placed for measurement of gauge pressure. The design shown in Figure 3-1 was modeled using SolidWorks 2015 (Dassault Systèmes, France) and implemented using a 3-D printer (Objet30 Scholar, resolution: 0.1mm, VeroBlack Matte, EPIC, Boston University, Boston).

The design criteria included a resistance that is large enough to produce a measurable pressure drop with the tiny flows typically encountered in mice, but not too large to significantly affect the animal's breathing pattern.

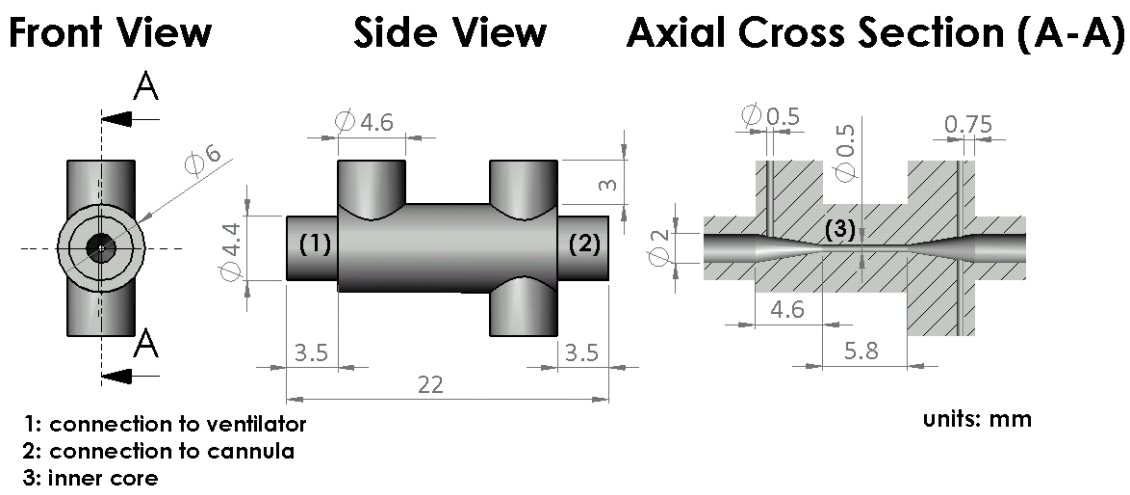

Figure 3-1: Sensor design. The sensor's front view, side view and axial cross-section view. The sensor can be connected to a ventilator on one side (1) and a mouse tracheal cannula on the other (2). The two adjacent side ports are connected to a differential pressure transducer for flow measurements, and the third side port is connected to a pressure transducer for absolute pressure measurements. The inner core (3) has a diameter of 0.5 mm spanning a length of 5.8 mm. Dimensions are in mm.

The inner volume (dead space) of the sensor was approximately 0.035 ml. The Functional Residual Capacity (FRC) of mice ranges from 0.2 to 0.5 ml [84,85] and the Total Lung Capacity (TLC) from 0.8 to 1.5 ml [85]. The dead space volume is thus only about 2 to 4% of TLC. More importantly, assuming a 25 g mouse and a tidal volume (V_T) of 8ml/kg, the dead space volume is 17.5% of the delivered V_T (0.2 ml). With this information, the ventilator settings can be adjusted (in this case to 9.7 ml/kg) to make sure that sufficient volume is delivered to the mouse for proper gas exchange.

Based on the outlined design, the differential pressure transducer only measures pressure across the inner core and the transitional regions and not the entire flow sensor. However, as later detailed, the pressure drop used to characterize the sensor is measured across its total length. Thus, for system identification to be representative and flow measurements to be accurate, it is both convenient and important that the total resistance of the sensor be due mostly to the core and the transitional region such that the pressure used to characterize the sensor and the pressure used to calculate flow from experiments closely match. Using Poiseuille's law, equivalent resistances were obtained for every region across the sensor (inlet and outlet, inner core, and the transitional region in between). For the transitional region, which had varying radii, an integration of Poiseuille equation was carried out. We found that the core and the transitional region contributed to an estimated 99.5% of the sensor's overall flow resistance (Table A-1, Appendix A). It should be noted that we assumed no flow to occur in the side ports.

The total respiratory system resistance of the mouse can vary between 0.5 and 0.8 $cmH_2O.s/ml$ [85,86]. The resistance of the flow sensor is approximately 0.9 $cmH_2O.s/ml$

and so it is of the same order as the mouse's resistance. Since the majority of the experiments use a ventilator to deliver tidal breath to the mice, the current design did not consider reducing this value by an order of magnitude. In case this is required, by simply modifying the design to have an inner diameter core of 1.1 mm reduces the resistance to around 0.0538 $cmH_2O.s/ml$ which composes 91.6% of the overall sensor resistance. The modified sensor's resistance will only be 11% and 7% of the mouse resistance respectively, while the dead space will increase to 22.7% of the delivered tidal volume. Tables A-2 and A-3 in Appendix A include the measurements and characteristics of the alternative design respectively.

3.2.2 Data acquisition

To test the device, we connected the inlet port (outer diameter, OD = 4.4 mm) via plastic tubing to a flexiVent small animal ventilator (flexiVent Legacy, Module 1, Scireq Inc., Montreal, CA), while the outlet port (OD = 4.4mm) was connected to a 20 gauge tracheal cannula. A differential pressure transducer (Biopac Systems, Model TSD160A) for recording airway flow was connected to the two symmetrical side ports by 12 mm of plastic tubing. A gauge pressure transducer (World Precision Instruments (WPI), 07B PNEU05) was connected to the single port for airway pressure measurement. The signals from both transducers were amplified (WPI, Model TBM4-F), digitized (WPI, DataTrax) at 500Hz sampling frequency and saved on a computer (WPI, Quad 16-EFA-400). The transducers were calibrated in units of cmH_2O using a water manometer.

3.2.3 Dynamic response

To identify the dynamic response of the sensor to a time-varying flow, a 16 seconds band-limited white noise volume signal comprised of sinusoidal components with frequencies between 0.5 and 20 Hz at 0.5 Hz increments, equal amplitudes, and random phases was applied to the inlet of the device using the ventilator. The signal was scaled so that the peak-to-peak amplitude in flow corresponded to a physiologically representative range for a mouse (±8 ml/s). During the volume perturbation that was delivered to the device, the pressure (P) and volume (V) signals at the inlet were also measured by the ventilator and the flow ($\dot{V}$) was obtained as the time-derivative of V using a differential filter of order 50, 22 Hz bandpass frequency, 25 Hz stop band frequency, and 256 Hz sampling frequency (F_S) (MATLAB R2015a, MathWorks, CA).

The sensor was studied in an open system configuration (no load on the outlet). To characterize the sensor parametrically, $\dot{V}$ and P were fit in MATLAB with the time-domain model:

$$P(n) = R_S\dot{V}(n) + I_S\frac{d\dot{V}(n)}{dt} \tag{3.1}$$

where R_S is sensor's resistance, I_S is sensor's inertance, and n is the data point index running from 1 to N (N=4095). To characterize the sensor nonparametrically, we first applied a nonparametric polynomial fit previously described and implemented by Giannella-Neto et al. [82] and Tang et al. [87]. Briefly, V can be written as the integral of $\dot{V}$:

$$V(n) = \frac{1}{F_S}\sum_{i=1}^{n}\dot{V}(i) \tag{3.2}$$

If $\dot{V}$ is assumed to be a polynomial function of ΔP with order m then:

$$\dot{V}(n) = c_1 P(n) + c_2 P(n)^2 + \cdots + c_m P(n)^m \tag{3.3}$$

and:

$$V(n) = \frac{1}{F_S}\sum_{i=1}^{n}\dot{V}(n) = \frac{c_1}{F_S}\sum_{i=1}^{n}P(i) + \frac{c_2}{F_S}\sum_{i=1}^{n}P(i)^2 + \ldots + \frac{c_m}{F_S}\sum_{i=1}^{n}P(i)^m \tag{3.4}$$

In vector form this is written as:

$$\boldsymbol{V} = \frac{1}{F_S}\boldsymbol{X}\boldsymbol{C} + \boldsymbol{B} \tag{3.5}$$

where $\boldsymbol{C}$ is an m x 1 column vector with the polynomial coefficients c_1 to c_m, $\boldsymbol{X}$ is an N x m matrix whose columns are increasing powers of P evaluated at time points i=1…n, and $\boldsymbol{B}$, a column vector of length N, is the error. $\boldsymbol{C}$ can be estimated as:

$$\boldsymbol{C} = (\boldsymbol{X}'\boldsymbol{X})^{-1}\boldsymbol{X}'\boldsymbol{V}F_S \tag{3.6}$$

where $\boldsymbol{X}'$ is the transpose of $\boldsymbol{X}$.

The last fitting technique included the nonparametric Volterra series up to 3rd-order. A 3rd-order series is written as:

$$\dot{V}(n) = h_0 + \sum_{i=1}^{M} h_1(i)\, P(n-i+1) + \sum_{i_1=1}^{M}\sum_{i_2=1}^{M} h_2(i_1,i_2)\, P(n-i_1+1)P(n-i_2+1) + \sum_{i_1=1}^{M}\sum_{i_2=1}^{M}\sum_{i_3=1}^{M} h_3(i_1,i_2,i_3)\, P(n-i_1+1)P(n-i_2+1)\Delta P(n-i_3+1) \quad (3.7)$$

where h_j is the Volterra kernel of order j. These kernels were identified using the approach of Korenberg and Hunter [83,88]. M represents the system's memory, and n goes from M to N. For example, if M=6, then n=6, 7… N and $\dot{V}$ is calculated using the current and 5 previous P values; for the 1st $\dot{V}$ value calculated (n=6), $h_1(1)$ will be multiplied with the current P value, $P(6)$, while $h_1(6)$ will be multiplied by the 1st P value, $P(1)$.

To briefly summarize the method, Eq. 3.7 was written in the following form:

$$y(n) = \sum_{m=0}^{M-1} a_m p_m(n) + e(n) \quad (3.8)$$

where $y(n)$ are the measured flow values $\dot{V}(n)$, the parameters a_m correspond to the individual Volterra kernels, p_m is related to the input $P(n)$ including higher order and cross-term multiplications, and e is the error. First, p_m was computed from $P(n)$ and was used to construct orthogonal functions via a modified Gram-Schmidt procedure [89]. These orthogonal functions were then used in a least square fit and the a_m values were calculated through a recursive procedure. The 1-D matrix a_m contains all kernel values arranged from the lowest to the highest order (i.e. a_o is the zero-order kernel) [83,88]. For a 3rd order

Volterra series, the zero-order kernel h_0 is a single value, the 1st order kernel h_1 is a 1-D matrix of size M, the 2nd order kernel h_2 is a 2-D symmetric matrix of size M x M, and the 3rd order kernel h_3 is a 3-D matrix of size M x M x M. Any non-zero elements from h_2 and h_3 signify nonlinearity due to interactions between P terms.

The main difference between the system identification techniques embodied in Eq. 3.1, Eq. 3.3, and Eq. 3.7 is that the first is a linear parametric model without memory and with parameters that can be related to physical quantities such as radius and length. The second approach is nonlinear and nonparametric but without memory while the last one also has memory, is nonlinear and nonparametric. Thus, the parameters in Eq. 3.3 and Eq. 3.7 have no direct physical interpretation.

We used the fitting parameters identified in Eqs. 3.1, 3.3, and 3.7 to predict flow ($\dot{V}_{fit}$) from P for comparison to $\dot{V}$ recorded by the ventilator. This comparison was quantified by the adjusted coefficient of determination ($\bar{r}^2$) given by:

$$\bar{r}^2 = 1 - \frac{N-1}{N-c-1}\frac{\sum_i^N(\dot{V}_{fit}(i) - \dot{V}(i))^2}{\sum_i^N(\dot{V}(i) - \bar{\dot{V}})^2} \tag{3.9}$$

where c is the number of coefficients (equal to the number of parameters in the parametric and polynomial fits or the number of unique kernels in the Volterra series) and the bar above $\dot{V}$ denotes the average. Finally, to confirm that the improved Volterra series performance is due to their enhanced ability to describe dynamic systems rather than noise, we applied a simple cross-validation exercise for all 3 techniques in which we fitted half the data and used the other half for validation and compared the $\bar{r}^2$ values as well.

3.2.4 Common mode rejection ratio

The *CMRR* of the differential pressure transducer connected to the flow sensor was determined using composite volume perturbations containing 5 frequencies (2, 5, 11, 19 and 31 Hz) based on the non-sum non-difference criterion [90] with peak-to-peak amplitudes of 2 and 4ml/kg. The two ports of the differential pressure transducer in each configuration were exposed to the same dynamic pressure excursions while a separate pressure transducer measured these pressure excursions relative to atmosphere (P_1). Using P_1 and the measured differential pressure across the sensor (P_2), *CMRR* was calculated as a function of frequency (F):

$$CMRR(F) = 20\log_{10}\left[\frac{P_1(F)}{P_2(F)}\right] \tag{3.10}$$

where $P_1(F)$ and $P_2(F)$ are the Fourier transforms of P_1 and P_2 respectively.

3.2.5 Mouse experiments

The experimental protocol was approved by the Institutional Animal Care and Use Committee of Boston University. The flow sensor was used in two sets of experiments to evaluate its performance. Before each experiment, the ventilator together with the flow sensor and tracheal cannula attached were calibrated for their combined internal airflow resistance, inertance and gas compressibility. Mice (C57BL/6) were anaesthetized with an intraperitoneal injection of Nembutal (80 mg/kg). Depth of anesthesia was confirmed by absence of response to toe pinch. Mice were then tracheostomized and attached to the ventilator.

In one set of experiments, and after a period of ventilation, the spontaneous

breathing patterns of two anesthetized mice (both weighing 23 g) were recorded for up to 2 minutes. Tidal volume (V_T), respiratory frequency (F_R) and their product, minute ventilation (MTV), was calculated for every breath from the recorded signals. In a second set of experiments, mice (n =5, 29.8±2.0 g) were ventilated at 8 ml/kg using variable ventilation (VV) such that each breath delivered a different V_T with its F_R adjusted so that MTV remains the same for every breath. V_T was selected randomly from a power-law distribution as described previously [47]. After delivery of 10 min VV, mice were disconnected from the ventilator and the lungs were lavaged with 0.1 ml warm phosphate-buffered saline (PBS) instilled into the trachea. VV was then resumed with the same settings for 20 min. In order to assess the ventilator's ability to deliver the prescribed tidal volume per weight (8 ml/kg), the mean value of V_T ($\bar{V}_T$), computed by the sensor during VV before and after lavage, was compared to the prescribed V_T (V_P).

It is worth pointing out that the purpose of the lavage was two-folds. First, it was used to assess our flow sensor's ability to measure small flows, and second, to capture changes in respiratory resistance and elastance in an ARDS mouse model using our novel strategy, ZVV, which is the topic of the next chapter.

3.2.6 Data analysis

All data analyses were performed using MATLAB. A paired t-test was used to assess the effect of lavage treatment on $\bar{V}_T$. Individual V_T measurements before and after lavage were compared using the rank-sum test. Statistical significance was accepted at $p < 0.05$.

3.3 Results

3.3.1 Dynamic response

The pressure-flow characteristics of the flow sensor were well characterized both parametrically ($\bar{r}^2$=0.9591) and nonparametrically ($\bar{r}^2$=0.975, 0.977, and 0.994 for the 1st, 2nd, and 3rd order respectively and 0.9147 for the polynomial fit) as illustrated in Figure 3-2. For the parametric fit, the values of R_S and I_S were 0.5758 $cmH_2O.s.ml^{-1}$ and 0.0015 $cmH_2O.s^2.ml^{-1}$, respectively. For the 3rd order nonparametric polynomial fit, the values of c_1 , c_2 and c_3 were 1.7920 $ml.s.cmH_2O^{-1}$, 0.00224 $ml.s.cmH_2O^{-2}$, and -0.0193 $ml.s.cmH_2O^{-3}$ respectively. For the 3rd order Volterra fit, h_o was equal to 0.4914 $ml.s^{-1}$ while $h_1$was given by the vector of values (0.654, 1.390, -0.598, 1.601, 1.273, 0.2832) $ml.s^{-1}cmH_2O^{-1}$ where the 1st component in this vector is $h_1(1)$. The fact that $h_1(1)$ is smaller in magnitude than several other components signifies that flow depends much more on some previous P values than on the current one. The h_2 values are shown in Figure 3-3A, and a selected slice for $h_3(i_1, i_2, 6)$, where i_1 and i_2 vary from 1 to 6, are shown in Figure 3-3B. The contour plots in Figure 3-3 demonstrate two main features. First, there are high absolute kernel values along the main diagonal that reflect a nonlinear dependence of flow on the current and previous pressure values individually (i.e., without cross-interactions). Second, there are also high absolute kernel values off the main diagonal with values comparable to those on the diagonal, showing that flow has a nonlinear dependence on cross-interactions between both current and past values of pressure. The values of these kernels are presented as supplementary data in Table A-4 (Appendix A).

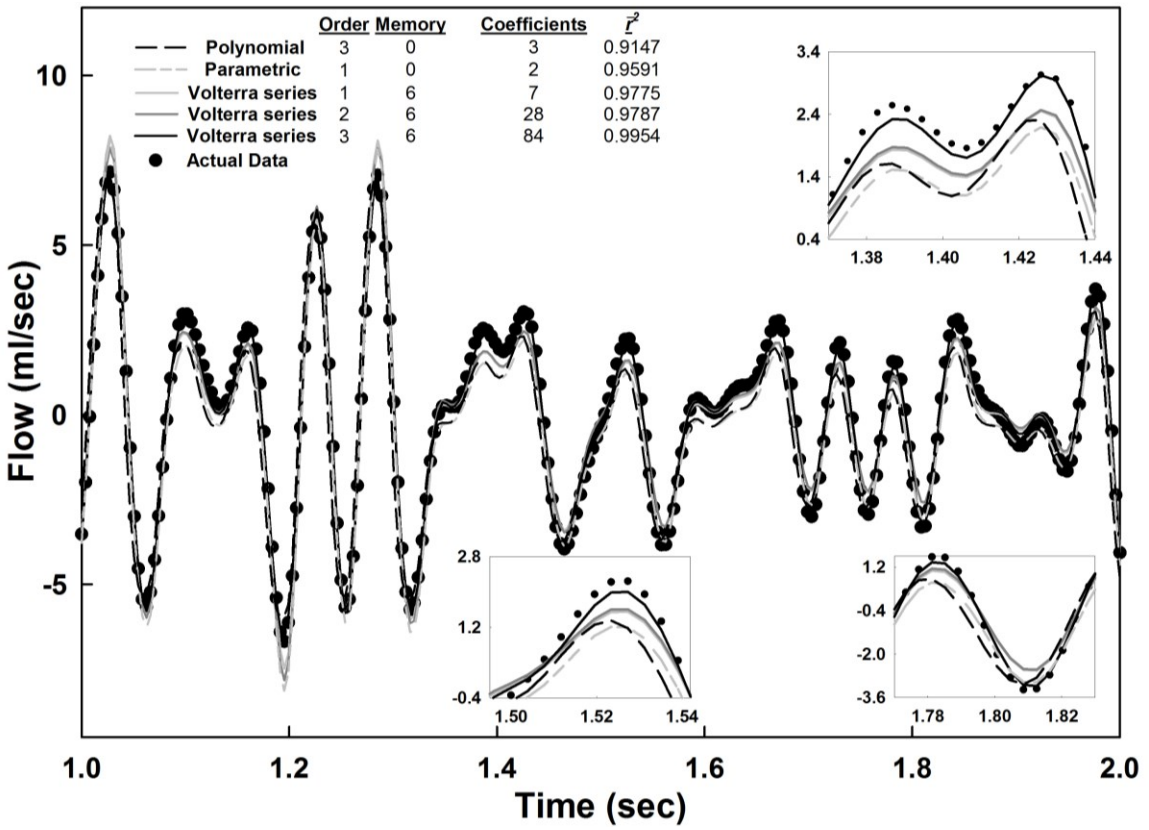

Figure 3-2: Sensor's dynamic response. Ventilator (circles) and fitted flow (lines). The parametric fit (dashed light gray), polynomial fit (dashed dark gray) and the nonparametric fits (medium gray, dark gray and black solid lines) captured the prescribed flow well. The fits of the Volterra nonparametric model were slightly better with higher adjusted $\bar{r}^2$ values (>0.97) compared to 0.9591 for the parametric model and 0.9147 for the polynomial model. The parametric and polynomial model fits tended to overshoot or undershoot the actual data at the extremities, and observing the insets, the 3rd order Volterra series (solid black line) was the most accurate in following the actual data. One second of the total 16 second signal is shown.

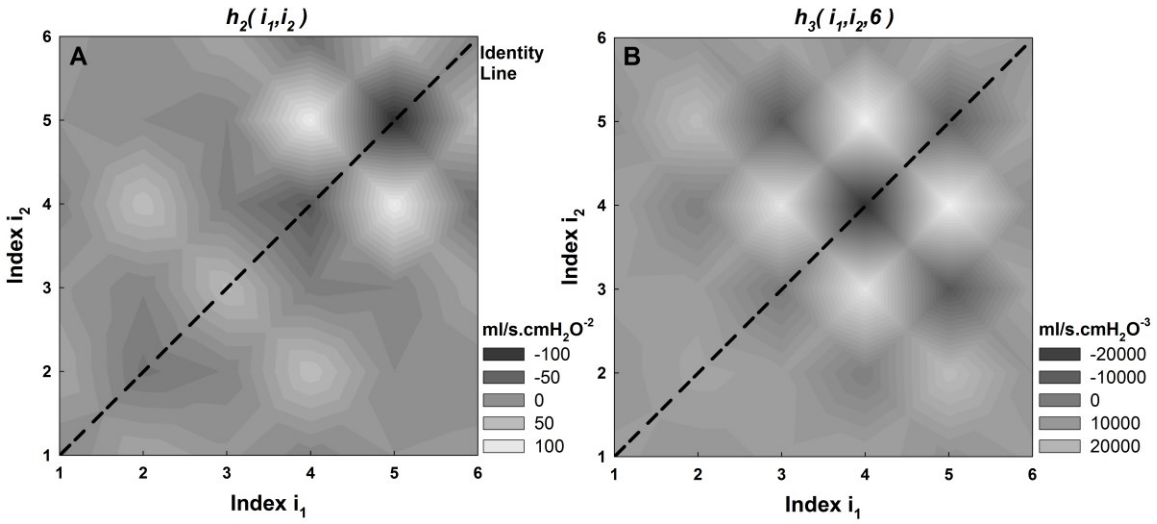

Figure 3-3: Kernel contour plots. Contour plots for 2nd order kernels (h_2) (Panel A) and a selected slice of the 3rd order kernels ($h_3(i_1, i_2, 6)$) (Panel B). The Volterra kernels are symmetric ($h_2(i_1, i_2) = h_2(i_2, i_1)$ and $h_3(i_1, i_2, k = 1{:}6) = h_3(i_2, i_1, k = 1{:}6)$ as can be seen using identity line (black dashed line). The contour plots show the extent of nonlinear behavior within the system. For instance, the current flow value highly depends on the square of the 3rd and 4th previous *P* values since the contour shows high kernel values at that location $h_2(4, 4)$ and $h_2(5, 5)$ respectively. The absolute values of $h_2(5, 4)$ and $h_2(4, 5)$ are also high and the current flow value has high nonlinear dependence on the kernels and thus the interaction of the 3rd and the 4th previous *P* values. Similarly, $h_3(3, 3, 6)$ and $h_3(4, 4, 6)$ show a cubic flow dependence on the 2nd and 3rd previous *P* values, respectively, while $h_3(3, 4, 6)$ and $h_3(4, 3, 6)$ show a nonlinear dependence of flow on the interaction of the 2nd and 3rd previous *P* values with the previous 5th *P* value (since *k*=6). Kernel values are presented in Table A-4 (Appendix A).

When cross-validation was applied using the 1st, 2nd, and 3rd order Volterra series, the $\bar{r}^2$ on the first half of the data were equal to 0.9771, 0.9786, and 0.9953, respectively. The same respective $\bar{r}^2$ values during the prediction on the second half of the data were 0.9717, 9723, and 0.9886. As expected the latter values are slightly smaller than the former; however, these $\bar{r}^2$ values are still close to 1. More importantly, they exceed the $\bar{r}^2$ of the other fitting techniques following cross-validation: for the parametric fit, the fitting $\bar{r}^2$ was 0.9597 while the validation $\bar{r}^2$ decreased to 0.9586 whereas for the polynomial the $\bar{r}^2$ slightly decreased from 0.9147 to 0.9145.

Figure 3-4 demonstrates that the *CMRR* of the differential pressure transducer combined with the flow sensor was above 40 dB at and below the mouse's breathing frequency (1-5 Hz) [91]. Furthermore, the results for 2ml/kg and 4ml/kg are virtually identical throughout the frequency range indicating that *CMRR* is independent of the delivered tidal volume.

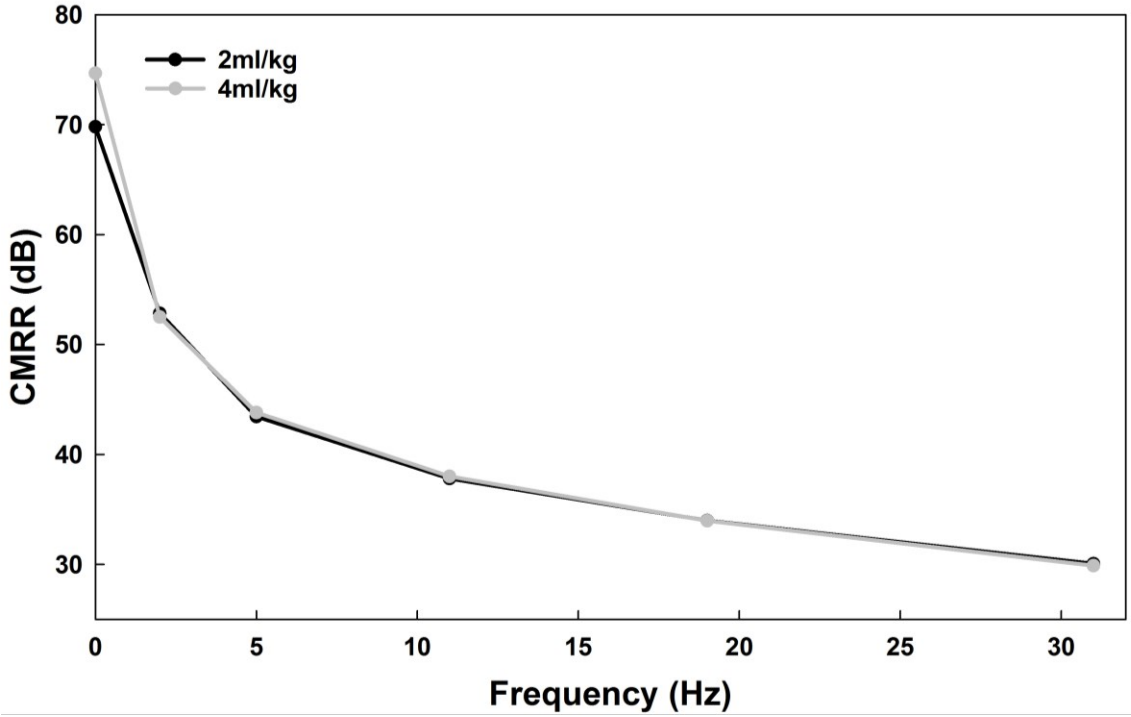

Figure 3-4: Sensor *CMRR*. *CMRR* as a function of frequency at 2 (black) and 4 (gray) ml/kg tidal volume using a composite volume perturbation containing 5 frequencies between 2 and 31 Hz. The curves represent the *CMRR* of the differential transducer connected to the sensor and the amplifier.

3.3.2 Mouse experiments

Figure 3-5A shows examples of volume recorded from two spontaneously breathing anaesthetized mice following a period of ventilation. The total number of cycles were divided into groups consisting of 13 consecutive breaths and for each group the average values for V_T, F_R, and MTV are plotted as functions of time in Figures 3-5B, 3-5C, and 3-5D respectively. Both mice showed increasing V_T over time; however, F_R in mouse 2 was fairly steady whereas F_R in mouse 1 displayed a sudden decreasing trend after 1 min. This resulted in a plateau in MTV in mouse 2 whereas F_R continuously increased in mouse 1.

In the mechanically ventilated mouse experiments, the natural breathing pattern of the mouse was overridden by the ventilator. Figure 3-6 shows an example of the measured VV pattern in a mouse highlighting breath-to-breath variability of both V_T and F_R. Table 1 shows the statistics on $\bar{V}_T$ primarily indicating its deviation from V_P and the ventilator's inability to deliver the prescribed volume in both healthy and injured lungs. Thus, generally, the delivered V_T was considerably lower than the prescribed in all mice both before and after lavage. Furthermore, there was an additional discrepancy in comparing $\overline{V}_T$ before and after lavage. Four out of the five mice showed a decreased V_T after lavage compared to before lavage and this was statistically significant in three mice.

At the end of the experiments, the mice responded to the toe pinch test and spontaneous breathing was observed due to chest wall movement suggesting that the sensor was tolerated and the data collected is viable for analysis.

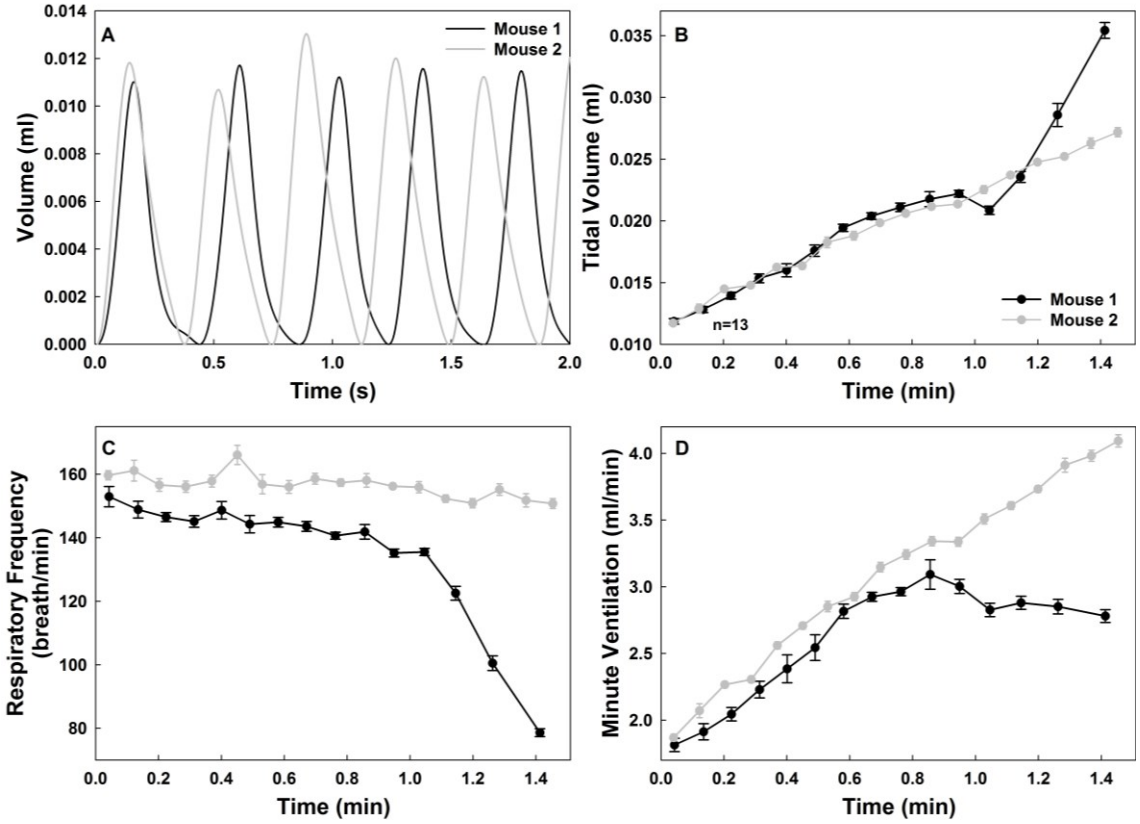

Figure 3-5: Measurements during spontaneous breathing. A) Two seconds of measured tidal excursions. Time analysis results for B) tidal volume, C) respiratory frequency, and D) minute ventilation. Every time point represents the mean and standard error of 13 consecutive breaths. The volume was obtained by integration of the estimated flow.

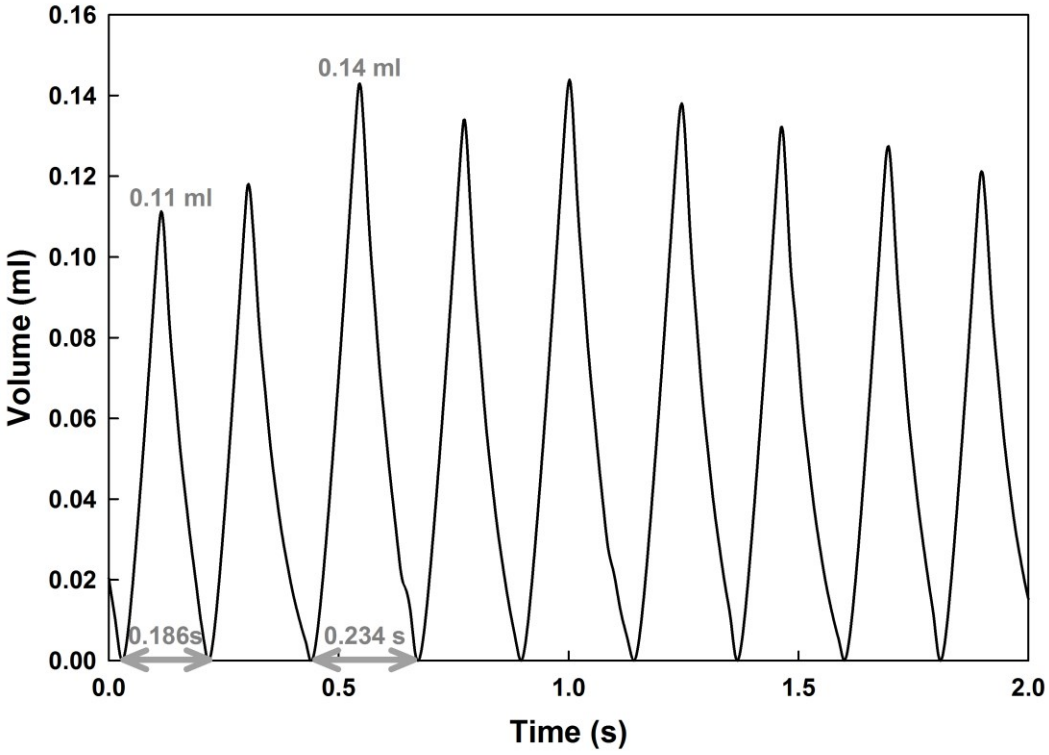

Figure 3-6: Measured lung volume changes during mechanical ventilation. The flow sensor was able to continuously record the flow waveform data. Shown is a 2 second demonstration of a measured variable ventilation pattern in which the tidal volume delivered changes with every breath. The tidal volume as well as the breath duration of two cycles are shown (gray). A larger tidal volume (0.14 ml) is delivered during a longer time (0.234 s) compared to a smaller tidal breath (0.11 ml) delivered in a shorter period (0.186 s). However, the minute ventilation (Tidal Volume/Breath Duration) for the two breaths is the same (0.59 ml.s^{-1}). The volume was obtained by integration of the estimated flow.

Table 3-1: Statistical Comparison on V_T before and after lavage.

n	w	Vp	V_T Before Lavage					V_T After Lavage					p
			$\bar{V}_T$	rV	Mn	25%	75%	$\bar{V}_T$	rV	Mn	25%	75%	
1	33.6	0.27	0.12	44	0.109	0.094	0.130	0.11	42	0.107	0.090	0.127	**<0.001**
2	27.8	0.22	0.16	71	0.149	0.130	0.172	0.16	70	0.147	0.127	0.172	0.1094
3	28.9	0.23	0.14	60	0.127	0.112	0.149	0.14	61	0.132	0.114	0.155	**0.0017**
4	29.7	0.24	0.15	65	0.144	0.128	0.167	0.15	62	0.138	0.119	0.164	**<0.001**
5	28.7	0.23	0.15	67	0.143	0.124	0.165	0.15	65	0.140	0.120	0.166	**0.0141**

n: mouse number, w: weight (gm), Vp: prescribed tidal volume (ml), $\bar{V}_T$: mean tidal volume (ml), rV= $\bar{V}_T$/ Vp (%), Mn: median, p: p-value (rank-sum).

3.4 Discussion

The aim of this study was to design, model, and test a simple 3-D printed flow sensor. The design is easily adjustable, scalable, and rapidly printable through the use of 3-D printing technology allowing researchers to optimize the design based on their needs, available tools, and the specifications of their equipment (i.e., transducer sensitivity). More importantly, the Volterra approach provides an accurate and general characterization of the behavior of the sensor, allowing tracheal airflow to be measured in living mice.

3.4.1 Dynamic response

The sensor displayed dynamic nonlinear behavior (Figure 3-2) which explains why the selected nonparametric Volterra series outperformed the parametric and the polynomial models as demonstrated by the higher $\bar{r}^2$ values. Despite the fact that the $\bar{r}^2$ values are close to each other, the insets in Figure 3-2 reveal that the 3rd order Volterra series best recapitulates the actual ventilator data and thus provides the most accurate flow measurements. The improved accuracy justifies the addition of extra parameters in the model. Furthermore, the application of cross-validation also yielded higher $\bar{r}^2$ values for the Volterra series demonstrating that the added accuracy is attributed to the enhanced description of system dynamics.

The nonparametric fitting with memory is a significantly more complicated procedure; however once implemented, it can improve the quality of the measurements through two mechanisms. We can use the kernels to try and improve the fit by using longer memory for the same order or using a higher order of the same memory. These decisions can be based on the kernel values. For instance, $h_2(5,5)$ is equal to -11.95 but it drops

down an order of magnitude to -1.88 at $h_2(6,6)$ which represents the highest 2nd order lag. On the other hand, the value of $h_3(4,4,6)$ is two orders of magnitude higher than that of $h_3(6,6,6)$. This suggests that increasing memory may not increase in accuracy significantly. Alternatively, the relatively large absolute 3rd order kernel values at low lags suggest that increasing the order has a larger effect than memory. Another advantage of the nonparametric fitting is that it requires no assumption for an a priori system structure. The kernels can account for many factors without having to consider the many possible model parameter structures. In short, for nonphysiological system identification, there is no need to interpret the parameters and/or assume any structure and thus nonparametric identification is a feasible option to obtain a more accurate system characterization than using parametric fitting.

Concerning the flow sensor's calibration and since the volume delivered is load dependent, our data suggest that the volume delivered to the flow sensor is not the same as the prescribed one. This, however, should not affect the calibration of the flow sensor since it was done in an open system and any load dependence mostly influenced by the compliant loads rather than resistive ones. More importantly though, the actual fitting used the calculated volume rather than the theoretical one and thus load dependence of the ventilator should be accounted for.

The general trend regarding the delivered V_T is in agreement with Thammanomai et al. [81] who showed that the ventilator's delivered volume is less than the prescribed one due to load dependence. This indicates that the actual delivered V_T depends on the animal's response to a given treatment based on a change in its mechanical impedance.

However, there was only a slight drop following lavage, the largest being -4.43% in mouse 4. To unravel this discrepancy, assessing respiratory mechanics using the novel strategy detailed in the next chapter, we calculated the respiratory resistance (R_{RS}) and elastance (E_{RS}) values from which we obtained the magnitude of the complex respiratory system impedance ($|Z_{RS}|$) at the breathing frequency (~4Hz). Before lavage, the mean and standard deviation were R_{RS}: 2.31±0.36 $cmH_2O.s.ml^{-1}$, E_{RS}: 38±3.1 cmH_2O/mL, and $|Z_{RS}|$: 2.74±0.84 $cmH_2O.s.ml^{-1}$. Following lavage, these values were R_{RS}: 2.23±0.18 $cmH_2O.s.ml^{-1}$, E_{RS}: 49±1.9 cmH_2O/mL, and $|Z_{RS}|$: 2.89±0.35 $cmH_2O.s.ml^{-1}$. Thus, even though E_{RS} increased by 29% due to lavage, $|Z_{RS}|$ increased by only 5.5% since it is more dependent on the changes in R_{RS} (-3.5%) at around 4Hz. Furthermore, to briefly reiterate the findings by Thammanomai et al. [81], we applied the same composite signal perturbation used to calculate *CMRR* with different loads (no load, 9, 18, and 27 ml syringe). With increasing load, there was an evident dependence of reduced volume delivery. (Figure A-1, Appendix A)

CMRR arises from asymmetries in the flow sensor and/or the differential pressure transducer, amplifier, and the magnitude of flow sensor resistance [92,93]. *CMRR* is highest when the resistance of the flow sensor is comparable to or higher than the impedance of the subject and when asymmetry is most pronounced. In our application, due to 1) the low resolution of 3-D printing (0.1 mm) compared to the tubing dimensions connecting the sensor outlets with the transducer ports, 2) the comparable values between the flow sensor and mouse resistance, and 3) the large pressure range of the pressure transducer (requiring an amplifier and making the system more susceptible to noise), the

CMRR is likely more dependent on the transducer (asymmetrical structure and range), tubing and the amplifier characteristics. Thus, in general, any improvements to *CMRR* would require selecting an amplifier-transducer system with proper range and high *CMRR* and minimizing the length and asymmetry of the flow sensor outlets and the associated tubing.

The current *CMRR* of our sensor is within acceptable limits. Peslin et al. [93] addressed the issue of minimizing human impedance measurement errors obtained by the FOT [29] waveform with a maximum frequency range of 30 Hz. For impedance measurements, the best available transducer had a *CMRR* of 70 dB at a frequency of 30 Hz, and they recommended a minimum *CMRR* of 40 dB at 30 Hz or the highest frequency of interest [93]. The calculated *CMRR* values from our setup were less by around 10 dB than the minimum threshold. However, the flexiVent system is generally used to probe impedance only up to 20 Hz at which our *CMRR* is 35 dB and for the purposes of tracking flow during ventilation at the ventilation frequencies between 1 and 5 Hz [91], the *CMRR* is above 40 dB (Figure 3-4). If further accuracy is required particularly for impedance measurements, Farré et al. [92] proposed a general technique to correct for transducer asymmetry for linearly behaving transducers which resulted in a maximum error in measured respiratory mechanics (resistance, inertance, and compliance) of 4%. Even without the correction, for a *CMRR* of 40 dB and a respiratory to pneumotachograph ratio of 5 (close to our design), the percent error in measured impedance is less than 5% [92]. However, more interestingly, it is actually possible to use the Volterra series to account for the transducer's asymmetry and thus correct for flow regardless of the *CMRR*. This

technique is also independent of any linearity assumption. To exemplify, we corrected the transducer's measured pressure by fitting/matching it to *P* through using Volterra series. Then the corrected pressure was used to measure a corrected flow. With a Volterra series of order 1 and memory 6, the corrected flow has an $\bar{r}^2$ of 0.9335 in comparison to the unadjusted flow ($\bar{r}^2$=0.685). (Figure A-2, Appendix A). Thus, the Volterra series can account for all system nonlinearities regardless of transducer characteristics. However, this calibration should be carried out every time the setup is changed (i.e., transducer, sensor, or tubing).

One limitation of the current sensor design which affects its practicality is the resolution of the 3-D printer. Since in our case the resolution was 0.1 mm and the inner core diameter was 0.5 mm, it was necessary to calibrate every sensor individually. The best currently available 3-D printers have resolutions as low as 0.02 mm which would give a 15% error in the theoretical value of the sensor's resistance.

Another limitation of the flow sensor is related to its effect on the natural mouse breathing physiology. Since a ventilator was used in the experiments, any effect of the sensor on the mouse's breathing pattern was overridden. Thus, the physiological effects of the flow sensor on breathing need to be examined without using the ventilator. As a preliminary test, expired CO_2 levels were recorded for around a minute in a mouse following tracheostomy and cannulation. A T-tube was secured to the cannula with the side port attached to a capnometer (MicroCapStar, CWE Inc, Pennsylvania) and measurements of CO_2 was carried out with and without the flow sensor connected to the other end the T-tube. In the absence of the flow meter, $\%CO_2$ varied between 3.1 and 3.8% whereas in the

presence of the flow meter, $\%CO_2$ was between 2.7 and 3.3% (Figure A-3, Appendix A). These values are somewhat under the normal range of 4.0-5.5% [94] possibly due to the anesthesia and/or the resistance of the endotracheal tube, which we estimated to be 0.4 $cmH_2O.s.ml^{-1}$, a value surprisingly close to R_S. Thus, while our $\%CO_2$ values can be considered acceptable, further tests may be warranted if the flow sensor is to be used without ventilator support.

3.4.2 Mouse experiments

The flow sensor was used to properly predict flows continuously, whether for VV or spontaneous breathing in the mouse experiments, for the total experimental time, and across the range of collected physiological mouse flow values. However, more importantly, this ability to monitor continuously, revealed a considerable discrepancy between V_P and $\overline{V}_T$ which has important implications for ventilation studies. It reveals that in general experimental settings, $\overline{V}_T$ could be significantly different than V_P and the control and treatment groups may in fact receive different V_T's. The former could be expected since ventilator never delivers the prescribed volume exactly due to gas compression in the cylinder. Corrections for gas compression can be made, in principle, but the flow sensor is able to measure the delivered volume directly, which has the advantage of avoiding errors and nonlinearities in the ventilator's calibration. This is further justified since most ventilators assume linear behavior when they calibrate for system properties (gas compliance, resistance and inertance); however, these could have some degree of nonlinearity especially when the flow sensor itself and the cannula are nonlinear.

More problematic though is the difference in $\overline{V}_T$ between groups. This can

adversely alter the experimental outcome either by reaching a wrong conclusion or missing a treatment's beneficiary effect. For example, unnoticed reduction in V_T due to the load dependence of the ventilator was shown to severely compromise lung function leading poor survival of mice with acute lung injury [81]. Our flow sensor can provide assistance to avoid such pitfalls by reducing both inter- and intra-group variabilities. First, it can be used post experimentally to verify that groups received the same or the desired V_T further strengthening any observation. Second, it can help researchers characterize a flow-load characteristic curve for their ventilators (along with any external connections) to correct for ventilator-load dependence. Third, it can also be a helpful tool when used as an online feedback mechanism to adjust the ventilator settings such that the delivered and prescribed settings match as the experiment is being conducted.

An additional benefit is the ability to monitor expiratory flow rates and determine if the subject is fully exhaling. If that is not the case, auto positive end-expiratory pressure (PEEP) might buildup altering the delivered flow and final outcome. This is critical in ventilator-induced lung injury models where unknowingly adding PEEP misleads to interpretations of the injury mechanism.

3.5 Conclusion

We have shown that nonparametric nonlinear system identification with memory (Volterra series) can be effectively utilized in a rapidly fabricated 3-D printed pneumotachograph-type flow sensor that provides accurate measurements of air flow in small experimental animals allowing researchers to monitor flow continuously, correct for any nonlinear system dynamics, and provide better experimental control. The current

device is designed specifically for and well tolerated by ventilated mice, but the design can be readily adjusted to accommodate other rodents.

3.6 Acknowledgements

This study was funded by the National Institutes of Health (NIH) grants HL 124052 and HL 126040. Capnometer measurements were possible thanks to Sefik Evren Erdener and Kivilcim Kilic (Neurophotonics Center, Boston University).

Chapter 4: ZVV

4.1 Introduction

The ability to measure continuously pressure (P) and flow ($\dot{V}$) recordings during variable ventilation (VV) allows us to utilize VV's inherent potential to measure respiratory system impedance (Z_{RS}). The essence of VV is that physiological values of tidal volume (V_T) and respiratory frequency (F_R) vary on a breath-by-breath basis. Since each breath has a distinct amplitude/V_T and frequency/F_R, over a long enough time period, VV actually probes the lung at multiple frequencies and amplitudes. We hypothesized that the variations in V_T and F_R present in VV can be utilized to assess the low-frequency features of Z_{RS}. To test this hypothesis, we first, analyzed VV data collected previously in human patients with mild ARDS. Second, to verify the accuracy of the approach under precisely controlled conditions, we applied ZVV to ventilated healthy mice followed by lavage as a model of ARDS. Finally, to assess whether Z_{RS} from ZVV is prone to transient effects due to the breath-to-breath variations present in VV, we simulated lung mechanics during VV and compared the ZVV-based estimates of Z_{RS} from non-steady-state recordings to theoretical steady-state values.

4.2 Methods

4.2.1 Measurement of Z_{RS} during VV: the ZVV technique

The steps involved in the ZVV approach are as follows:

- The subject is ventilated using VV.
- Breath-by-breath $\dot{V}$ and P recordings are stored for processing.

- The beginning and end of every breath are determined and each breath is analyzed separately.
- V_T and F_R of each breath delivered by the ventilator are calculated.
- Z_{RS} is calculated for each breath by dividing the discrete Fourier transform of ΔP, the pressure difference between absolute airway pressure and the positive end-expiratory pressure (PEEP), with that of $\dot{V}$.
- Values of respiratory resistance (R_{RS}) and elastance (E_{RS}), or volumetric stiffness, are evaluated as the real part of Z_{RS} and the imaginary part of Z_{RS} multiplied with $-2\pi F_R$, respectively, at F_R.
- The data are filtered by setting a minimum and maximum for F_R, R_{RS}, and E_{RS} and excluding values outside the range due to systematic and random errors corresponding to faulty breath detection, nonphysiological values, or patient respiratory effort.
- R_{RS} and E_{RS} are binned according to F_R. For each bin, R_{RS} and E_{RS} values that are 2 standard deviations away from the mean are removed. The means and deviations of R_{RS} and E_{RS} are then recomputed.
- The binned R_{RS} and E_{RS} spectra represent the low-frequency mechanical properties of the respiratory system for the time interval during which the subject is ventilated with VV.
- In a similar fashion, R_{RS} and E_{RS} are binned as a function of V_T.
- Changes in mechanical function with respect to different time periods (T) can be obtained by segmenting the total VV data into different time segments (T1, T2…).

- In order to capture the V_T, F_R, and T dependence of the mechanical properties, R_{RS} and E_{RS} are plotted against various combinations of the bins within each time segment.

4.2.2 Human clinical trial

Previously collected patient data was analyzed using ZVV (see biographic data of all patients in Appendix B.1, Table B-1). The protocol to ventilate patients with VV was approved by the FDA and the IRB of Boston University School of Medicine. Five male patients with mild ARDS were mechanically ventilated using a modified ventilator capable of delivering VV (Puritan Bennett 840 Ventilator, Covidien. Ireland, Dublin). The system consisted of a laptop to control the desired settings through a custom-designed computer program (LabVIEW, National Instruments, Austin, TX), the breath delivery unit of the ventilator, and a graphical user interface to monitor the outputs. The ventilation was divided into two sections, one with CV and the other with VV delivered in random order with a 1 h washout period between them using CV. However, with regard to the objectives of the current study, only the VV time domain data are relevant and reported here. At the beginning of the VV session, the respiratory therapist set up the baseline ventilation parameters including the baseline tidal volume ($V_{T,B}$) and baseline respiratory frequency (F_B) based on biometric data and patient condition. The objective was to deliver a range of tidal volumes such that the peak inspiratory pressure (PIP) was uniformly distributed within a range of ±30% around the mean PIP corresponding to $V_{T,B}$ [46]. This was achieved by first delivering 3 cycles with a V_T=1.4$V_{T,B}$ and recording airway opening pressure and flow in order to obtain a partial pressure-volume (P-V) curve. For each VV cycle during

the protocol, a PIP was randomly chosen from this distribution and the P-V curve was then used to compute the corresponding V_T to be delivered by the ventilator. To maintain constant minute ventilation (MTV= $F_R V_T$) on a cycle-by-cycle basis, F_R was computed for each cycle as $F_R = F_B V_{T,B}/V_T$. Finally, for patient comfort, the inspiratory time was allowed to vary only by 10% in each cycle.

During VV, pressure and flow data were recorded (50 Hz) by the ventilator and saved for off-line processing. Following the experiments, the flow tracing was used to determine the beginning and end of every breath from which V_T and F_R were computed. The pressure-flow recordings were then split into two equal time periods (T1 and T2), and the ZVV analysis described above was separately carried out on the 1st period (T1) as well as the 2nd period (T2). The R_{RS} and E_{RS} values in each section were grouped according to 5 frequency bins allowed by the cycle-by-cycle fluctuations in F_R. The R_{RS} and E_{RS} data were then plotted for every patient as a function of F_R. The full set of data was also binned into a low V_T ($V_{T,1}$) and high V_T ($V_{T,2}$) where the maximum V_T ($V_{T,max}$) and minimum V_T ($V_{T,min}$) were used to claculate the threshold $\left(\frac{V_{T,max}+V_{T,min}}{2}\right)$. Since the recorded time periods in some patients were shorter, the criteria set for breath inclusion and the length of ventilation used varied among patients: per period, the time interval ranged from 23 minutes to 64 min of ventilation with the number of breaths between 200 and 900.

4.2.3 Mouse experiments

The data collected in the 5 mechanically ventilated mice, described in the methods section of chapter 3 (3.2.5), were analyzed via ZVV. As in the human data, the same

analysis was carried out both before and after lavage, which reproduces the physiology of ARDS in the mouse. The periods T1 and T2 included the first and last 5 minutes of VV, respectively. In addition, using all the VV time data before and after lavage separately (pooling T1 and T2), the mean values of R_{RS}, E_{RS}, and F_R were calculated. The evaluated mean of F_R was used to calculate the equivalent R_{RS} and E_{RS} from the OVW data (Appendix B.2). Then the values obtained from the 4 OVW recordings were averaged and compared to the ZVV-derived ones (e.g., ZVV vs OVW).

4.2.4 Computational study

The calculation of Z_{RS} with Fourier analysis requires that the measured system is in a steady state. However, since both F_R and V_T vary from cycle to cycle during VV, the mechanical state of the respiratory system is also affected by transients. To test how such transients influence the estimated values of R_{RS} and E_{RS} using the ZVV approach, a linear viscoelastic Kelvin body was utilized to represent the lung (Appendix B.3) [95,96]. The mechanical model consisted of a dashpot (R_1) in series with a spring (E_1) and both in parallel with another spring (E_2). E_2 captures the static elastic property of the lung, while R_1 in series with E_1 accounts for the viscoelastic properties [96]. The parameter values (R_1= 60 $cmH_2O.s.L^{-1}$, E_1=20 $cmH_2O.L^{-1}$, and E_2=5 $cmH_2O.L^{-1}$) were selected so as to replicate the magnitudes of R_{RS} and E_{RS} observed in the human data. The ZVV procedure described above was carried out to reconstruct the Kelvin body's frequency dependent Z_{RS} from the simulated VV data. To observe the effects of the transients and breath-to-breath variations in F_R/V_T, a secondary binning was carried on both R_{RS} and E_{RS}. Specifically, after binning the data across F_R, the R_{RS} and E_{RS} spectra were further binned based on the time difference

in periods between consecutive breaths (ΔT_b). Based on preliminary results, we introduced a correction method to estimate a steady-state pressure difference (ΔP_s) between absolute airway pressure and the PEEP in order to minimize the effects of transients (Appendix B.3). This simple method matched the end-to-end pressure of every breath by removing a linear trend. To test the robustness of this correction (Eqs. B.8 and B.9), starting from a baseline simulation (sampling frequency = 50 Hz, number of breath = 500 breaths, $10 \leq F_R \leq 20$ breath/min, MTV=7.5 L/min), an additional 14 sets of simulations were carried out in which only one parameter was changed at a time. For each simulation, the mean values of R_{RS} and E_{RS} using both ΔP_s and ΔP were computed and grouped into 8 frequency bins and the errors with respect to the Kelvin body (Eqs. B.4 and B.5) were calculated.

4.2.5 Statistical analysis

All data analyses and statistical tests were performed using MATLAB R2018b (MathWorks, CA). The statistical tests used were MATLAB's built-in functions. For the human clinical trial, to account for the effects of F_R, T, and any interaction between these factors, a 2-way Anova was applied to the whole data set. For the Anova, the F_R bins were categorized from 1 to 5 representing the lowest and largest frequency bin center respectively, while T was categorized to 1 and 2 to represent T1 and T2, respectively. For the mice, a 3-way Anova was used with the additional effect of lavage. Following the 3-way Anova, a multiple comparison test (Tukey's honestly significant difference) was used to separate the effects of lavage within T. Paired t-tests were used to compare the values of R_{RS} and E_{RS} from VV and FOT. Finally, ranksum tests were used to compare V_T dependence. Statistical significance was accepted at $p<0.05$.

4.3 Results

4.3.1 Human clinical trial

The ZVV approach is exemplified in Figure 4-1. Recordings of flow (Figure 4-1A) and pressure (Figure 4-1B) tracings of two consecutive cycles from patient 1 were analyzed. The recordings were separated into individual breaths and for each breath, the respiratory resistance (R_{RS}) and elastance (E_{RS}) were estimated using ZVV as well as via 2 time domain approaches (Appendix B.4, Figure B-1) that provided similar results to those of ZVV.

The corresponding discrete Fourier transforms are shown in the insets. Using the transforms, R_{RS} and E_{RS} can be computed from the complex ratio of pressure and flow, Z_{RS}, as the real part and $-2\pi F_R$ times the imaginary part, respectively. Both the full cycle and the inspiratory phase only time domain data are also fitted using a 2 element R_{RS}-E_{RS} model (Appendix B.4). The corresponding fits are relatively close to each other and so are their R_{RS} and E_{RS} parameters displayed in the top right box.

Applying ZVV to all patients reveals both general trends as well as patient specific results within the population (Figure 4-2). For instance, R_{RS} and E_{RS} decreased from the first half of the time recording (T1) to the second half (T2) in all patients while the amount of drop from T1 to T2 varied among patients. With respect to F_R, R_{RS} decreased in all patients and E_{RS} was nearly constant in most patients. Also, R_{RS} increased with V_T in all patients in both T1 and T2, but changes in E_{RS} were patient specific with patients 3-5 displaying an increase during both T1 and T2.

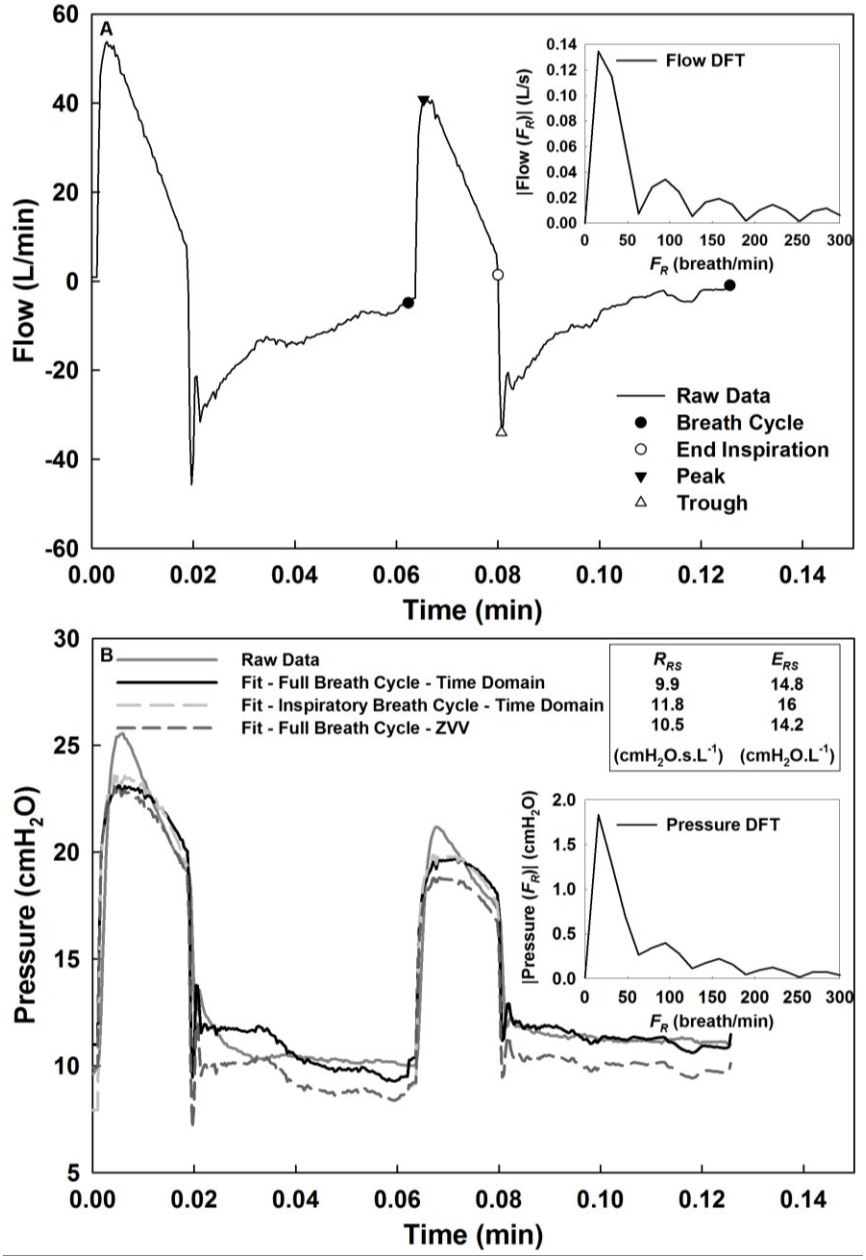

Figure 4-1: Breath detection and ZVV application. A) Flow and B) pressure time series of two consecutive cycles with different V_T's from patient 1. Notice that the two breaths are different due to VV. The flow is used to detect breath cycles as well as flow peaks, troughs, and end of inspiration as shown in the 2nd cycle flow data. The corresponding discrete Fourier transforms are shown in the insets. Using the transforms, R_{RS} and E_{RS} can be computed from the complex ratio of pressure and flow, Z_{RS}, as the real part and $-2\pi F_R$ times the imaginary part, respectively. Both the full cycle and the inspiratory phase only time domain data are also fitted using a 2 element R_{RS}-E_{RS} model (Appendix B.4, Figure B-1). The corresponding fits are relatively close to each other and so are their R_{RS} and E_{RS} parameters displayed in the top right box.

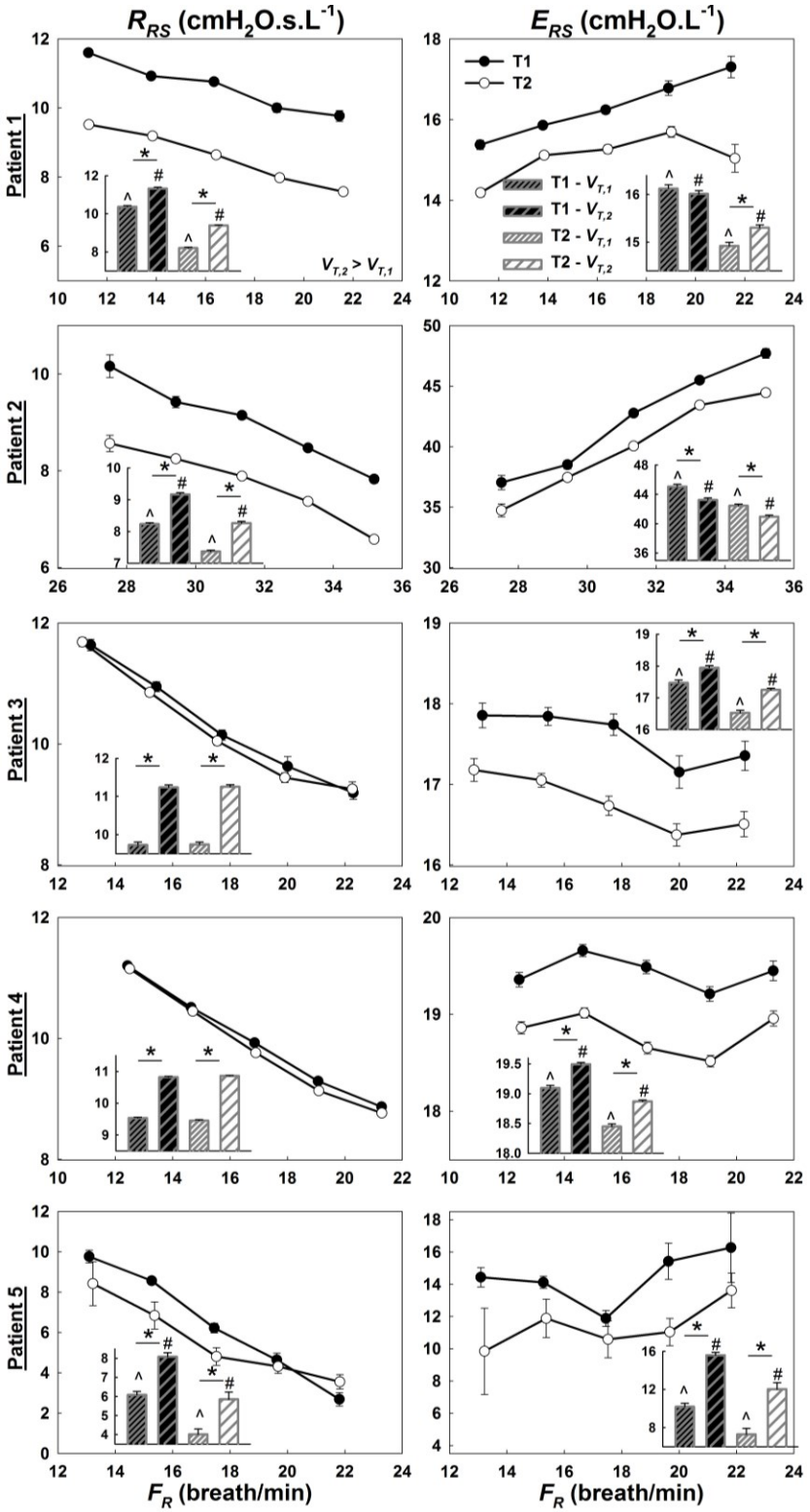

Figure 4-2: Human ZVV results (see next page for complete caption).

Figure 4-2: Human ZVV results (see previous page for Figure). Analysis results showing the binned means and standard errors of R_{RS} and E_{RS} as a function of F_R and V_T (bar charts insets) for both the first and second halves of the time recording T1 and T2. Notice that the lowest F_R in patient 2 was greater than the highest F_R in all other patients. Note also that the error bars are often smaller than the symbols. (*): significance between V_T within same T. (^) and (#): significance from T1 to T2 for $V_{T,1}$ and $V_{T,2}$ ($V_{T,2} > V_{T,1}$).

The full statistics, summarized in Table 4-1, show that in all 5 patients, E_{RS} decreased significantly with from T1 to T2 ($p<10^{-5}$). In 4 patients, R_{RS} decreased significantly ($p<0.005$) as a function of T. In all 5 patients, R_{RS} and E_{RS} also exhibited a statistically significant frequency dependence. In most patients, R_{RS} and E_{RS} were independent of the interaction between F_R and T (F_R*T).

Table 4-1: Summary of human acute lung injury results.

Respiratory Resistance ($cmH_2O.s.L^{-1}$)											
		T1			**T2**			**T1 Vs. T2**	**p-values**		
n	**t**	**nb**	**μ**	**SE**	**nb**	**μ**	**SE**	Δ	F_R	**T**	F_R***T**
1	107	677	10.8	0.05	688	8.9	0.03	-18.2%	**$<10^{-80}$**	**$<10^{-100}$**	**0.022**
2	47	639	8.8	0.05	608	7.6	0.04	-13.2%	**$<10^{-100}$**	**$<10^{-50}$**	0.26
3	60	327	10.58	0.063	419	10.56	0.054	-0.2%	**$<10^{-100}$**	0.4	0.71
4	120	895	10.13	0.028	888	10.07	0.028	-0.5%	**$<10^{-100}$**	**$<10^{-5}$**	0.060
5	129	482	7.2	0.15	203	4.9	0.23	-31.8%	**$<10^{-50}$**	**0.0049**	**0.019**
Respiratory Elastance ($cmH_2O.L^{-1}$)											
		T1			**T2**			**T1 Vs. T2**	**p-values**		
n	**t**	**nb**	**μ**	**SE**	**nb**	**μ**	**SE**	Δ	F_R	**T**	F_R***T**
1	107	681	16.1	0.06	683	15.0	0.05	-6.4%	**$<10^{-10}$**	**$<10^{-30}$**	**0.0005**
2	47	637	43.6	0.20	603	41.0	0.17	-6.0%	**$<10^{-150}$**	**$<10^{-30}$**	**0.020**
3	60	326	17.7	0.07	423	16.9	0.06	-4.6%	**$<10^{-5}$**	**$<10^{-10}$**	0.80
4	120	900	19.5	0.03	898	18.8	0.03	-3.3%	**$<10^{-10}$**	**$<10^{-30}$**	0.080
5	129	487	13.8	0.30	199	11.6	0.52	-15.8%	**0.0043**	**$<10^{-5}$**	0.34

n: patient number, t: time studied (min), nb: number of breath, μ: mean, SE: standard error, Δ=(T2-T1)/T1.

4.3.2 Mouse experiments

Testing the ZVV approach under controlled conditions revealed qualitatively similar as well as mouse specific results when compared to the human data (Appendix B.1, Table B-2). Indeed, with increasing F_R, R_{RS} decreased slightly, but E_{RS} generally increased both before and after lavage (Figure 4-3). With respect to V_T, R_{RS} increased while E_{RS} decreased both in T1 and T2 before lavage. Following lavage, E_{RS} increased while R_{RS} remained subject specific either decreasing or increasing. Interestingly, lavage reversed the effect of T: before lavage, E_{RS} increased from T1 to T2, while following lavage, it decreased from T1 to T2 (Appendix B.1, Table B-3).

Next, we compared R_{RS} and E_{RS} from ZVV with those obtained independently using the optimal ventilator waveform (OVW, Appendix B.2) forced oscillation technique [97]. The means and standard errors of R_{RS} and E_{RS}, in units of $cmH_2O.s.ml^{-1}$ and $cmH_2O.ml^{-1}$, respectively, calculated using ZVV were 2.31±0.36 and 38±3.1 before lavage and 2.23±0.18 and 49±1.9 after lavage. The corresponding values obtained from OVW at the mean F_R were 0.93±0.33 and 35±0.8 before lavage and 0.96±0.17 and 48±0.7 after lavage, respectively. While E_{RS} from ZVV and OVW did not differ, the difference in R_{RS} was significant ($p=0.036$ and $p=0.002$ before and after lavage, respectively).

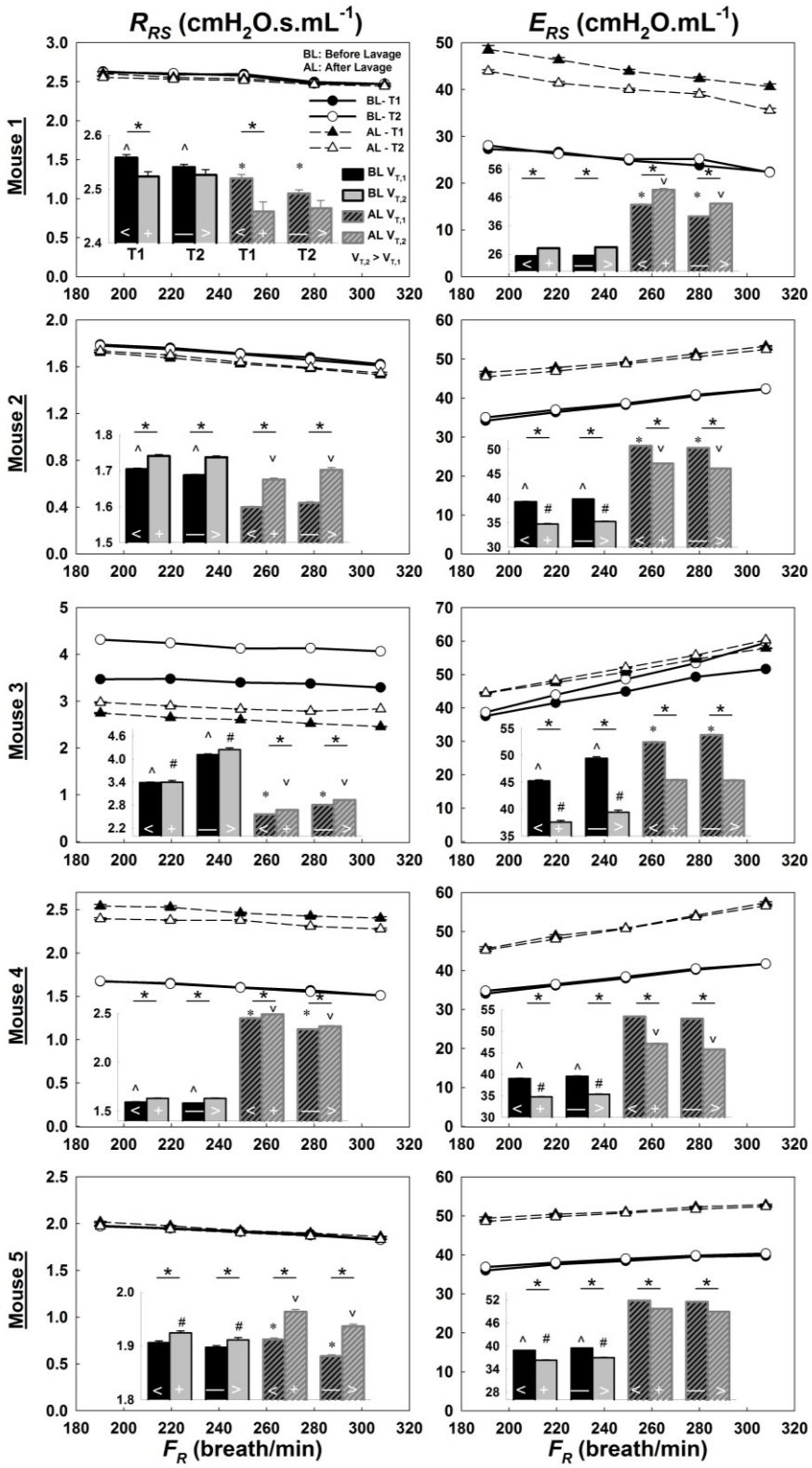

Figure 4-3: Mouse ZVV results (see next page for complete caption).

Figure 4-3: Mouse ZVV results (see previous page for Figure). Analysis results showing the means and standard errors of R_{RS} and E_{RS} as a function of F_R and V_T (bar charts insets) for T1 and T2 before and after lavage. With respect to F_R, R_{RS} showed a decrease in all mice, while E_{RS} increased in 4 out of 5 mice before and after lavage. With respect to V_T, expect for mouse 1, R_{RS} increased while E_{RS} decreased significantly with increasing V_T both in T1 and T2 before and after lavage. Following lavage, E_{RS} increased in all mice while R_{RS} was subject specific either decreasing or increasing. However, the effect of T on E_{RS} before and after lavage was different (Table B-3). Although the percent changes were small (<10%), they were statistically significant in 4 out of 5 mice. (*): Significance between V_T within same T. (^) and (#): significance between T1 and T2 for $V_{T,1}$ and $V_{T,2}$ before lavage. (*) and (∨): significance between T1 and T2 for $V_{T,1}$ and $V_{T,2}$ after lavage. (<) and (+): significance before and after lavage during T1 for $V_{T,1}$ and $V_{T,2}$. (—) and (>): significance before and after lavage during T2 for $V_{T,1}$ and $V_{T,2}$.

4.3.3 Computational study

To quantify the extent to which the transients affected ZVV, we used computational modeling summarized in Figure 4-4. There was a systematic error in R_{RS} that increased with ΔT_b, the difference in time periods in consecutive breaths, resulting in an overestimation at low F_R but an underestimation at high F_R (Figure 4-4A). The error in E_{RS} was much smaller (Figure 4-4B). However, applying our correction for transient pressures (ΔP_s) drastically reduced the error in R_{RS} (Figure 4-4C) from 19% to -1.9% for an F_R close to 10 breath/min and from -42% to +1.6% for an F_R close to 20 breath/min. Nevertheless, E_{RS} was properly estimated using both techniques with an error less than 2% (Figure 4-4D). The proposed correction similarly reduced the errors when the parameters of the model were varied (Appendix B.3, Table B-4).

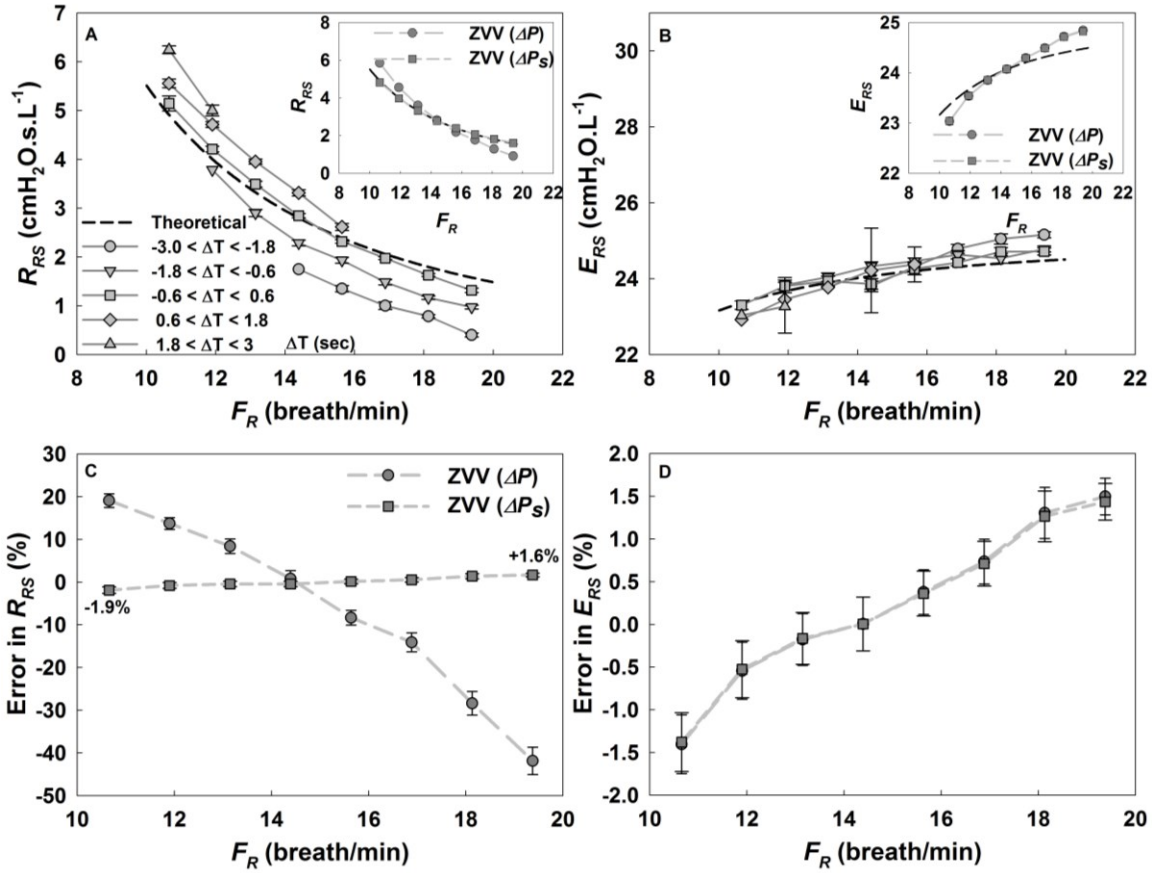

Figure 4-4: Kelvin body simulations. R_{RS} (A) and E_{RS} (B) as a function of F_R and ΔT_b, the difference in the periods between consecutive breaths (different gray-colored curves). The solid dashed line is the theoretical impedance and the solid gray lines are obtained from the breath-by-breath ZVV analysis. Curves with different symbols represent cycles corresponding to different ΔT_b. The R_{RS} and E_{RS} irrespective of ΔT_b are plotted in the insets with and without pressure correction (ΔP and ΔP_s, respectively). Percent error are shown with respect to theoretical steady-state values for R_{RS} (C) and E_{RS} (D) as a function of F_R with (ΔP_s) and without (ΔP) transient pressure adjustment.

4.4 Discussion

In this study we introduced a novel clinical approach, ZVV, for continuously estimating a subject's respiratory resistance (R_{RS}) and elastance (E_{RS}) at physiological breathing rates during variable ventilation (VV). ZVV obviates the need for specialized FOT equipment or ventilation methods that were developed in the past [3,30,37,90,98] but remain impractical and limited during mechanical ventilation of patients. The clinical potential of ZVV was demonstrated in human patients with mild ARDS and further validated in a mouse model of ARDS, in which ZVV provided a smooth frequency response. The R_{RS} and E_{RS} spectra from ZVV were also compared with direct FOT and computational modeling verified that a simple pressure correction can avoid errors due to transients inherent in VV. Our analysis thus demonstrated that ZVV can accurately detect changes in functional lung mechanics even when they are minor. The application of ZVV in human ARDS patients provided strong evidence that VV has positive impact on lung function in human patients with ARDS. To our knowledge, this is the first report to demonstrate VV's therapeutic potential in human patients.

Traditional FOT measurements include several breathing cycles and are applied only periodically [3,99]. Moreover, in conscious patients, the FOT also requires the patient to be cooperative throughout the measurement. Since ZVV is measured utilizing the breathing waveform of the ventilator, it estimates the respiratory system impedance under more physiological conditions than the small-amplitude FOT. Furthermore, in contrast to the FOT and the OVW approaches, ZVV derives the frequency dependence of R_{RS} and E_{RS} from hundreds or thousands of breaths with varying F_R. Additionally, since ZVV evaluates

Z_{RS} only at the fundamental frequency of the ventilator waveform, R_{RS} and E_{RS} are minimally affected by nonlinearities that often hinder the FOT to produce smooth impedance spectra superimposed on breathing. Finally, binning R_{RS} and E_{RS} according to V_T also allows studying the effects of system nonlinearities at the physiological breathing rates.

The primary limitation of the ZVV technique is that it requires the subject to be mechanically ventilated using VV, and is therefore limited to such patient population. On the other hand, a continuous recording of the mechanical impedance can be useful for tracking any changes in lung function during any intervention or drug testing. Another disadvantage is that each value of R_{RS} and E_{RS} is derived from a single cycle which means that in contrast to the FOT, frequency dependence of R_{RS} and E_{RS} cannot be obtained quickly.

During MV the inspiratory cycle is driven by the ventilator, while the expiration is a passive process. The ZVV approach, however, analyzes the full breath unlike the FOT in which the respiratory system is actively driven throughout the full cycle. In order to investigate the extent to which the R_{RS} and E_{RS} values are influenced by passive expiration in ZVV, we also determined R_{RS} and E_{RS} in the time domain both from inspiration only and the full cycle by fitting the pressure-flow data using a 2-element R_{RS}-E_{RS} in-series model (Appendix B.4). This approach resulted in similar values obtained from ZVV and showed similar trends across time (Appendix B.4).

4.4.1 Human clinical trial

From Figure 4-2 as well as Table 4-1, it is observed that the data are smooth with small error bars and their quality is sufficient to allow the fitting of parametric models. This is because the binning process and the breath selection criteria partition and average the data over a relatively long period of time. Thus, abnormal breaths which might have been missed by the algorithm or due to the patient's own attempts to breathe have little effect on the final R_{RS} and E_{RS} spectra. As an example, it is worth noting that patient 5's E_{RS} spectrum is least smooth and this may be attributed to the patient-ventilator asynchrony. Evidently, for the method to work best, it is important that the patient show minimal spontaneous breathing efforts.

The decrease in R_{RS} and E_{RS} from T1 to T2 in the human data signifies that VV induced an improvement in lung mechanics. Nevertheless, some patients showed minimal yet statistically significant improvements. Surprisingly, however, R_{RS} in all patients and E_{RS} in most patients increased with V_T for both T1 and T2. While the increase in R_{RS} can be attributed to nonlinear flow dynamics in the airways, the increase of E_{RS} is less expected, yet it has been reported previously in human patients [100]. This suggests that some recruited regions may have been over ventilated as the higher tidal volumes could reach the upper more nonlinear portion of the acinar pressure-volume curve. Regardless of the extent of the improvement, the ability to monitor the level of response to treatment or changes in ventilation settings provides a quantitative personalized approach to clinical ventilation. As Table 4-2 demonstrates, even a small improvement (or deterioration) in respiratory mechanics can be detected by ZVV. This can have important implications for

the treatment of ARDS patients in clinical settings. Future studies could benefit from this technique by tracking the responses to clinical maneuvers in ARDS such as surfactant therapy, optimization of PEEP, or altered body position.

The cause of decreasing R_{RS} and E_{RS} with time signifies the improving condition of the patients. We argue that VV itself induced this improvement for the following reasons. First, we note that the study was administered when the patients were in a stable condition and VV was always preceded by CV. Therefore, while statistically speaking improvement and deterioration would be equally likely, all 5 patients showed a decrease in both R_{RS} and E_{RS}. Second, VV has shown several benefits experimentally in both healthy and diseased animal models [47–60] and clinically in humans [61–63], not including though ARDS patients. The present results provide evidence that VV also improves lung physiology in human patients with mild ARDS. To our knowledge, only one study applied VV in human subjects during abdominal surgery which did not result in any physiological improvement [101]; however, the subjects had normal lungs and the results are similar to our mouse data before lavage. Another possibility is that the ventilation time and/or settings were not adequate for improvements to occur.

With the application of our technique, the utility of VV is extended from a potential ventilation strategy to treat patients to a powerful diagnostic tool as well. This is not the first study to propose VV as a diagnostic tool. Smith & Bates [64], through the use of modeling, demonstrated that the breath-to-breath variations inherent to VV are adequate for a numerical optimization algorithm that captures the dynamics of lung recruitment and derecruitment in healthy and injured mice. Their findings support the ability of VV to

identify the extent of lung injury in ARDS. The real-time coupling of such models with ZVV could provide further insight on lung mechanics as well as better optimized ventilation settings.

4.4.2 Mouse experiments

Thammanomai et al. [56] reported that E_{RS} remained fairly constant during VV while it linearly increased with time during CV in mice subjected to acute lung injury *via* HCl instillation. Our findings are in agreement with those of Thammanomai et al. [56]. In particular, they showed that E_{RS} remained fairly constant after ~15 minutes of VV. Figure B-2 (Appendix B.4) plots the ZVV time binned data before and after lavage. Furthermore, as observed in their experiments, our data show that E_{RS} reached a plateau only after lavage and specifically after about 5 minutes of ventilation in mice 1, 2 and 5. More importantly, there is a minor but statistically significant improvement from T1 to T2 after lavage (Appendix B.1, Table B-3). Unlike the human data, the therapeutic effects of VV are more apparent in mice since before lavage there was a slight increase in E_{RS} attributed to progressive derecruitment; however, following lavage, there was a decrease indicating VV-induced recruitment. Similar to the human patients, R_{RS} mainly increased with increasing V_T. However, opposite to the human data, E_{RS} decreased with increasing V_T suggesting in this case either alveolar recruitment or inverse tidal volume dependence [102,103].

We also found differences between R_{RS} and E_{RS} from ZVV and OVW; however, only the former was significant. The OVW provides an instantaneous result whereas the ZVV produces an average over many breaths. A more likely reason for the observed difference in R_{RS} is due to how nonlinearities contribute to the FOT during OVW and ZVV.

Data at higher frequencies in the OVW approach are estimated from the small-amplitude components of the OVW. In contrast, values from ZVV are obtained at much larger breathing amplitudes. This supports the idea that different techniques result in different assessments [104] and therefore ZVV might be more precise since it assesses R_{RS} and E_{RS} at normal breathing frequencies.

4.4.3 Computational study

To test the effects of transients due to the sudden change in V_T and F_R after each breath, a Kelvin body was utilized to represent the lung. The forward simulations revealed a difference between the theoretical R_{RS} and the ZVV-derived one. Without accounting for the transients, the difference in R_{RS} reached 47% which we attribute to the fact that the decay of a transient is more associated with viscous dissipation and hence R_{RS}. After accounting for the transients through a simple linear correction in pressure, the error was reduced by an order of magnitude. The correction is simple and can be carried out automatically. Furthermore, based on our modeling simulations (Figure 4-4A), it can be seen that simply discarding those breaths from the calculations that have an F_R much larger or smaller compared to the previous cycle will significantly reduce the bias due to transients. However, for E_{RS}, the difference was consistent and negligible even without correction (<2.5 %in either case). Furthermore, E_{RS} is more often used to guide mechanical ventilation since it reflects recruited lung [69,105–107]. The frequency dependence of E_{RS} in turn can reflect lung heterogeneity [108] which might also provide useful information on how to set ventilation parameters. Hence, the frequency spectrum of E_{RS} could be of significant relevance to clinicians, while the error in R_{RS} may not be of concern in clinical

applications.

4.5 Conclusion

We have introduced a novel approach, ZVV, to assess respiratory impedance around breathing frequencies in clinically-ventilated patients using variable ventilation. This novel method also provided evidence for the first time that VV can improve the lung mechanical conditions of human patients with mild ARDS. With the increasing need of noninvasive, accurate, clinically-practical, and inexpensive personalized patient monitoring, the ZVV approach offers a powerful diagnostic tool for clinicians during VV that can simultaneously be therapeutic.

4.6 Acknowledgements

This study was supported by NIH grant U01 HL-139466. We are grateful to Allan J. Walkey, Arnab Majumdar, and George T. O'Connor for the collection of the human data.

Chapter 5: Alveolar model

5.1 Introduction

The pressure-volume (P-V) curve of the lung has been one of the most studied relationships in lung physiology since the beginning of the field of respiratory mechanics [109–112]. Specific features of the P-V curve allows one to infer the possible contributions of alveolar recruitment, elastin, collagen and surface tension to lung mechanics in healthy as well as diseased lungs [113]. However, to gain specific information on the level of stresses and strains of a single fiber within an alveolar wall of one of 480 million estimated alveoli [66] undergoing large deformation across a range of pressures is not trivial. In order to link microscopic mechanics to macroscopic P-V curves, alveolar geometry, tissue constituents and their properties, and the interaction between alveolar units need to be considered. The composition of the alveolar septal wall consisting of elastin and collagen fibers embedded within a matrix as well as the changes pertaining to each element within several diseases such as fibrosis and emphysema are well documented [114–119]. It is these components that support the stresses within the alveolar septal wall [118]. In particular, alveolar recruitment and elastin engagement is mainly attributed to occur before the lower inflection point of the P-V curve. Collagen fibers which are wavy and much stiffer displaying nonlinear stress-strain behavior, are assumed to become recruited toward the upper inflection point of the P-V curve in order to insure that alveoli do not over expand which is the currently accepted view [113,118,119]. However, to our knowledge, there has not been any quantitative assessment concerning the role of collagen waviness in alveolar mechanics under physiological large deformation. Furthermore, it’s been long known that

a spherical balloon under initial tensile stress exhibits a runaway unstable P-V behavior [120,121], because as inflation proceeds the volume increases while the pressure decreases. Yet it is not understood how the amount, waviness, and stiffness of collagen stabilizes the alveoli insuring protection from over distension or alveolar inflation stability, defined in this context as the continuous increase in pressure with a plateauing in alveolar volume.

To address these issues, we developed an analytical model for the P-V curve of a spherical thick-walled alveolus with embedded wavy fibers and undergoing large deformations. To test the model, we fit a macroscopic P-V curve from the literature. Our results suggest separate roles for elastin and collagen in alveolar stresses and pressures and a key role for collagen waviness in providing inflation stability at normal lung volumes. To further investigate the model-suggested role of collagen waviness in inflation stability, waviness was measured in bovine lung tissue. Furthermore, through forward simulations, we shed light on how varying model parameters mimicking diseases affects the P-V curve with biological implications for using true stress rather than engineering stress.

5.2 Methods

5.2.1 Model description

The model considers a spherical, thick-walled alveolus (Figure 5-1A). During isotropic expansion, an arbitrary radius R ($R_i \leq R \leq R_e$) from the initial undeformed state stretches to a radius r ($r_i \leq r \leq r_e$) (Figure 5-1B). Within the alveolar wall, wavy collagen fibers and non-wavy elastin fibers are embedded within the matrix (Figure 5-1C and 5-1B).

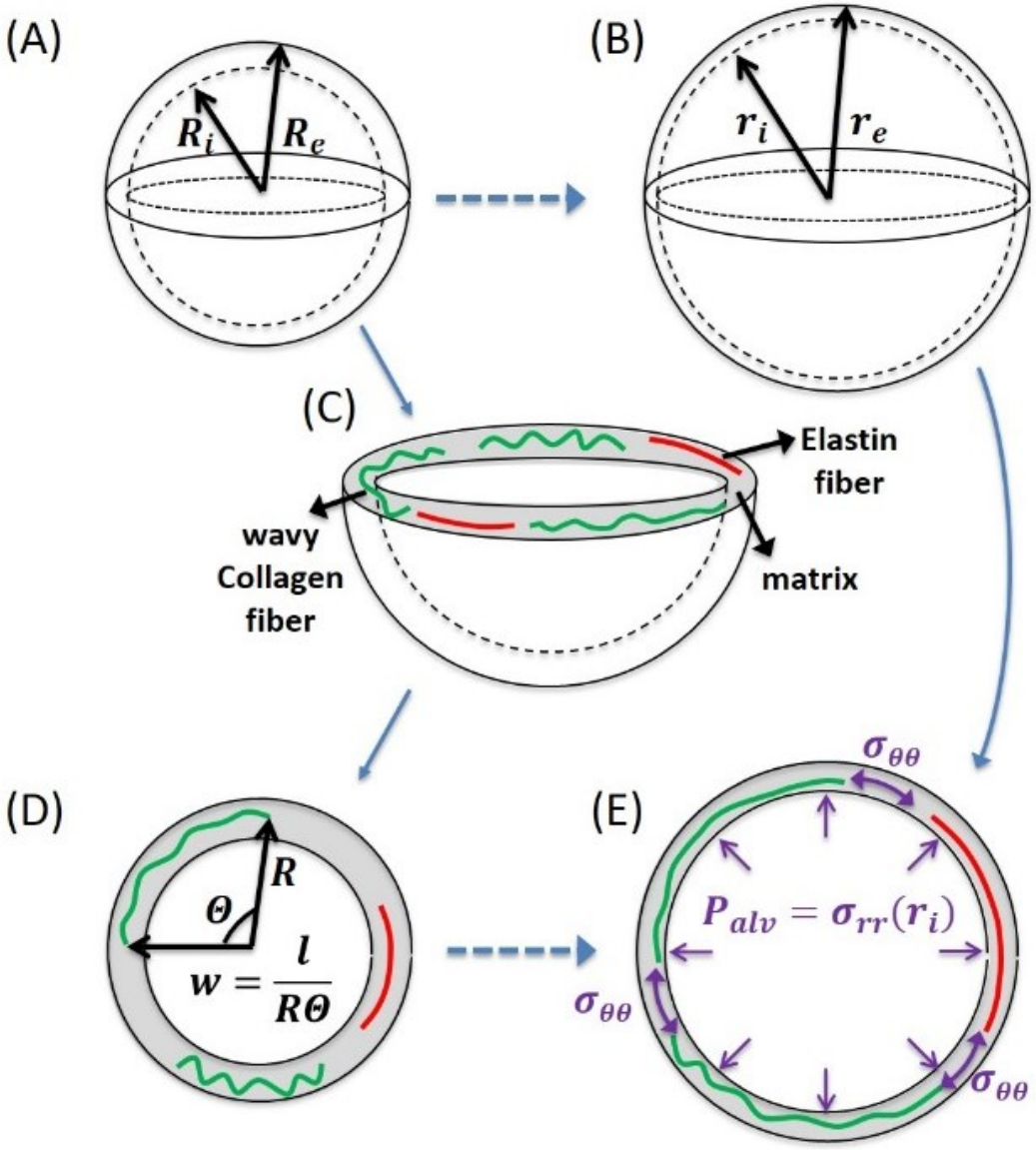

Figure 5-1: Alveolar model description. A) A thick-walled spherical alveolus of initial inner and outer radii R_i and R_e respectively. B) As the alveolus expands isotropically, its wall thickness decreases and the stretched inner and outer radii are r_i and r_e respectively. C) Within a plane slicing through the great circle of the sphere, lie the wavy collagen fibers (green) and the non-wavy elastin fibers (red) embedded in a matrix (gray). D) The waviness of a collagen fiber is defined as its contour length (l) over its end-to-end distance at rest. E) As the alveolus expands due to alveolar pressure (P_{alv}), the wavy fibers become less wavy and once fully straightened they contribute alongside the already elongated elastin fibers to the circumferential stress ($\sigma_{\theta\theta}$). Note that P_{alv} is equal to the radial pressure (σ_{rr}) at r_i.

In the undeformed state, no stress exists at the level of the fibers or alveolar wall. At the onset of expansion due to an alveolar pressure (P_{alv}) relative to the outside of the sphere, the elastin fibers instantly elongate and contribute to stress, while the collagen fibers become less wavy and only when they are fully straightened do they add to the circumferential stress $\sigma_{\theta\theta}$ (Figure 5-1E). Radial stress σ_{rr} also builds up within the wall and it equals to P_{alv} at the inner radius (r_i).

Let Y_c and Y_e represent the elastic modulus of collagen and elastin, respectively. Defining a total fiber area fraction as the product of fiber number and average fiber cross-sectional area divided by the alveolar wall cross-sectional area, $\delta_{A,c}$ and $\delta_{A,e}$ are the total area fractions for collagen and elastin, respectively. We also define the effective fiber elastic modulus as $Y_{ce} = Y_c\,\delta_{A,c}$ and $Y_{ee} = Y_e\,\delta_{A,e}$ for collagen and elastin, respectively.

Collagen fiber waviness (w) is defined as the fiber length divided by the end-to-end distance (Figure 5-1D). Collagen fiber minimum and maximum waviness are denoted by w_1 and w_2. We assume that the waviness within a population of fibers can be described by the beta probability distribution function (p) with two shape parameters α and β:

$$p(w) = \frac{(w - w_1)^{\alpha-1}(w_2 - w)^{\beta-1}}{B(\alpha,\beta)(w_2 - w_1)^{\alpha+\beta-1}} \tag{5.1}$$

where $B(\alpha,\beta)$ is the beta function of two variables (α and β).

We also introduce the stretch ratio $\lambda = \frac{r}{R}$, the inner stretch ratio $\lambda_i = \frac{r_i}{R_i}$ and a thickness mapping parameter $S = \frac{R}{R_i}$ to span across the alveolar thickness such that $1 \leq S \leq \frac{R_e}{R_i} = S_e$.

Based on this description, accounting for mass conservation, and using the deformed area in calculating stress, the true circumferential stress in the alveolar wall, at any given layer, due to elastin is:

$$\sigma_{e,\theta\theta}(\lambda, S) = Y_{ee}\frac{\lambda}{S}(\lambda - 1) \tag{5.2}$$

whereas the true circumferential stress due to the wavy collagen fibers is:

$$\sigma_{c,\theta\theta}(\lambda, S) = \frac{Y_{ce}}{B(\alpha,\beta)\alpha(\alpha+1)}\frac{\lambda}{S}\frac{\lambda - w_1}{w_1}\left(\frac{\lambda - w_1}{w_2 - w_1}\right)^{\alpha}\left((\alpha+1)A_1 - \alpha B_1\right), \quad for \quad w_1 < \lambda < w_2 \tag{5.3}$$

$$\sigma_{c,\theta\theta}(\lambda, S) = \frac{Y_{ce}}{B(\alpha,\beta)\alpha(\alpha+1)}\frac{\lambda}{S}\frac{\lambda - w_1}{w_1}\left((\alpha+1)A_2 - \alpha B_2\right), \quad for \ \lambda \geq w_2 \tag{5.4}$$

where

$$A_1 = F_1\left(\alpha; 1-\beta, 1\,; \alpha+1; \frac{\lambda - w_1}{w_2 - w_1}, -\frac{\lambda - w_1}{w_1}\right) \tag{5.5}$$

$$B_1 = F_1\left(\alpha+1; 1-\beta, 1\,; \alpha+2; \frac{\lambda - w_1}{w_2 - w_1}, -\frac{\lambda - w_1}{w_1}\right) \tag{5.6}$$

$$A_2 = F_1\left(\alpha; 1-\beta, 1\,; \alpha+1; 1, -\frac{w_2 - w_1}{w_1}\right) \tag{5.7}$$

$$B_2 = F_1\left(\alpha+1; 1-\beta, 1\,; \alpha+2; 1, -\frac{w_2 - w_1}{w_1}\right) \tag{5.8}$$

and F_1 is the Appell hypergeometric function of two variables (α and β).

The total circumferential stress ($\sigma_{\theta\theta}$) is then the summation of the two ($\sigma_{\theta\theta}(\lambda, S) = \sigma_{e,\theta\theta} + \sigma_{c,\theta\theta}$). Assuming that no shear stress exists within the alveolar wall and applying

the equations of equilibrium, P_{alv} can be computed as:

$$P_{alv} = \frac{2}{\lambda_i^2} \int_{S=1}^{S_e} \frac{S^2}{(S^3 + \lambda_i^3 - 1)^{\frac{1}{3}}} \sigma_{\theta\theta}(\lambda, S) dS \tag{5.9}$$

Finally, assuming a finite but thin alveolar wall, the stress across the wall can be assumed to be uniform and equal to the mean stress ($\bar{\sigma}_{\theta\theta}$) evaluated at the middle layer. This reduces Eq. 5.9 to the final analytical expression:

$$P_{alv}(\lambda_i) \cong \bar{\sigma}_{\theta\theta} \left[\frac{(\lambda_i^3 + S_e^3 - 1)^{2/3}}{\lambda_i^2} - 1 \right] \tag{5.10}$$

while the alveolar volume (V_{alv}) with an initial value V_o is expressed as:

$$V_{alv} = V_o \lambda_i^3 \tag{5.11}$$

Thus to construct an alveolar P-V curve, the final model includes 8 parameters, 6 parameters related to the fibers (Y_{ce}, Y_{ee}, α, β, w_1, w_2) and 2 parameters related to alveolar geometry (S_e and V_o). For a known alveolar geometry, the model reduces to fitting 6 parameters, the effective elastic modulus for elastin (Y_{ee}) and collagen (Y_{ce}), the minimum and maximum waviness of collagen (w_1 and w_2 respectively), and the two beta distribution shape parameters (α and β).

The full derivation of Eqs. 5.1-5.11, which also includes equations for engineering stress, uniform fiber distribution, alveolar elastance, and tension, is given in Appendix C.1.

5.2.2 Data fitting

In order to find proper parameter values within the physiological range, we first fitted experimental data as follows. A healthy adult P-V curve published by Clements et al. [122] was fitted using the model Eq. 5.9. The P-V curve was recorded in an isolated

lung that was first degassed, inflated to total lung capacity (TLC) then deflated to zero pressure and volume. Several mechanisms contribute to the P-V curve [123]. To minimize the influence of recruitment and alveolar wall folding, only the deflation limb was used in the fitting. Residual volume (RV) was assumed to be equal to the volume at 0 deflation pressure. We assumed homogeneity and isotropic expansion of all alveoli. Thus the change in alveolar volume over the initial volume $\left(\frac{\Delta V}{V_o} = \frac{V_{alv} - V_o}{V_o}\right)$ for a single alveolus is equivalent to that of the whole lung. Assuming a quasi-steady deflation process, the pressure is homogenous throughout the lung.

A value of 1.05 was used for outer to inner radius ratio (S_e) based on the following: Gehr et al. [124] measured and reported the air-blood barrier to be around 2.2 μm in humans. Mercer et al. [125] later measured this across species showing that it increased with body mass with values between 3 to 4 μm for humans. The air-blood barrier which consists of the alveolar epithelial cells, interstitium, and endothelial cells is around half-the alveolar wall thickness [125]. Thus, the estimated total alveolar wall thickness is between 4 to 8 μm. At functional residual capacity (FRC), the alveolar radius is around 100 μm [66]. RV is around 0.6 times FRC for an adult [126], thus at RV the alveolar radius is around 84 μm. Using an alveolar thickness of 4 um leads to an S_e of 1.05.

To verify that the microscopic values obtained from fitting the macroscopic P-V curve are physiologically appropriate, we also verified the model at a much smaller scale. In particular, we fitted the model to two stress-strain curves collected by Sugihara et al. [127] of lung micro-strips containing only a few alveoli from the lung of a young healthy female and an elderly male with obstructive pulmonary syndrome. In this case, we fixed

the shape parameters of beta distribution at the values obtained from the P-V curve fit assuming no inter-individual variation of the shape of the waviness distribution. However, we assumed that the excised tissues lost their in vivo prestrain [113,119] which led to higher w_1 and w_2 values without a significant change in fiber effective elastic modulus. For fitting the tissue strip stress-strain curves, the equations were adjusted for the case of uniaxial stretching (Appendix C.2).

Finally, after verifying that the data fitting reproduced comparable parameters from the P-V and stress-strain curves, we quantified the model's resulting stress on individual fibers as a function of λ_i (see Appendix C.1 for details) as well as the overall fiber contribution to wall circumferential and radial stresses. Then, we related these different stresses to P_{alv}. Since the model fitting only provides an effective elastic modulus without information on the fiber area fractions, we estimated area fractions from literature. Mercer and Crapo [117] reported that volume fractions of collagen and elastin in the human lung far from the alveolar duct are around 0.08 and 0.05, respectively. Images from literature [117,128] show fibers running almost in parallel to the alveolar wall and thus are of comparable length. The area fraction can then be estimated as the volume fraction.

5.2.3 Sensitivity analysis

After finding a set of parameters that captured physiological behavior through model fitting, we used this set as our baseline values. Each baseline parameter was then varied individually in order to investigate its effect on the P-V curve. We varied the 6 fiber parameters, S_e, and in one additional simulation, we also varied the minimum and maximum waviness of the fibers across the wall thickness. For the latter simulation, instead

of keeping w_1 and w_2 constant across the wall thickness (independent of *S*), we made them a function of *S* ($w_1(S)$ and $w_2(S)$) (see Appendix C.1 for details).

5.2.4 Alveolar inflation stability

Guided by the sensitivity analysis, we investigated whether our model shows tensile instability, and if so under what conditions. Thus, the baseline P-V curve was plotted to higher pressures (~40 cmH_2O at $\Delta V/V_o$ = 4 or λ_i=1.71) along with five additional simulations using engineering stress, lower Y_{ce}, smaller S_e ratio, a Gaussian waviness distribution with the same waviness range, and a Gaussian distribution with the same minimum waviness but different maximum waviness (1.92) such that the modes of the two Gaussian distributions were the same (most fibers are recruited at the same time).

5.2.5 Collagen waviness

To support our findings which suggest an important role for fiber waviness in alveolar inflation stability, we investigated the waviness of collagen in lung tissue. Fresh bovine lungs (Research 87 Inc., MA) were obtained and imaged on the same day. Tissue samples, with a length and width less than 1 cm and a thickness of a mm, were cut using a razor, placed on a cover slip (76 x 24 mm), and glued at the sides without inducing any tension in the tissue. The cover slip was previously glued to a 3-D printed rectangular well. The well was 86 x 44 x 10 mm in length, width, and depth respectively, and had a cut out opening of 66 x 17.5 mm in length and width, respectively, onto which the cover slip was glued. The samples were placed in phosphate buffer solution (PBS). Before imaging, the PBS around the tissue was eliminated, the well was inverted and oil was placed on the other

side (no tissue) of the cover slip for upright microscopy imaging. If needed, imaging was suspended and drops of PBS, via a syringe, were added to assure the samples remained moist.

Imaging of collagen in the bovine lung samples was accomplished through Second-Harmonic Generation (SHG) imaging with an upright Multiphoton Microscopy (MPM) system (Ultima Investigator, Bruker, Billerica, Massachusetts). Details of the MPM system are described in detail elsewhere [129]. Briefly, the MPM system consisted of a femtosecond tunable laser source (Spectra Physics, Insight DS+, Santa Clara, CA, USA) tuned to 1050 nm, providing the illumination light for SHG imaging. The illumination light was passed through a Pockels cell (Model 350-80LA EOM, Model 302RM Driver, Conoptics, Dan- bury, Connecticut) to control the power of the illumination light at the sample. A quarter wave-plate (QWP) (AQWP05M-980, Thorlabs, Newton, New Jersey) was placed in the illumination path, circularly polarizing the illumination light to sample all possible collagen orientations during SHG imaging. The illumination and SHG light paths were coupled through a 60x oil-immersion objective (NA = 1.42, working distance = 0.15mm) (Olympus, Tokyo, Japan). A photomultiplier tube (Hamamatsu Photonics, R6357, Hamamatsu City, Japan) was used to detect the SHG light through a 525/70 nm bandpass filter (Chroma, Bellows Falls, VT, USA). The field of view (FOV) was 156 x 156 μm (1024 x 1024 pixels), with a sampling resolution of 153 nm/pixel. A Z-stack was collected for each FOV. Number of slices per Z-stack and step size varied between 10-15 slices and 1–2 μm respectively. To reduce noise in Z-stacks every a 2-frame averaging for every image was applied.

For image analysis, the single images of each Z-stack as well as their max intensity projection was loaded into FIJI [130]. An alveolar wall was first located and zoomed into view. Then using the images, the fiber was traced using free form fitted to a spline (Figure 5-2). Every hump consisted of a minimum of 5 points. Then, the arc length across the outlined fiber segment was traced using the free form spline fit. By saving these measurements and exporting them to MATLAB R2018b (MathWorks, CA), the waviness for each fiber, defined as the fiber length over the arc length, was measured. A histogram of waviness was created which was fitted with the beta probability distribution function (Eq. 5.1). Specifically, w_1 and w_2 were fixed from the experimental findings and the beta shape parameter values (α and β) were fitted.

Finally, we incorporated our experimental findings and fitted again the human P-V curve from the literature (Clements et al. [122]). In particular, we fixed the beta shape parameter values (α and β) and the range of fiber waviness ($w_2 - w_1$) and optimized 3 parameters (Y_{ce}, Y_{ee}, and w_1). We then compared the 3 new parameter values with their previous fitted ones.

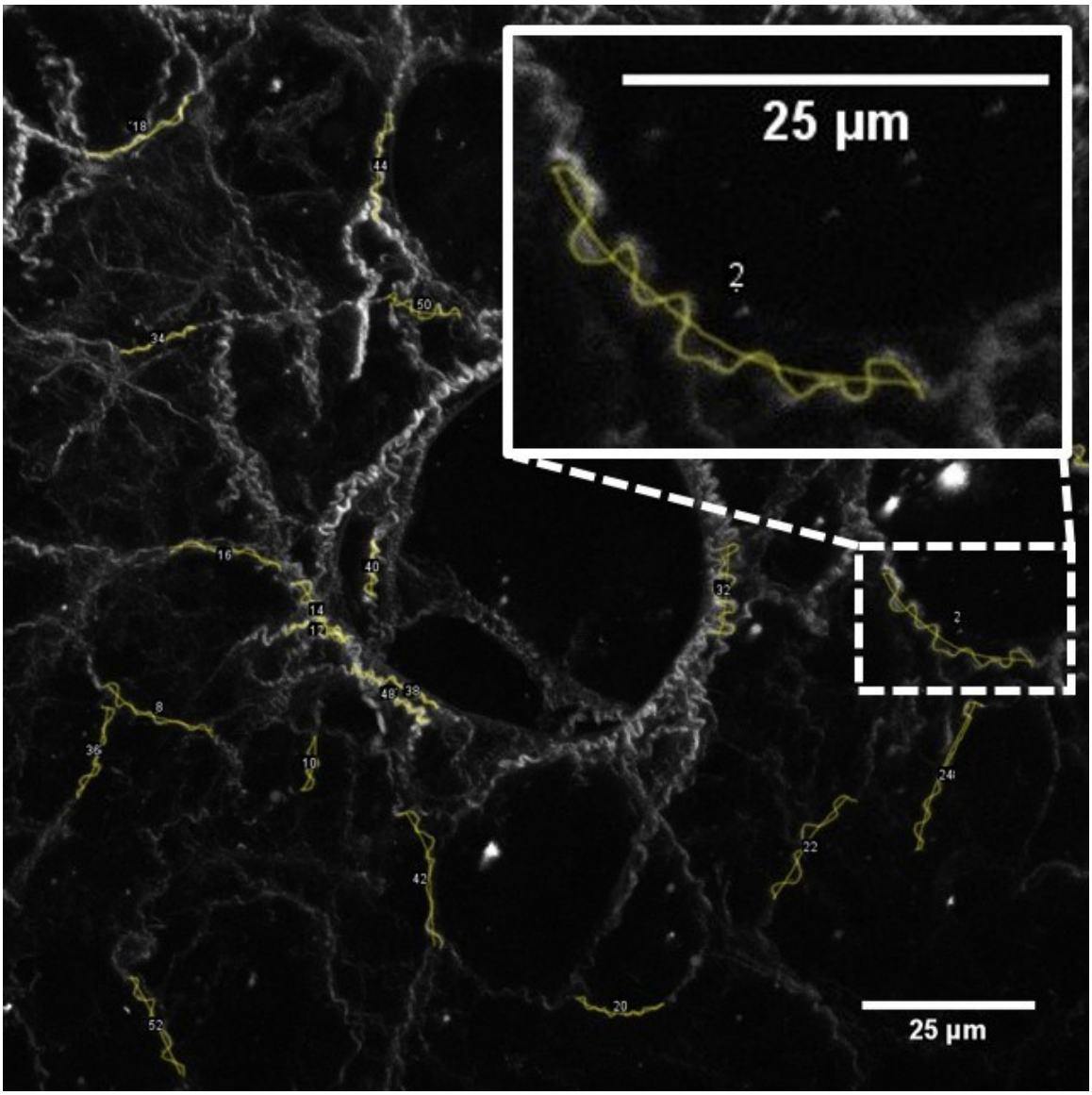

Figure 5-2: Collagen waviness measurement. SHG image example with fiber tracing. Yellow traced lines are drawn over the fiber length and arc length. The former is divided by the latter to find the waviness of a single fiber. The inset shows an enlarged section of a selected fiber.

5.3 Results

5.3.1 Data fitting

Figure 5-3A plots the organ level P-V curve, while Figure 5-3B shows the alveolar wall strip stress-strain curves together with the model fits. The beta shape parameters in the stress-strain curve fits were taken from the P-V curve fit in Figure 5-3A. In both cases, the model provided a good fit of the data with small errors. However, in the case of the elderly subject, Y_{ee} could not be determined likely because it contributed little to the stress. Note that Y_{ce} increased and the waviness range decreased in the old subject compared to the young.

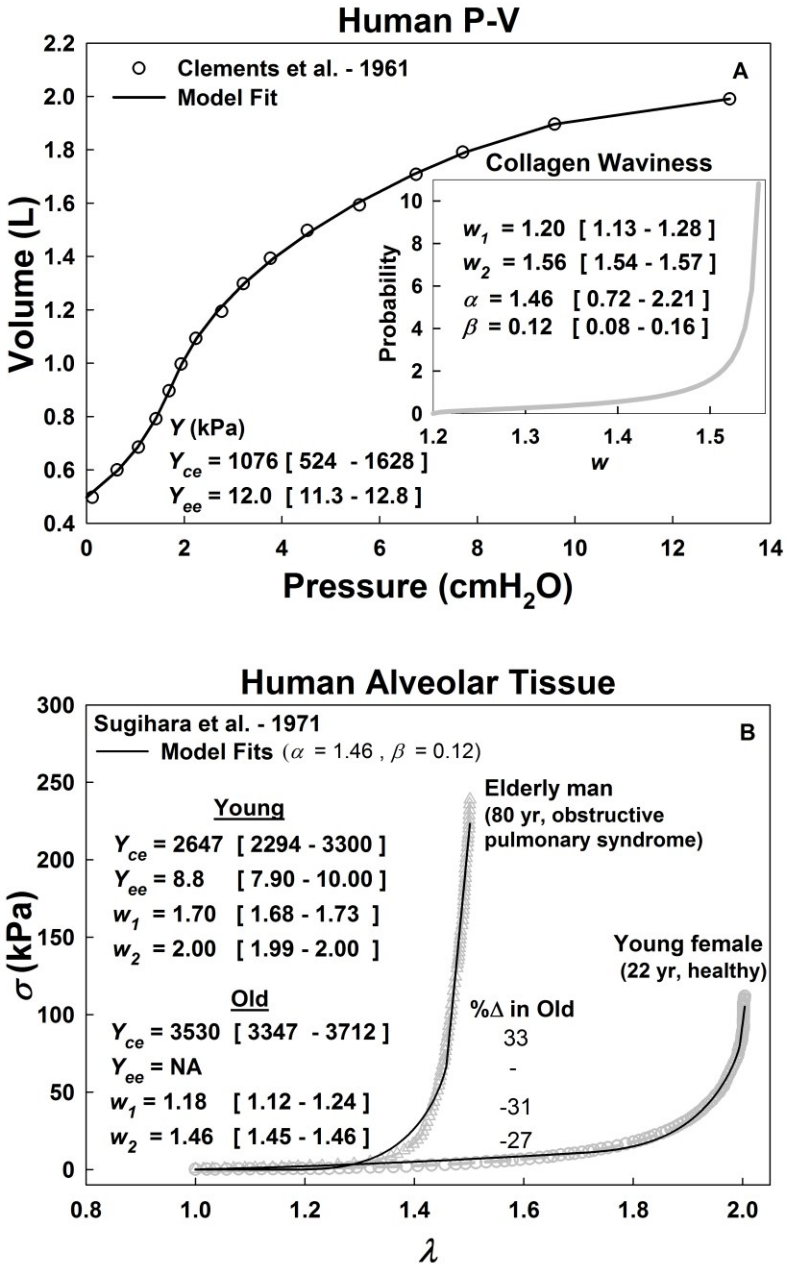

Figure 5-3: Model fitting results. A) Fitting a healthy adult human P-V curve with the six estimated parameters and their confidence intervals. Using the estimated beta shape parameters, the resulting waviness distribution of collagen is shown in the inset. B) Fitting of two alveolar strip stress-strain curves in uniaxial stretch for a young female and elderly male using the shape parameters obtained from panel A and the derived uniaxial equations from Appendix C.2. The estimated parameters and confidence intervals for each are displayed and the percent difference (%Δ) from young to old is evaluated. Y_{ce}: collagen effective elastic modulus. Y_{ee}: elastin effective elastic modulus. w_1: minimum collagen waviness. w_2: maximum collagen waviness. α and β: beta distribution shape parameters.

Once the model was fit to the macroscopic P-V curve as in Figure 5-3A, it allows us to predict microscopic fiber stresses shown in Figure 5-4. For example, during spontaneous breathing the trans-alveolar pressure varies between 5 (at FRC) and 10 (FRC + tidal volume) cmH_2O at expiration and inspiration, respectively [113]. From Figure 5-3A, these pressures correspond to $\Delta V/V_o = 1.55$ or $\lambda_i = 1.36$ (Eq. 5.11) and $\Delta V/V_o = 1.92$ or $\lambda_i = 1.43$ respectively. Given, the inner stretch ratio, we can find the stretch ratio at any internal layer from the conservation of mass (see Appendix C for details) as shown in Figure 5-4A. Thus, around normal breathing the stress on the elastin fibers can reach 90 kPa with small variations across the layers (Figure 5-4B). This value can rise to 120 kPa as the lung approaches TLC. In contrast and interestingly, collagen is already recruited within that range but at a very low percentage (<10%, Figure 5-4C). Specifically, recruitment starts at $\Delta V/V_o = 0.72$ or $\lambda_i = 1.2$ and is gradually and slowly increasing across the normal breathing pressures. Only beyond that and around $\lambda_i = 1.56$ recruitment suddenly jumps to near 100% (Figure 5-4C). Furthermore, the recruitment highly depends on the location within the wall. For example, at $\lambda_i = 1.6$, 100% of the collagen fibers at the inner layer are recruited while only 20% are recruited in the outer layer. Figure 5-4D shows the stress distribution at $\lambda_i = 1.6$ based on the initial collagen waviness distribution (Figure 5-3A inset). At this stretch ratio, most of the fibers have a stress of 0.4-1 MPa while very few can reach to 4.5 MPa.

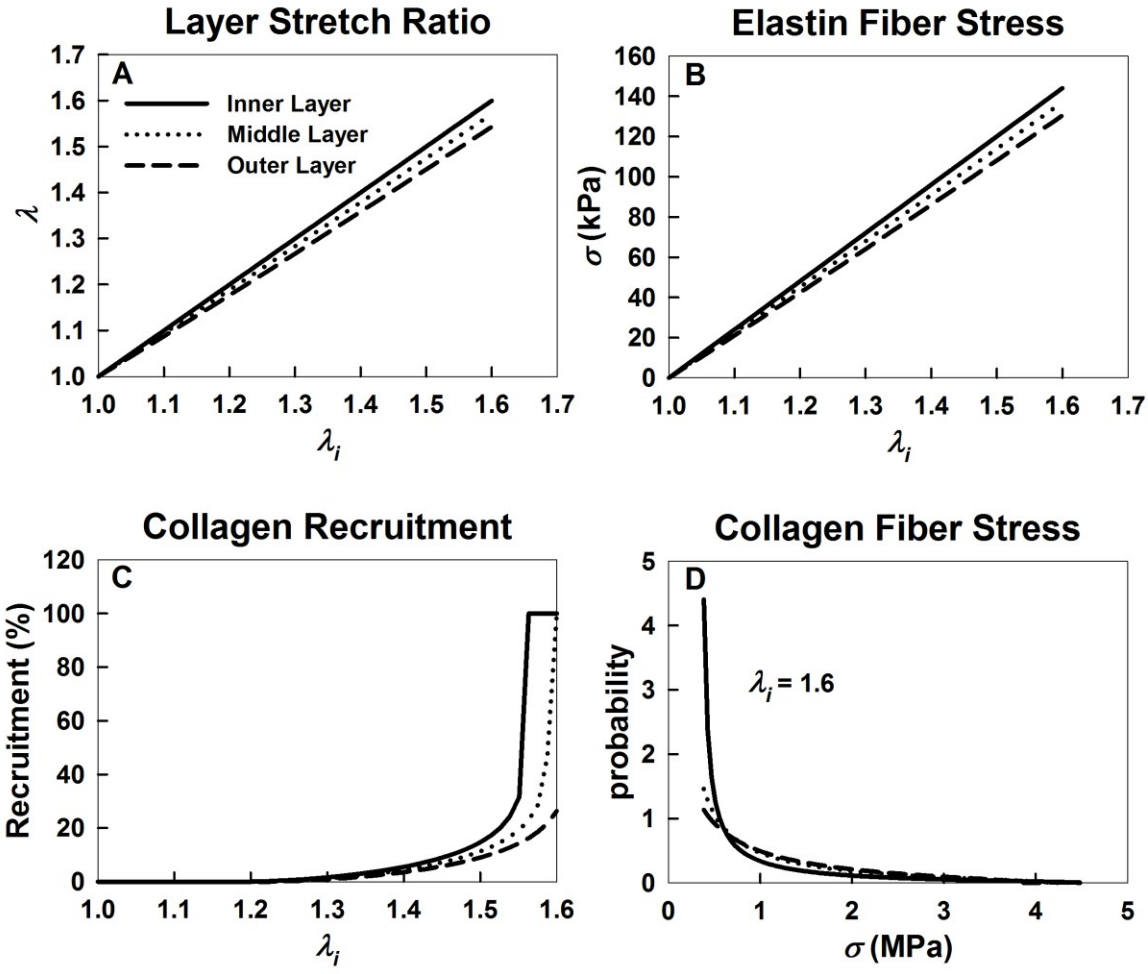

Figure 5-4: Single fiber analysis. A) Due to the spherical geometry alveolar wall layers will have different strains resulting in different fiber stresses within each of the three layers (inner, middle, and outer layer). B) Elastin fiber stress as a function of inner layer stretch ratio (λ_i). C) Collagen recruitment as a function of λ_i. D) Collagen stress distribution at λ_i=1.6.

From the fitted parameters, we can also estimate alveolar wall stresses. Figure 5-5 plots the circumferential and radial alveolar stresses for three different layers (inner, middle, outer) as well as the mean. The contribution of elastin and collagen to the alveolar tissue stress across different layers is shown separately (rows 1 & 2), and the total alveolar values are displayed in the last row with the percent contribution of collagen from the total stress for the middle layer displayed at specific inner stretch ratios. In every case, the results for the mean and the middle layers are nearly identical. Interestingly, even though elastin is neither wavy nor nonlinear its resultant stress is a nonlinear function of the stretch ratio. This nonlinearity arises from normalizing the force developed by elastin with the deformed tissue area (true stress).

Finally, we can also relate the alveolar wall circumferential stress and fiber stresses to the P_{alv} (Figure 5-6). Interestingly, the findings reveal that the stress increases approximately by an order of magnitude from P_{alv}, to alveolar circumferential stress, to elastin fiber stress, and to finally maximum collagen fiber stress.

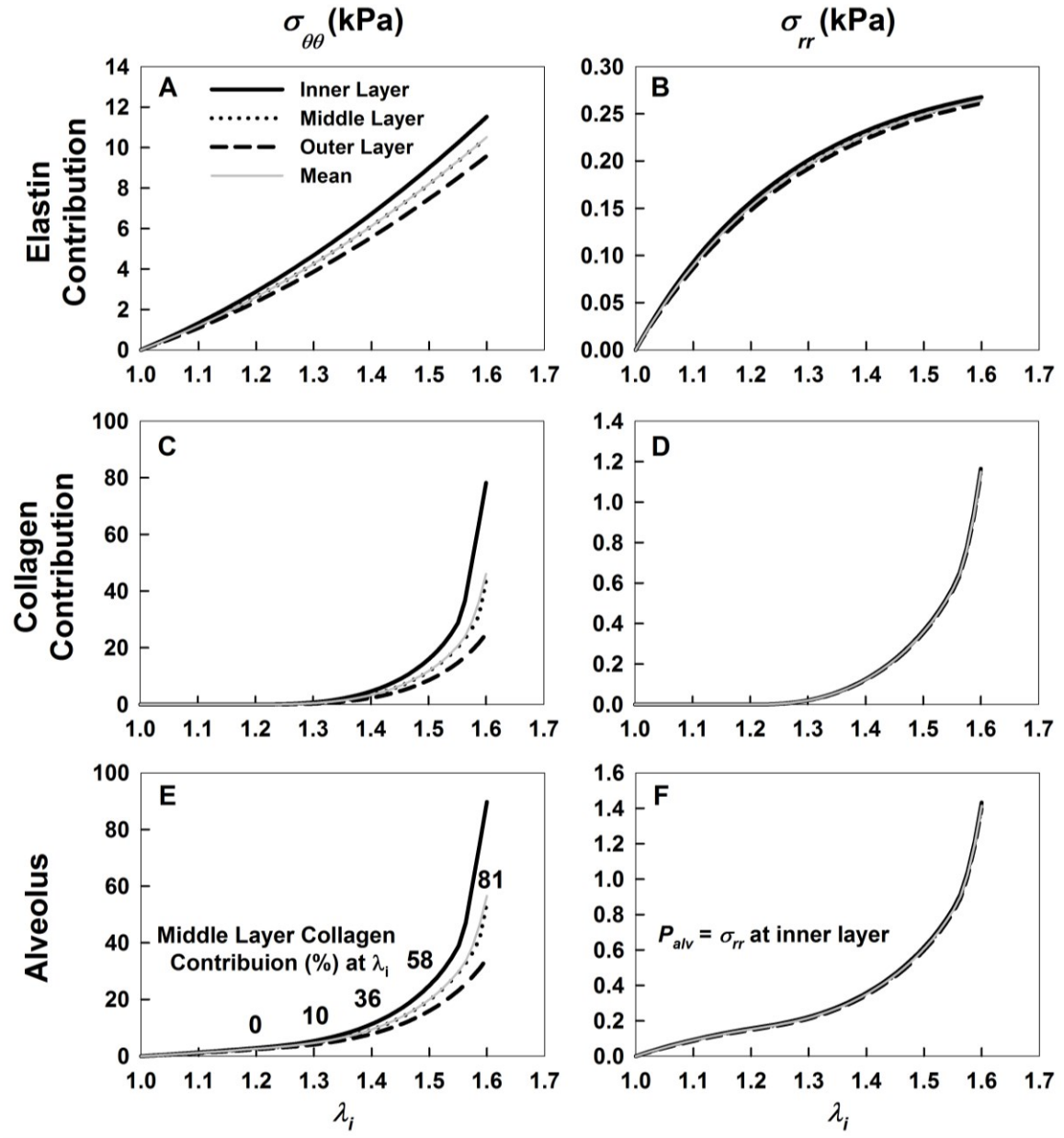

Figure 5-5: Alveolar stresses. Rows represent the contribution of elastin (row 1), collagen (row 2), and their combined effect (row 3) for the circumferential stress (column 1) and radial stress (column 2) calculated analytically for the three different layers (black lines) and the numerically integrated mean (gray line). Percent contributions of collagen to the total stress are shown in Figure 5-5E at specific inner stretch ratios. Note that the percentage contribution is the same for both circumferential and radial stresses. The alveolar pressure is equal to the radial stress evaluated at inner layer.

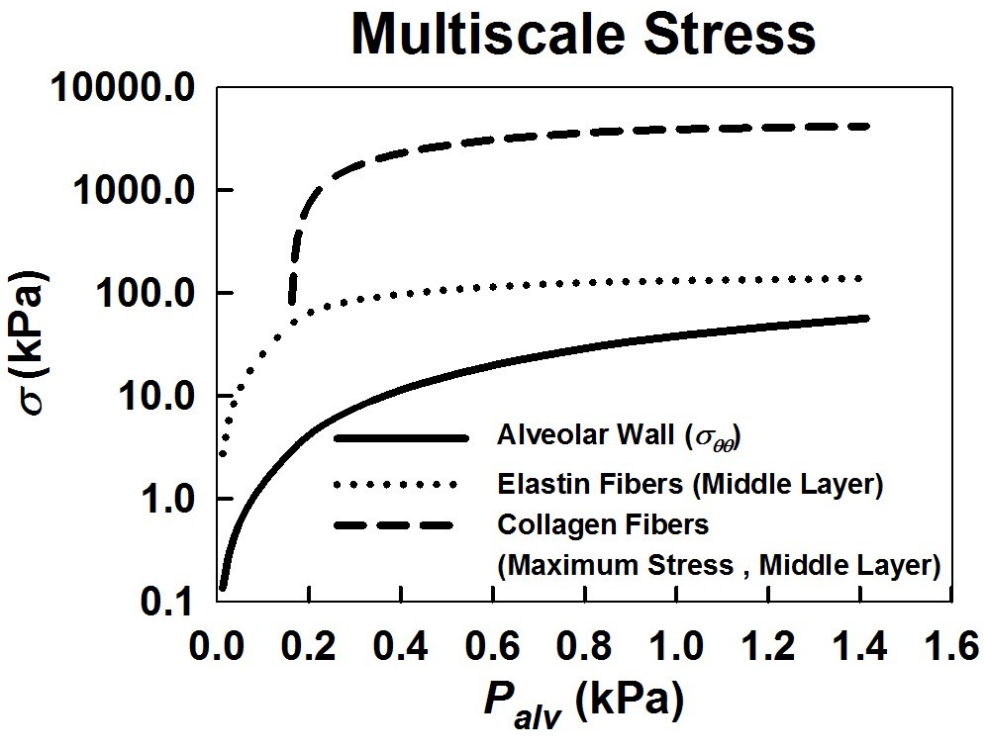

Figure 5-6: Multiscale stress. The alveolar wall, elastin, and collagen stresses can be related to P_{alv}. The middle layer for elastin and collagen fibers are shown, and in the case of the latter, the maximum stress is represented.

5.3.2 Sensitivity analysis

To evaluate how sensitive the results are to changes in parameters, we present in Figure 5-7 the effects of varying several parameters on the P-V curve. Allowing the maximum and minimum waviness to vary across the layer (see Appendix C.1 for details) did not have a considerable effect on the P-V curve (Figure 5-7A). Doubling or halving S_e, however, considerably changed the P-V curves reaching 86% and -48% at $\Delta V/V_o$ =1, respectively (Figure 5-7B). The effect of doubling or halving Y_{ee} reached differences compared to baseline P_{alv} values as high as 97% and -48% at $\Delta V/V_o$ =1, respectively. Elastin had a diminishing effect on the P-V curve at higher $\Delta V/V_o$ (Figure 5-7C). On the other hand, Y_{ce} had a much stronger effect on P_{alv} at higher $\Delta V/V_o$ reaching 78% and -49 when doubled or halved, respectively (Figure 5-7D). The waviness range and shape parameters of the beta distribution were studied simultaneously. A slight downward shift (<10%) of the fiber waviness range dramatically pushed the P-V curve to the right with a value as high as 238% at $\Delta V/V_o$=3, representing faster collagen recruitment (Figure 5-7E). Notably, using a uniform or Gaussian distribution with the same waviness range as the baseline beta distribution resulted in a very stiff P-V curve, while shifting the mean waviness to the right (left-skewed distribution) resulted in a P-V curve that was closer to the baseline (Figure 5-7F).

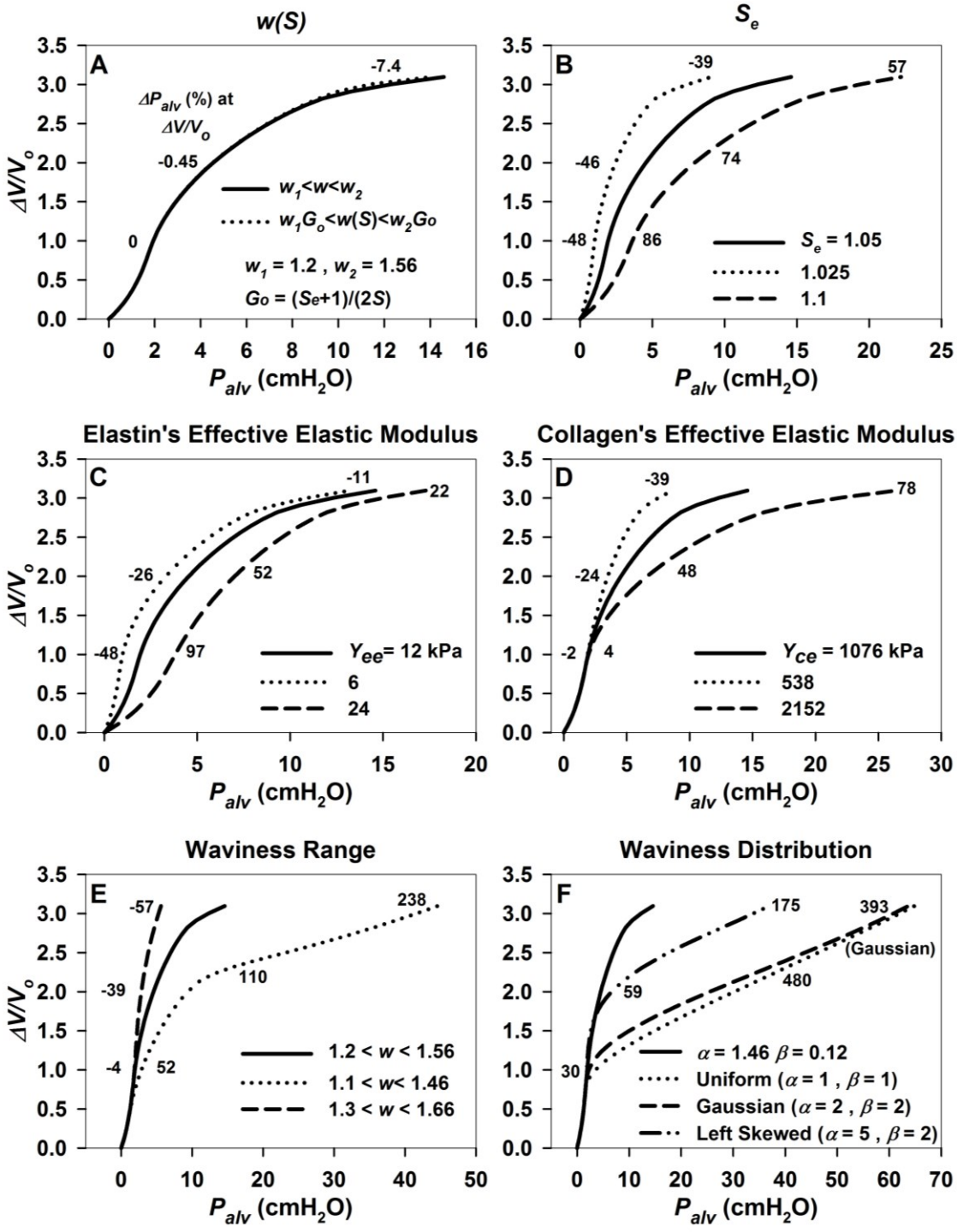

Figure 5-7: Sensitivity analysis. The effect on the P-V curve was studied for A) varying waviness across the alveolar wall B) outer to inner radius ratio (S_e) C) elastin effective elastic modulus, D) collagen effective elastic modulus, E) waviness range, and F) waviness distribution beta shape parameters. Percent differences in P_{alv} from the baseline simulation are indicated next to each curve for $\Delta V/V_o$ of 1, 2, and 3.

5.3.3 Alveolar inflation stability

Using the fitted parameters and further inflating the alveolus from $\Delta V/V_o$ of 3 to 4 (33%), which corresponds to less than 7% in stretch ratio (1.6 to 1.71), led to a 170% drastic increase in pressure (from 14 to 40 cmH_2O) (Figure 5-8). More importantly, there was a volume plateau signifying inflation stability or protection against over distention. The pressure calculated from the engineering stress, however, shows a yielding phenomenon as well as considerably higher $\Delta V/V_o$ above 20 cmH_2O pressure compared to the true pressure (using true stress). Instability also emerges in the case of low Y_{ce} and S_e. Maintaining the same waviness range (1.2-1.56) but applying a Gaussian distribution, the P-V curve still maintained a stable plateau. However, $\Delta V/V_o$ tremendously decreased. Although not as drastic, that was also the case for using another Gaussian distribution with equal mode (compared to baseline). However, more importantly, the P-V curve did not achieve the stability plateau, and the P-V slope was much higher than baseline.

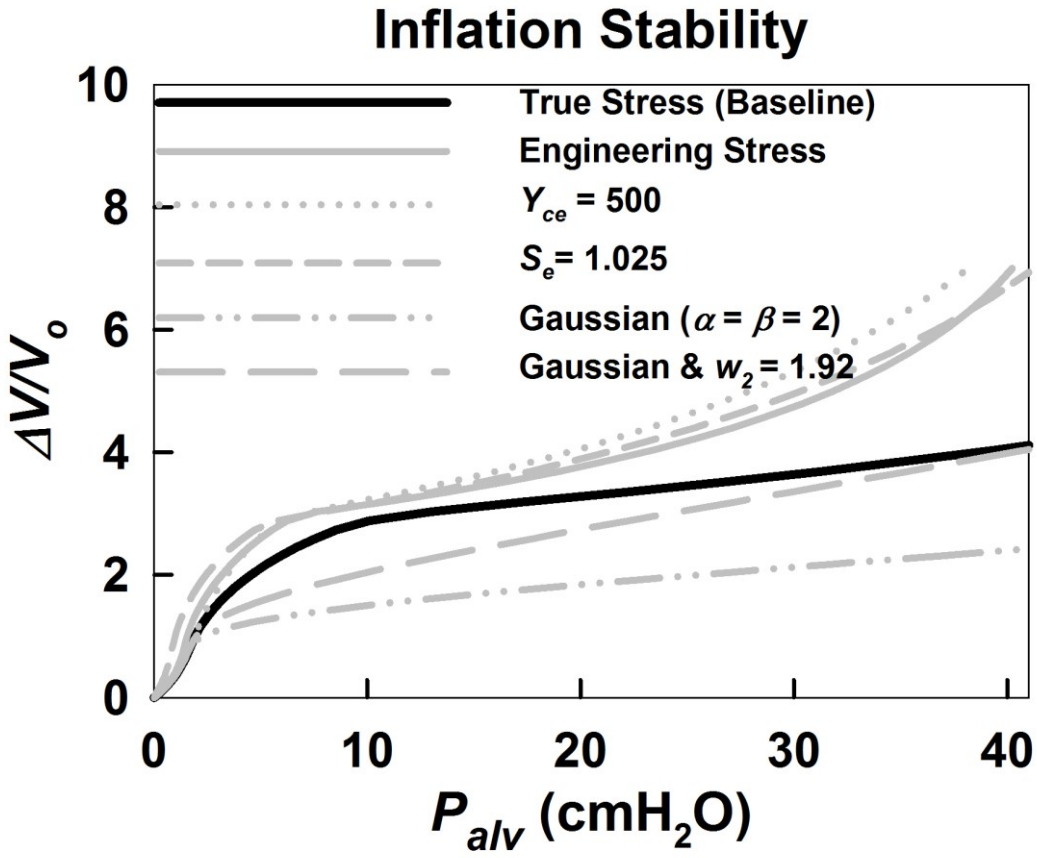

Figure 5-8: Inflation stability. P-V curves based on true stress (black solid line), engineering stress (gray solid line), reduced Y_{ce} (dotted gray line), reduced S_e (gray short dashed line), Gaussian distribution with same waviness range (dash-dot line) and Gaussian distribution with equal mode compared to baseline (medium dashed lines) at higher pressures.

5.3.4 Collagen waviness

Figure 5-9 shows the probability distribution function of the experimental results for the fiber waviness. In contrast to the resulting collagen waviness obtained from model fitting, the experimental distribution, shows a much wider range of waviness (1.12-2.53) compared to the model-based waviness (1.2-1.56). This finding suggest that the collagen waviness distribution provided by the model only captures the range across which the pressure is measured.

Figure 5-10 incorporates the experimental findings, the beta shape parameter values (α and β) and the range of collagen waviness ($w_2 - w_1$) and compares the previous fit with 6 parameters to the new one with only 3 parameters (Y_{ce}, Y_{ee}, and w_1). The values of the 3 common fitted parameters were close to each other before and after incorporating the experimental waviness measurements.

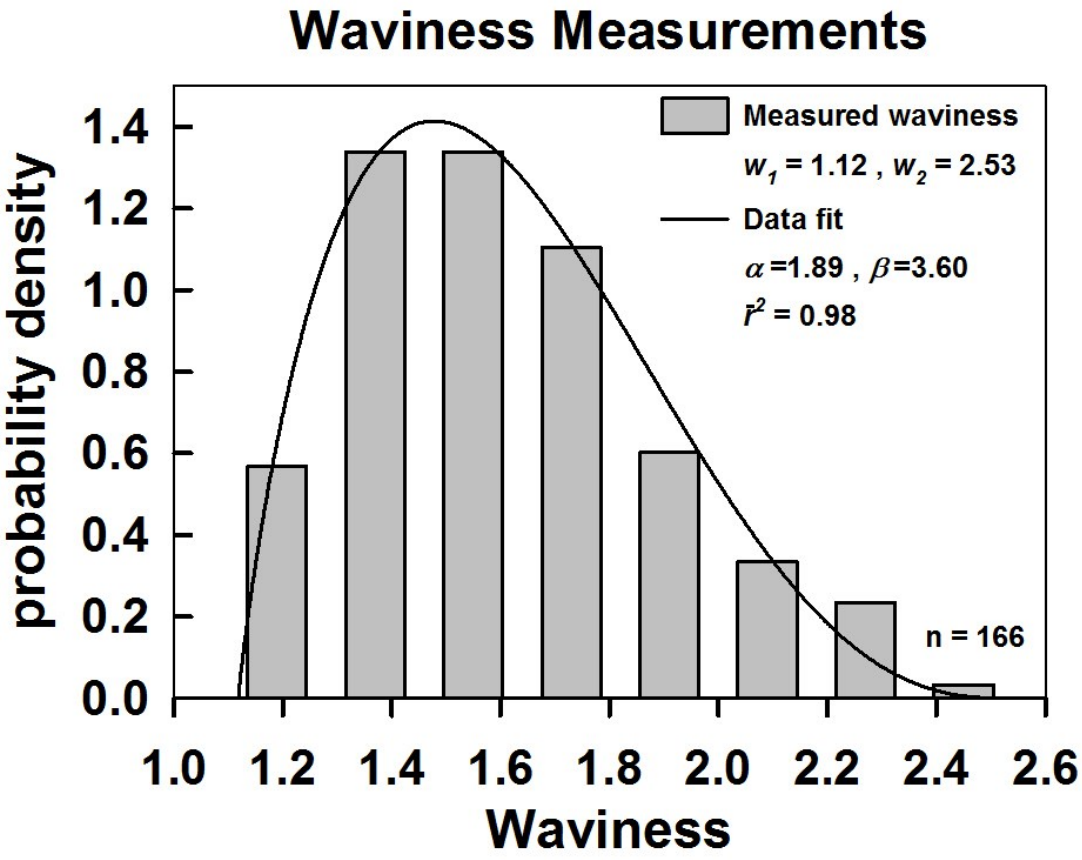

Figure 5-9: Collagen waviness results. Histogram and fit for all 166 measured fibers. Gray bar graph represents the experimental collagen waviness, while the solid continuous line is the fit using the beta distribution (Eq. 5.1). The adjusted coefficient of determination $\bar{r}^2$ is equal to 0.98 and α and β are 1.89 and 2.53 respectively. The minimum and maximum experimentally measured waviness values were 1.12 and 2.53, respectively.

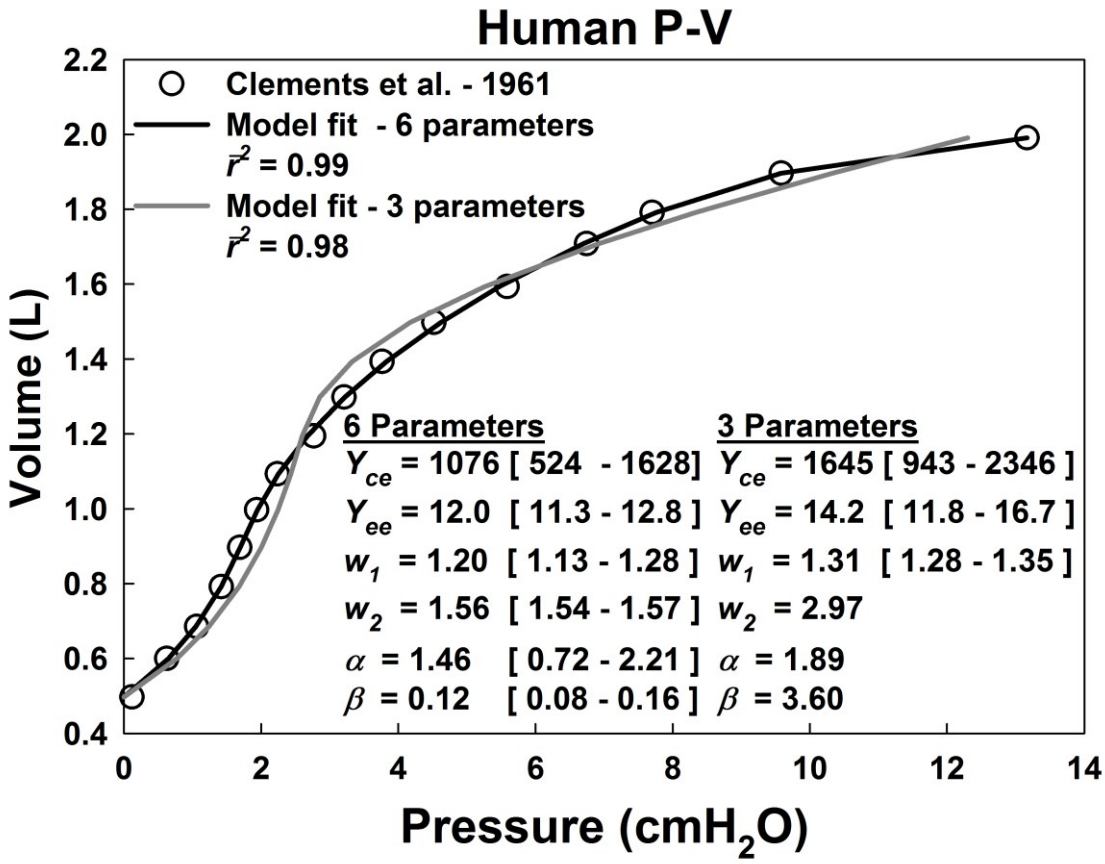

Figure 5-10: Results of fitting the 6- versus 3-parameter models. Fixing α, β, and the range of collagen waviness ($w_2 - w_1$) from the experimental waviness measurements, Y_{ce}, Y_{ee}, and w_1 were fitted. Compared to the 6-parameter fit these values were very similar. For the 3-parameter fit, the parameters without the interval range were not fitted but evaluated experimentally.

5.4 Discussion:

In this study, we developed an analytic thick-walled model of a single alveolus containing elastin and wavy collagen fibers embedded in the tissue matrix undergoing large deformations during inflation. The model allowed the estimation of collagen and elastin effective elastic modulus and the waviness distribution of collagen. Simulations provided new insight into the role fibers and their recruitment plays in alveolar mechanics and inflation stability (protection from over distension). Unlike the traditional view that attributes the inflation stability to the nonlinear behavior of collagen fibers, we have demonstrated that inflation stability can be achieved through linearly elastic but wavy collagen fibers. Measuring collagen waviness experimentally, we observed a large range of waviness values in support of this finding. Furthermore, we shed light on the importance of computing true stresses to accurately predict alveolar stresses and strains during inflation. Since alveolar strains significantly influence cellular behavior [45,54,131–135], our model also helps quantify the stresses and strains within the septal wall in both healthy and diseased alveoli with possible implications for drug treatments and mechanical ventilation strategies.

5.4.1 Data fitting

Collagen elastic modulus has been evaluated to be around 100 MPa [136,137], while elastin fibers have been reported to have an elastic modulus between 0.5 and 1 MPa [95,138,139]. Using the area fractions deduced from Mercer and Carpo [117], the effective elastic modulus (elastic modulus times area fraction) of collagen and elastin are in the order of 10^3 and 10 kPa, respectively, which are comparable to our model-based estimates

(Figure 5-3). Apart from species-related differences, the effective elastic modulus of collagen evaluated from the tissue strips is more consistent with literature. The difference in the collagen's effective elastic modulus estimated from the tissue stress-strain and P-V curve is likely due to P-V curve hysteresis as well as uneven boundary effects in the tissue strip. From Figure 5-7D, we can observe that a reduced collagen effective elastic modulus shifts the P-V curve to the left, and hence the effect of hysteresis leads to an underestimation of collagen effective modulus. Nevertheless, our estimates are still in the range of literature-based values.

From the P-V curve fitting, the large confidence intervals for collagen fiber effective elastic modulus and beta shape parameters signifies that they have similar roles in defining specific features of the P-V curve. Indeed, our sensitivity analysis suggests that they affect the P-V curve in similar ways (Figure 5-7D and 5-7F). By keeping the beta shape parameters constant, the effective collagen elastic modulus confidence interval dropped significantly from 51% from the P-V curve to 25% and 10 % from the stress-strain curves of the young and old tissue strips, respectively. Furthermore, the alveolar wall stresses in the young tissue strip (Figure 5-3B) are similar in magnitude to those calculated ($\sigma_{\theta\theta}$ in Figure 5-5E) from the model fit to the P-V curve.

The beta distribution parameters (α and β) define the shape of the collagen waviness distribution (Figure 5-3A inset) which suggests that collagen fibers are first recruited very slowly during the inflation followed by a sudden acceleration of recruitment (Figure 5-4C) consistent with the documented role of collagen fibers as well as their low extensibility [118,138,140,141]. However, our results also imply that collagen recruitment

starts at as low strain as 0.2 corresponding to $\Delta V/V_o$ of 0.7. The estimated collagen waviness range (1.2-1.56) generates a maximum collagen extension of 30%, which is only 10% more of what is reported to be the maximum strain for stiff collagen fibers [138]. Nevertheless, the majority of fibers are not recruited until λ_i reaches 1.5 which results in 3.3% extension in the model consistent with the proposed inextensibility of collagen fibers [142,143]. Elastin fibers, on the other hand, are extended by 160% which is closer to their limit [138].

The difference in the waviness range of fibers ($w_2 - w_1$) is consistent between the P-V curve (0.36=1.56-1.2) and the tissue strips (0.3=2-1.7). However, the difference in absolute values between w_2 and w_1 could be attributed to the prestress which is known to play a critical role in lung mechanics yet is not quantitatively measured for the lung parenchyma [113,119]. By dividing w_2 and w_1 obtained from the P-V curve by w_2 and w_1 obtained from the tissue strips respectively (2/1.56 and 1.7/1.2), our findings suggest that the prestress generates a prestrain that is between 30-40%.

5.4.2 Alveolar inflation stability and collagen waviness

The role of surfactant in lung deflation stability has been extensively studied [45,69,74,144]. However, surfactant does not play a major role in alveolar mechanics at higher lung volumes compared to collagen fibers. During inflation, there can be another type of instability associated with the fact that surface and volume increase faster than pressure leading to a runaway phenomenon. Both deflation and inflation instability can be best understood through the Laplace law:

$$P_{alv} = \frac{2(T_f + \gamma)}{r_i} \tag{5.12}$$

where T_f and γ are the tension due to the fibers and surface tension due to surfactant respectively. As the alveolus deflates, surfactant reduces γ at a faster rate than r which decreases P_{alv}; otherwise, the decreasing r_i would increase P_{alv} which results in the smaller alveolus emptying into larger ones and full collapse. This is referred to as deflation instability. On the other hand, during inflation, r_i increases which decreases P_{alv} and thus further inflating the alveolus becomes progressively easier leading to an infinitely large volume in the limit. However, experiments clearly show that the volume reaches a plateau increasing very slightly with pressure [6]. Therefore, T_f/r_i must increase with r_i faster than $\Delta V/V_o$ which is a function of r_i^3 which means $T_f/r_i \sim r_i^n$ where $n>3$. When we combine the stress equation from the collagen fibers during recruitment (Eq. 5.3) with the equation of tension (Appendix C.1, Eq. C.64), we find that the tension from the fibers varies with r_i as $T_f \sim r_i^{3+\alpha}$. Since $\alpha>1$, stability is satisfied and this is when we observe a concavity in the P-V diagram. However, after the full recruitment of the fibers this is no longer the case ($T_f \sim r_i^3$). This could explain why the experimental waviness measurements resulted in a large range of collagen waviness. In brief, this large range could act as a safety net assuring inflation stability. Interestingly, after full collagen recruitment, due to the combination of high collagen elastic modulus, mass conservation, and appropriate S_e ratio, yielding can be delayed though it is eventually inevitable (Figure 5-8). Furthermore, since the uniform and even the Gaussian distribution of waviness still leads to a linearly increasing volume without a clear plateau (Figure 5-7F), a key modeling result is that stability requires a

specific waviness distribution that allows sudden recruitment of a large fraction of collagen at pressures near TLC. Additionally, these features of the waviness distribution are critical in achieving the required TLC value at physiological pressures (Figures 5-7F and 5-8).

5.4.3 Physiological implications

The consistency between the analytically calculated values at the middle layer and numerical integrated mean (Figure 5-5) signifies that a single layer of fibers can achieve the same pressures as multiple layers. This is relevant because the alveolar interstitium, which includes fibers as well as other components, takes up only 56% of all the alveolar wall [124]. More importantly, this allows to analytically relate the stresses at different levels (Figure 5-6). This will be key for reducing VILI or designing mechanotransduction based experiments.

The sensitivity analysis in Figure 5-7 provides important physiological insight into alveolar mechanics. For example, changes in alveolar wall thickness result in large changes in the P-V curve and hence lung compliance (Figure 5-7B). This has implication for emphysema. For example, Szapiel et al. [145] showed that the tight skin mice with spontaneous emphysema had thinner alveolar walls compared to normal mice. Even though elastin content is decreased in these mice [146] , our model shows that reduction in thickness has a much more significant influence on physiology than reduction in elastin especially since elastin only plays a role in the lower region of the P-V curve (Figures 5-7B and 5-7C).

Our model analysis also allows the estimation of the separate contributions of structure (e.g. wall thickness and waviness) and constituent properties (e.g. elastic

modulus) to the P-V curve. Sugihara et al. [127] did not separate these two factors and justified the observed increase in resting length due to a permanent deformation of elastin and the sudden sharpness in stress due to collagen acting as a fixed mechanical stop. It is currently not known whether parenchymal reorganization or changes in fiber stiffness contributes more to the observed physiological phenotype of a given disease. Collagen content has been shown to increase in the aging lung [147], while an organizational change in the parenchyma has been shown to play a role in both fibrosis and emphysema [148,149]. Fitting of Sugihara's young and old tissue strip data suggests that both structure and mechanical properties are equally important contributing each by ~30% of the change in stress that occurs with aging (Figure 5-3B). Our sensitivity analysis demonstrates that even a small shift of 9% in collagen waviness drastically alters pressure that cannot be achieved by changing stiffness by 50% (Figures 5-7D vs 5-7E). This implies that the straightening of collagen fibers [150] that occurs in aging or disease [151,152] is mainly responsible for the increased tissue stiffness of the aging lung [153].

An interesting further insight into lung physiology is related to the convexity of the deflation P-V curve. Our simulations demonstrate that this occurs at the level of a single alveolus (e.g. Figure 5-7A at $P<2$ cmH_2O) suggesting that this convexity can be explained by the initial yielding of elastin fibers before collagen recruitment starts. Another finding which opposes classical belief suggests that collagen fibers are being recruited even within normal breathing pressures. This finding has been suggested from other experiments in lung tissue strips as well [154].

5.4.4 Model limitations

Our model is not without limitations. First and most important, the model does not take into account surface tension which plays an important role at low airway pressures [73,144,155] and which will affect the estimated parameters. However, concerning inflation instability and the role of collagen waviness in achieving it, adding surface tension should not affect it for the following reason. Surface tension has been found to increase linearly with volume [155,156]. This suggests, based on Eq. 5.12 that the surface tension contribution to P_{alv} is proportional to r_i^2 which is less than the increase in alveolar volume suggesting that surface tension alone is not able to achieve inflation stability. Second, we assumed linearly elastic collagen fibers. To our knowledge, the stress-strain curves of single fibers isolated from the lung has not been reported yet. However, linear collagen behavior has been reported [157,158]. Third, the model does not include network effects through alveolar interactions and does not consider changes in volume which occur in the alveolar ducts and airways. We also neglect fiber-fiber interactions which could further contribute to alveolar mechanics especially dissipation [159]. However, from images of human lung parenchyma, Matsuda et al. [150] noted that collagen and elastin fiber bundles run parallel to each other without intertwining within the alveolar mouth, then they separate at different locations and run independently from one another within the septal walls. This suggests minimal interaction between the two fiber systems. The model also assumes affine transformation in that the stretch ratio within the wall thickness is transmitted to the fibers. If the deformation was non-affine, then the waviness range would be overestimated. However, the role of waviness and the conclusions drawn would still be the same. In future

work, imaging fiber waviness under stretch could resolve this question. Finally, the lack of a network of alveoli produces a certain asymmetry. In a network, two alveoli share the same septal wall and hence the outside of one is the inside of the other. This may have further limitations on the possible waviness distributions across the wall thickness. More importantly though, a network of alveoli could affect how a single alveolus achieves inflation stability. Nevertheless, despite these limitations, the model offers novel insight on alveolar mechanics and stability as well as provides a framework to estimate ECM stresses and strains vital for mechanotransduction. These new findings and possibilities warrant further investigation into alveolar mechanics and inflation stability.

5.5 Conclusion

Modeling the behavior of elastin and collagen fibers inside thick-walled alveoli under large deformation allowed the quantification of the fiber's contribution and their organization to the P-V curve, uncovered a key role for collagen waviness in achieving P-V inflation stability, and provided estimates of strains and stresses at the level of a single alveolus. The estimation of these stresses is crucial for studying the response of cells to mechanical cues, avoiding tissue damage in ventilator-induced lung injury, and separating structural from material changes in healthy and diseased lungs.

5.6 Acknowledgement

This study was supported by NIH grant U01 HL-139466. We are thankful to Kavon Karrobi and the Biomedical Optical Technologies Lab at Boston University for providing the means and support to image collagen waviness.

Chapter 6: Uniaxial model

6.1 Introduction

The biological and physical properties of the constituents of tissues play important roles in the normal functioning of organs and organisms. These functional properties invariably demonstrate nonlinear mechanical behavior at the macroscopic scale and can be related to tissue structure at the microscale. In particular, the nonlinear stress-strain curve of various tissues at the macroscopic scale has been primarily attributed to microscopic processes such as recruitment of fibers via rotation and/or straightening within the extracellular matrix (ECM) [118,119,160]. An abundance of numerical and analytical models have provided useful insight into tissue function by relating macroscopic stress-strain curves to microscopic fiber properties of collagen and elastin [140,161–163]. For example, Maksym & Bates [140] used a spring-string model to capture the elastic behavior of elastin (as the spring) and the stiff and wavy behavior of collagen (as the string). With their model, insight on the relation between fiber stiffness and collagen stop length were obtained. Decraemer et al. [163] developed a wavy fibril model and showed its application to several tissues including human vein, fascia, tympanic membrane and rabbit papillary muscle. Liao & Belkoff [162] expanded on the model and provided an analytical solution for wavy parallel collagen fibers in the ligament. While these studies did not include the spatial information of the fibers, other models did take into account the structure. For example, Lanir developed a model of wavy collagen and pre-stretched elastin with the ability to rotate and stretch as the tissue was being deformed [161]. Sacks was able to determine fiber orientation using small angle light scattering and numerically solved the

constitutive equations to estimate individual collagen fiber properties and stress-strain curves [164]. In addition to the effects of fiber structure and orientation, the fiber recruitment process and the tissue stress-strain curve has been shown to be governed by both the stiffness of the fibers as well as the ECM stiffness which mainly arises from the repulsion of the negatively charged proteoglycans (PGs) [165,166].

However, directly applying these models to the lung parenchyma is not an adequate representation of the unique structure of the lung. Unlike most other tissue, the lung parenchyma presents a distinctive structure where alveolar walls rotate and elongate during uniaxial stretching of lung tissue strips. Several models were developed particularly for the lung tissue stress strain curves [128,167]. The role of PGs in the mechanical behavior of tissue strips and particularly their effect on alveolar wall rotation was also demonstrated using such models [128,168]. While these specific parenchymal models provide very useful insight on the microscopic lung properties, to our knowledge, these models mainly utilize numerical approaches which render them computationally exhaustive especially in fitting experimental data. The primary objective of the present study was to develop an analytical model that allows the separate estimation of the alveolar tensile elastic modulus and the rotational elastic modulus, defined as an increase in stress due to a small rotation normalized by the change in angle, from experimental stress-strain data obtained under uniaxial stretch.

In the current study, we first present the theory describing the simultaneous rotation and tensile stretching of a representative alveolar wall during uniaxial stretching of a tissue strip. Next, through several forward simulations, a physiologically-sound range of

parameters is deduced and their sensitivity on the stress-strain curves is examined. To assess model credibility, the stress-strain behavior is compared (1) computationally to a previously developed network model in its ability to estimate the parameters and microscopic alveolar strains and angles and (2) experimentally by fitting stress-strain curves of two different treatment conditions. Finally, to investigate how alveolar wall and fiber elastic modulus change with age, the stress-strain curves of young and old mouse tissue strips were fitted with the model.

6.2 Methods

6.2.1 Model development

Assume that a 2-dimensional piece of lung tissue with length L and width W is stretched uniaxially from one end while the other end is fixed. Stretching progresses from current step $s-1$ to the new step s ($s = 1,2 \ldots$) (Figure 6-1A). The tissue is composed of a network of hexagonal alveoli which can be partitioned into N alveolar walls (Figure 6-1A) with a tensile elastic modulus Y_a and rotational elastic modulus Y_b. The alveoli are air or fluid filled and the total volume fraction of alveolar walls is $\delta_{V,w}$, and the effective alveolar tensile and rotational elastic modulus are defined respectively as $Y_{ae} = Y_a\ \delta_{V,w}$ and $Y_{be} = Y_b\ \delta_{V,w}$. A single alveolar wall has a current length l_{s-1} corresponding to the current alveolar strain ε_{s-1} and is oriented at an angle θ_{s-1} with respect to the direction of the tissue stretch (Figure 6-1B).

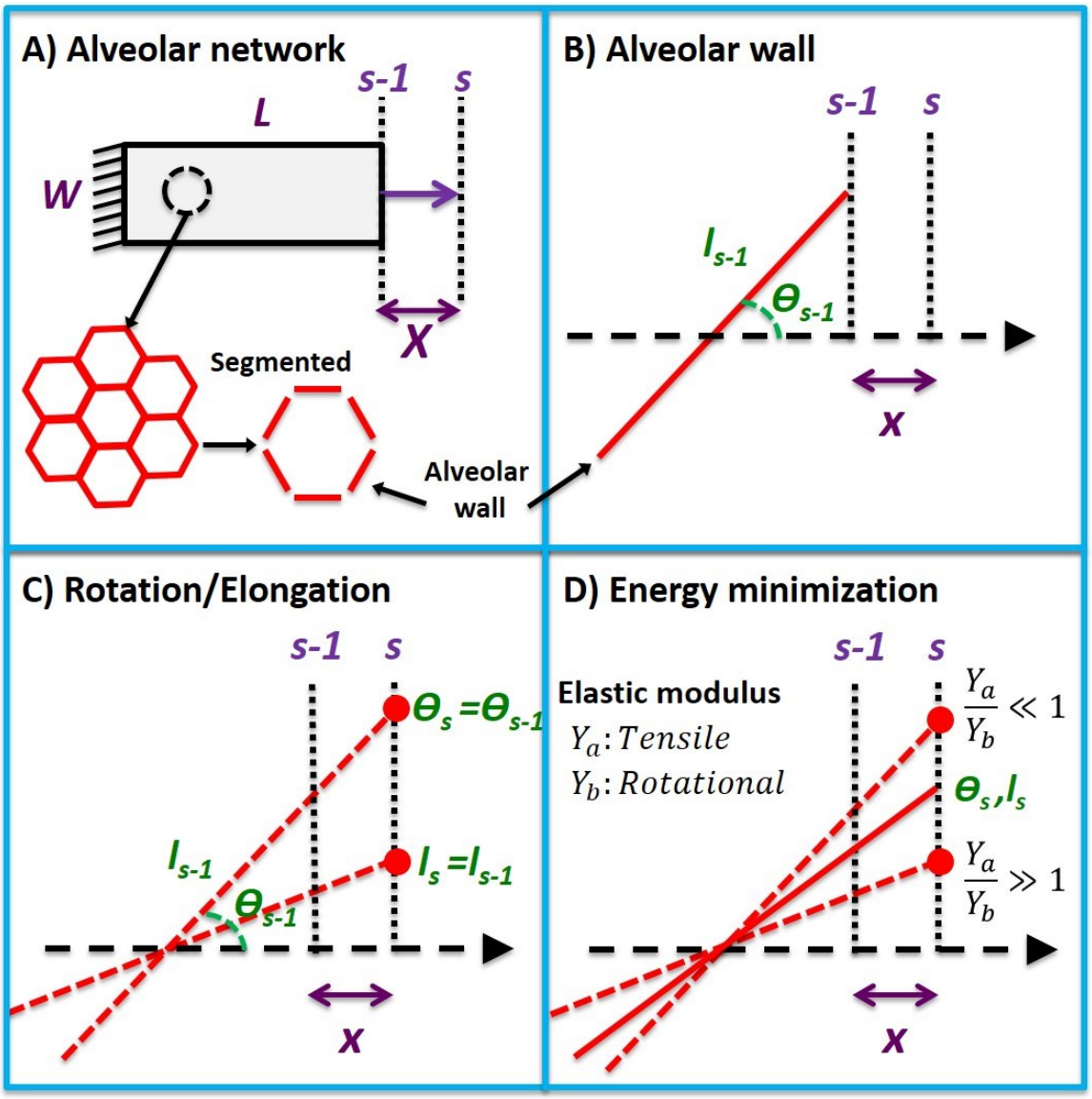

Figure 6-1: Uniaxial model development. A) Uniaxial stretching of a tissue strip from step *s-1* to *s* with an incremental macroscopic displacement *X*. The tissue is composed of a hexagonal alveolar network which can be partitioned into alveolar walls. B) A single alveolar wall segment with length l_{s-1} and angle Θ_{s-1} with respect to the direction of stretch at step s-1. A microscopic displacement *x* will cause the wall to rotate and stretch. C) The alveolar wall will follow the microscopic displacement between two extremes of pure elongation and pure rotation. D) When the tensile elastic modulus of the wall is much larger than its rotational elastic modulus ($Y_a >> Y_b$), it will rotate, and when its rotational elastic modulus is much larger than its tensile elastic modulus ($Y_b >> Y_a$), it will elongate in order to minimize energy. The new angle (Θ_s) and length (l_s) at step s will be between these two extreme locations at a location that minimizes its total elastic energy.

Due to a small incremental microscopic displacement *x,* the alveolar wall will stretch and rotate following the microscopic displacement between two extremes of either pure rotation and pure elongation (Figure 6-1C). The actual new configuration of the wall will be between these two limits such that the amount of rotation and elongation will minimize the total energy (Figure 6-1D).

Applying this approach to all walls at every single step/strain, the total system energy is the summation of energies for all alveolar walls as they undergo rotation and elongation. Finally, the total stress of the system is calculated by differentiating the energy density of the system with respect to macroscopic strain. To establish the final stress-strain equation, we assume the following:

- An average constant tensile and rotational elastic modulus.
- Affine tissue macroscopic-microscopic deformation characterized by the following: the incremental microscopic tissue strain (ε_{ix}) due to the incremental microscopic displacement *x* is equal to the incremental macroscopic strain (ε_{iX}) due to the macroscopic incremental displacement *X* ($\varepsilon_{iX} = \varepsilon_{ix}$).
- Linear relationship between incremental alveolar wall length and alveolar wall rotation between the two extreme points (pure elongation and pure rotation) with each incremental macroscopic strain.
- $L/W >> 1$ such that there are minimal boundary effects and any displacements in the direction perpendicular to stretch do not affect the alveolar wall behavior.

With the above assumptions, the final total tissue stress σ_T at every step s can be related to the alveolar wall properties, current microscopic alveolar strains and angles, initial

angles θ_i, and the incremental strain as described in detail in Appendix D.1:

$$\sigma_T(s) = Y_{ae}\frac{1}{N}\sum_{n=1}^{N}\frac{\varepsilon_{ix} + \ \varepsilon_{n,s-1} + \left(1+\varepsilon_{n,s-1}\right)\left(\theta_{n,i}-\theta_{n,s-1}\right)\tan(\theta_{n,s-1})}{1+\frac{Y_{ae}}{Y_{be}}\left(1+\varepsilon_{n,s-1}\right)^2\tan^2\left(\theta_{n,s-1}\right)} \quad (6.11)$$

Thus, the total stress involves an average across all alveolar walls from $n = 1$ to N which includes interaction terms between previous alveolar wall strains and angles. In case the alveolar walls are all aligned, the denominator is equal to 1, the last term of the numerator is 0, and the stress-strain equation reduces to linearly elastic walls in parallel

$$\sigma_T = Y_{ae}\varepsilon_T \quad (6.12)$$

where $\varepsilon_T \ = \varepsilon_{iT} + \ \bar{\varepsilon}_{s-1}$ is the total tissue macroscopic strain and $\bar{\varepsilon}_{s-1}$ is the mean alveolar strain. Therefore, regardless of the initial angle distribution, following full alignment, the linear portion of the stress-strain curve only depends on the tensile elastic modulus of the walls and their density. Furthermore, since the final tissue stress at each step is the mean over all the walls, it is independent of the alveolar wall number.

Invoking the assumption of a uniform distribution of alveolar wall angles, the final equation involves two elastic modulus parameters to estimate (Y_{ae} and Y_{be}).With an additional step, the average fiber tensile elastic modulus (Y_f) within the walls can be estimated by knowing the average fiber volume fraction ($\delta_{V,f}$) within the wall and assuming they are the major contributors to the alveolar wall tensile elastic modulus:

$$Y_f \cong \frac{Y_a}{\delta_{V,f}} \cong \frac{Y_{ae}}{\delta_{V,w}\delta_{V,f}} \quad (6.13)$$

6.2.2 Forward simulations

First, forward simulations were used to find the combination of the two elastic

modulus values which lead to an experimentally observed lung tissue stress-strain curve. For this purpose, effective tensile to rotational elastic modulus ratios (Y_{ae}/Y_{be}) ranging from 0.01 to 100 (order of magnitude steps) were utilized for a uniform angle distribution between 0 and $\pi/2$. Dimensionless stress-strain curves normalized by Y_{ae} were plotted for five different simulations. For ratios of 0.1, 1, and 10, the alveolar angles and strains are also computed at four different tissue strains of 0.25, 0.5, 0.75, and 1. For a ratio of 10, a sensitivity analysis was conducted to study the effect on tissue stress of independently changing Y_{ae} and Y_{be} by 10, 20, and 40%. Additional forward simulations, available in Appendix D.2, were carried out to examine the effects of alveolar number and incremental strain.

6.2.3 Model validation

6.2.3.1 Computational model validation

To compare our analytic results to a previously developed model, several stress-strain curves were generated from a previously developed hexagonal network model [128] and fitted using our model. Briefly, Cavalcante et al.'s [128] introduced a 2-dimensional hexagonal network as a model of lung tissue strip. Each hexagon represents an alveolus and each side of the hexagon is an alveolar wall (Figure D-3A, Appendix D.3). Each of these wall segments is modeled as a spring with a spring constant k in units of [N/m]. The rotation of the alveolar walls at their connected nodes is hindered elastically and a bond-bending constant b [N.m] is used to evaluate the energy required to rotate the alveolar wall. When b is zero, the hexagonal structure collapses upon shear or uniaxial stretch and when b is very high, the rotation of the wall is reduced so as to maintain the symmetric

configuration of the hexagon. In both cases, the walls rotate and stretch in such a way that the total energy is minimized at each strain step. However, Cavalcante et al.'s [128] model minimizes the total network energy which includes alveolar wall interactions while our model minimizes the energy of an average wall without network effects. In order to see how this difference affects our estimated parameters, we first relate our model to their network parameters. In doing so, we note the total energy at each tissue strain should be the same and thus by equating the network's energy equation of both models (see Appendix D.3 for details), we can relate Y_{ae} (Pa) to k and Y_{be} (Pa) to b as follows:

$$Y_{ae} = u\frac{9}{4}\bar{l}_i^2 k \tag{6.14}$$

$$Y_{be} = u18b \tag{6.15}$$

where $\bar{l}_i$ [m] is the mean initial length of the walls and u [$1/m^3$] is a unity constant to account for appropriate dimensions.

A set of 11 simulations (N=508, L/W=10.2) with varying k and b were generated using the network model, their initial angle distributions were saved and imported into our analytical model, and then the stress-strain curves were fitted using the exact angle distribution from the network. The estimated parameters and their theoretical values (Eqns. 6.14 and 6.15) were plotted against the network parameters. For an additional simulation (N=4762, L/W=10.1) the alveolar angles and alveolar strains at 4 different tissue strains (0.15, 0.3, 0.45, and 0.6) were compared by dividing the data into 9 different bins and plotting their probability distribution function.

6.2.3.2 Experimental validation

The physiological interpretation and consistency of Y_{ae} and Y_{be} was tested using stress-strain data previously collected for lung tissue strips undergoing two different treatments.

In one treatment, Cavalcante et al. [128] altered the charge density on the PGs using different tonicities (normal, hypertonic, and hypotonic) in excised rat lung slices (n=5 per group). They showed that lung tissue strips in hypotonic and hypertonic solutions were significantly stiffer and softer compared to normal tissue respectively. This was explained through the repulsive effect of the negative charges on PG's in the alveolar walls. In hypertonic solutions, the negative repulsive forces are more neutralized by the positive ion in the solution which results in reducing the compressive rotational stresses, while in hypotonic solutions this stress increases due to absence of neutralizing agents. Due to the significantly lower surfaces charges of elastin and collagen compared to PG [169,170] the hypotonic and hypertonic solutions should mainly alter Y_{be} increasing and decreasing it respectively with minor alterations in Y_{ae}.

In the other treatment, Shiwen et al. [171] studied the effect of Myocardin Related Transcription Factor-A (MRTF-A) on the development and progression of fibrosis. MRTF-A is known to lead to a reduction in type I collagen deposition leading to tissue softening. Using lung tissue strips from wild type (WT, n=6) and aged-matched MRTF-A knockout mice (KO, n=6), quasi-steady stress-strain curves were collected, and the study showed reduced stresses compared to WT. The reduction was attributed to a decrease in collagen content as well as a decrease in fibril diameter size from 97±24 nm (n=986) in WT to 58±9

nm (n=1086) in KO. In this case, collagen elimination by the knockout treatment should alter Y_f and Y_{ae} with minimal alterations to Y_{be}.

6.2.4 Aging study

After confirming that the model parameter estimation is credible, we investigated the effects of aging on alveolar wall tensile and rotational elastic modulus in mice by fitting previously collected lung tissue stress-strain curves obtained in young (n=5, 5 months) and old (n=6, 19 and 24 months) mice. The experimental protocol was approved by the Institutional Animal Care and Use Committee of Boston University. Tissue stress-strain curves were obtained as previously described [154,171]. Briefly, mice (C57BL/6) were anaesthetized with an intraperitoneal injection of Nembutal (80 mg/kg). Depth of anesthesia was confirmed by absence of response to toe pinch. Mice were then euthanized, the lungs were isolated, and the tissue strips were cut from the lungs and the dimensions were measured. These strips were then stretched using a servo-controlled lever arm (series 308B, Cambridge Technologies) driven by a laptop. From the other side of the tissue, a force transducer (model 400A, Cambridge Technologies) measured the force. Stress and strain were calculated from the measured force and displacement using the strip dimensions.

6.2.5 Simulations, curve fitting and statistical analysis

Data simulation and curve fitting were carried out using either MATLAB R2015a or R2018b (MathWorks, CA) while statistical tests were performed using SigmaPlot 11.0 (Systat Software, CA). To fit the data, the nlinfit function in MATLAB was used. Since

the model requires small incremental strains to satisfy the assumptions, while in some cases the experimental strain steps are large, the model first created strain values that ranged from zero to the maximum experimental strain utilizing small user-defined steps. At a tissue strain of zero, the alveolar strains were set to zero and the alveolar angles were defined by a user selected distribution. Using the initial parameter guesses, the new alveolar angles and strains due to the macroscopic incremental strain were calculated iteratively across the whole strain vector. The individual alveolar wall folding and stretching patterns were computed and the tissues stress was calculated. The error was calculated by utilizing the experimental stress and the interpolated model stress values at the experimental strains. To avoid solutions corresponding to local minima, multiple fitting iterations with random initial guesses were employed, and the fit with the lowest mean square-error was selected. In fitting the experimental data, the model's incremental strain was set to 0.001, the number of alveolar walls was 5000, and the alveolar angle distribution was uniform between 0 and $\pi/2$. The model is symmetric with the direction of stretch (i.e., an alveolar wall initially oriented at $-\pi/4$ and $\pi/4$ behave the same), and once a wall was recruited in the direction of macroscopic strain, it was allowed to stretch without any rotation. Statistical significance was accepted at $p<0.05$.

6.3 Results

6.3.1 Forward simulations

Figure 6-2 plots the normalized stress-strain curves for five different Y_{ae}/Y_{be} ratios (Figure 6-2A) as well as displays the mean and standard deviation for the alveolar angles and

strains for three of those ratios (Figure 6-2B and 6-2C, respectively). The forward simulation for the normalized stress strain curves reveals an almost linear relationship for Y_{ae}/Y_{be} ratios of 0.01, 0.1, and 1 suggesting that the micro-structural configuration is maintained by simple alveolar stretching (minimal rotation). This is supported by the change in angels which is minimal for a ratio of 0.1 (Figure 6-2B). With an increasing elastic modulus ratio, the curves gradually become more similar to the observed convex stress-strain curves and the stress is less for the same strain since alveolar walls can reduce total energy as well as stress by rotating. The higher the ratio, the lower the stress becomes; however, the recruitment becomes faster as evident by the alveolar angles (Figure 6-2B). Beyond an elastic modulus ratio of 100, the ratio has less of an effect indicating that the walls are mainly rotating and not stretching.

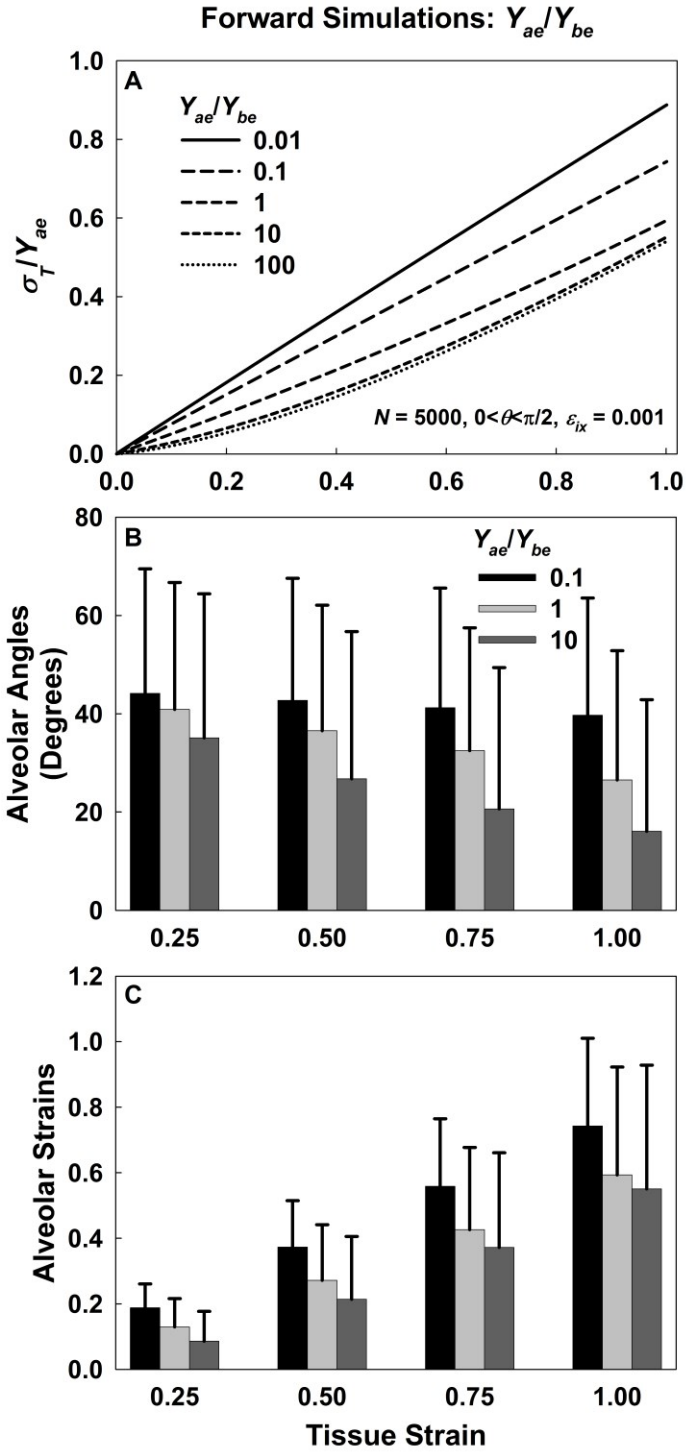

Figure 6-2: Forward simulation results. A) Normalized stress-strain curves for different Y_{ae}/Y_{be} ratios. B) and C) Mean and standard deviation for alveolar angles and strains, respectively for Y_{ae}/Y_{be} ratios of 0.1,1, and 10. Alveolar angles at a strain of zero are uniformly distributed between 0 and π/2 while alveolar strains are zero.

Figure 6-3 represents the percent change in stress due to individually varying Y_{ae} or Y_{be} around an elastic modulus ratio of 10 versus tissue strain. From the figure, it is evident that the contributions of Y_{ae} and Y_{be} have opposite effects. The former has a stronger impact at higher strains, while the latter's dominance is more apparent at lower strains. Once the alveolar walls are aligned, Y_{be} has no further effect on the stress-strain curve and only then is the percent change in stress equal to the percent change in Y_{ae} (otherwise it is always less); however, a linear effect from Y_{be} is not possible. This analysis provides a range of strains over which data should be collected in order to determine meaningful parameters. For instance, fitting the stress-strain curve over a range of strains from 0 to 30% should be sufficient to reliably estimate both elastic modulus values.

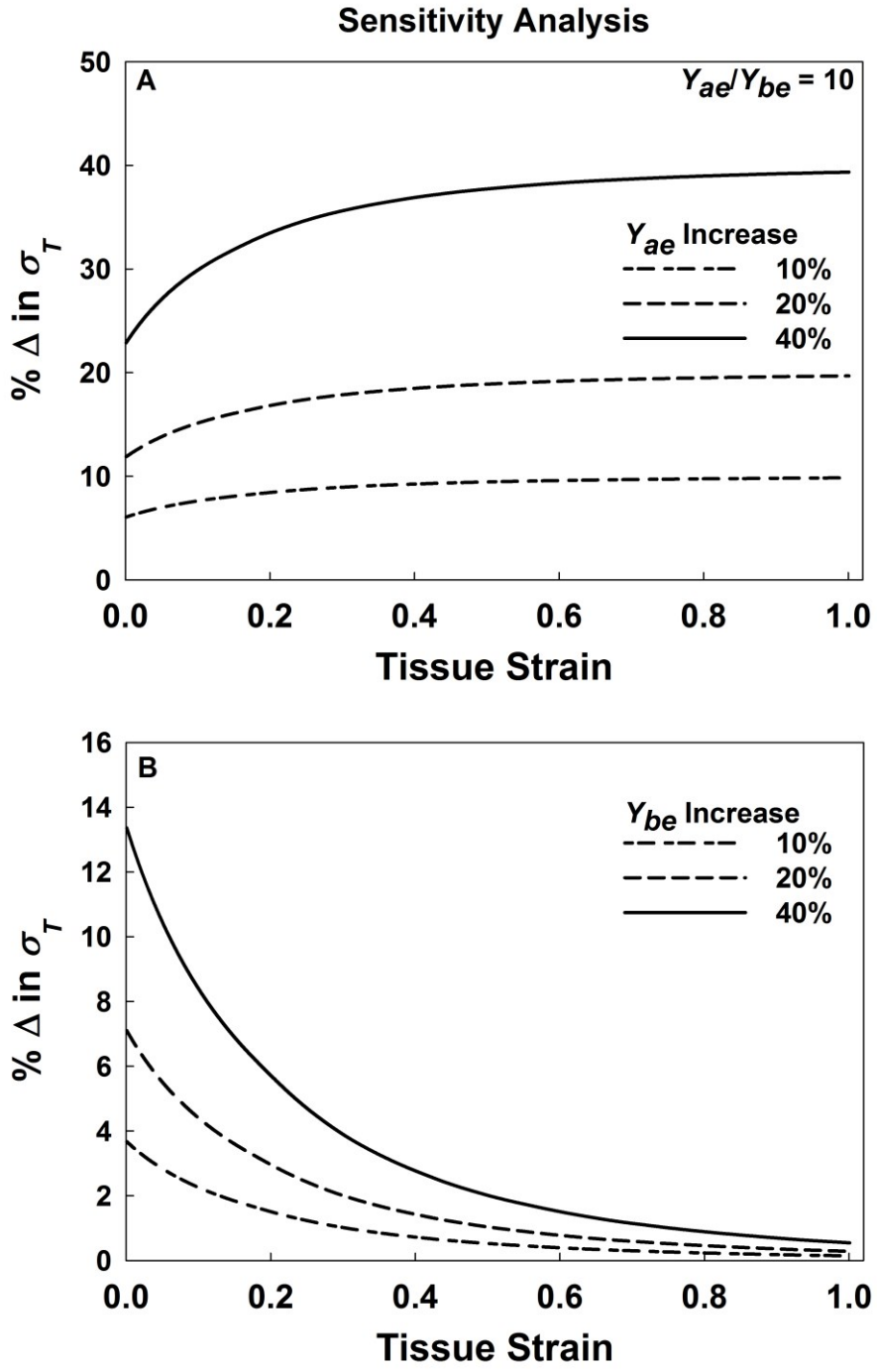

Figure 6-3: Sensitivity analysis. A) and B) % change in stress for increasing Y_{ae} and Y_{be} respectively by 10, 20, and 40% for Y_{ae}/Y_{be} of 10.

6.3.2 Model validation

6.3.2.1 Computational Model Validation

Comparisons of analytical model-based estimates of Y_{ae} and Y_{be} values to those of the used in the network simulations for a range of parameter values are shown in Figure 6-4. The estimated model parameters were independent of each other and were consistent with the theoretical values. In addition to adding credibly to the model, this provides an ability to estimate time-consuming numerical network simulations with a much faster analytical one.

Alveolar angles and strains probability distributions for the selected network at four different tissue strains are shown in Figure 6-5. The angle distributions from the analytical match well those from the network. In the analytical model, the alveolar walls are recruited faster since in the network the interactions among the nodes slow down the recruitment of the walls. The strain distribution histograms, though not as consistent as the angles, also show similar behavior and most importantly similar strain range values. However, in the network two nodes which form an alveolar wall can approach each other causing the length of the alveolar wall to decreases unlike the model where the length only increases. Note however that the network model does not consider this effect in the energy calculation. In other words, any “compressed wall” is similar to a wavy fiber that does not contribute to stress.

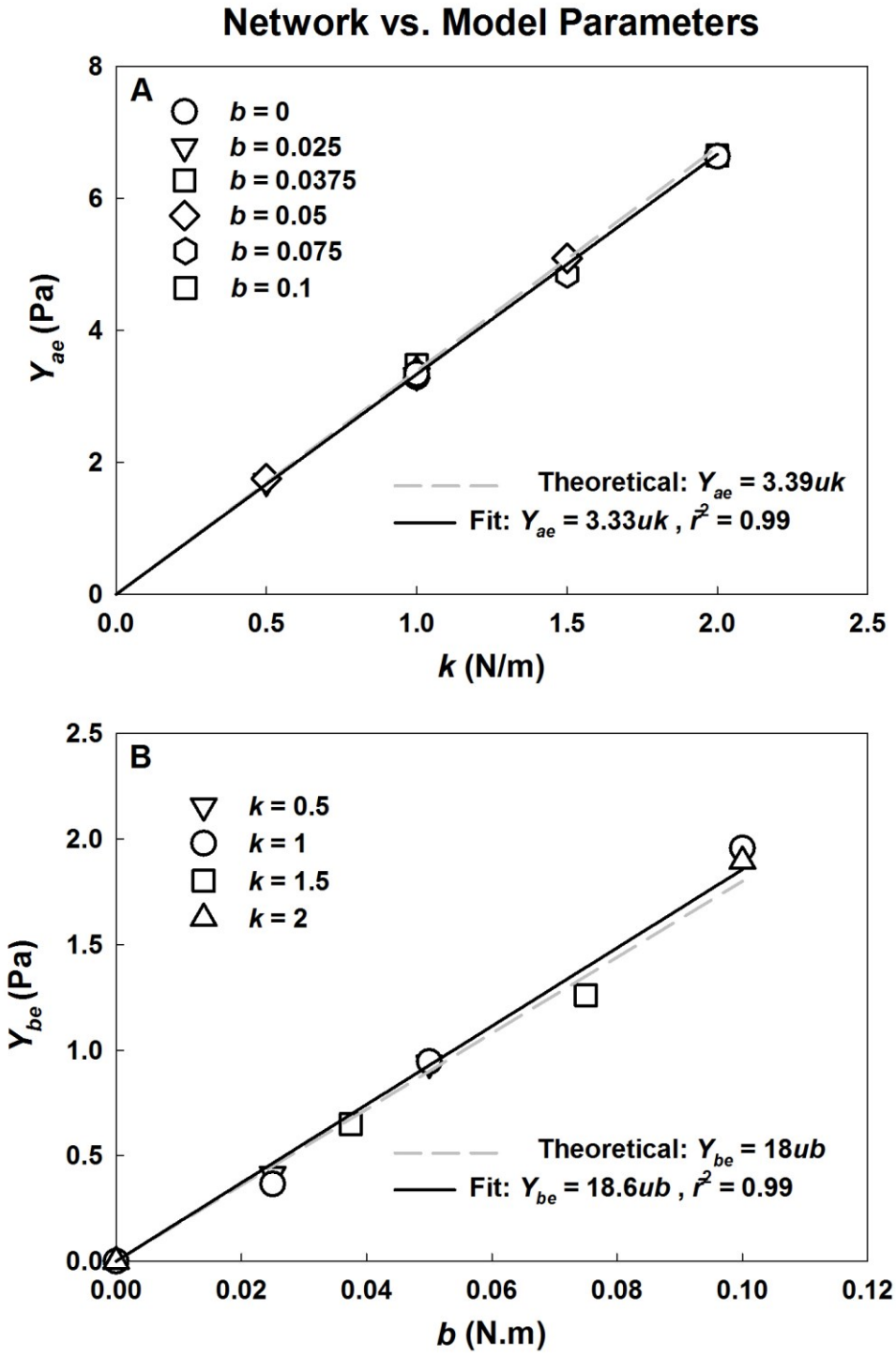

Figure 6-4: Uniaxial model-based estimates of network parameters. A) Y_{ae} versus k for different b values. B) Y_{be} versus b for different k values. Dashed gray lines represent the theoretical relationship between network and model parameters. Solid lines represent the fits with the $\bar{r}^2$ as the adjusted coefficient of determination for the linear fit.

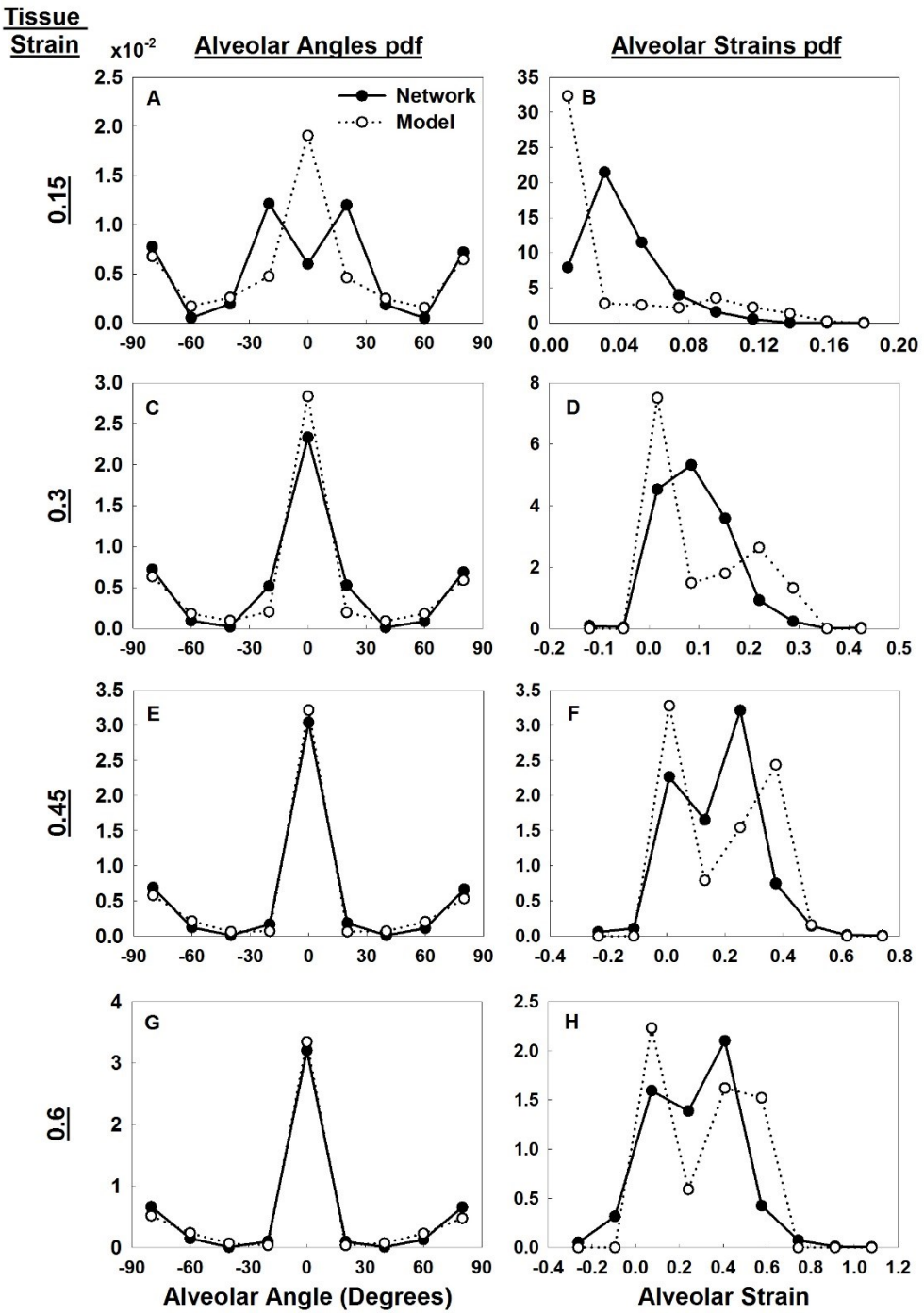

Figure 6-5: Uniaxial and the network model alveolar strains and angles. Alveolar angle probability distribution function (A, C, E, and G) and alveolar strains probability distribution function (B, D, F, and H) from the analytical model and the network for four levels of tissue strains (0.15, 0.3, 0.45, and 0.6). Initial alveolar strains are zero. Initial angle distribution is shown in Appendix D.3 Figure D-3B.

6.3.2.2 Experimental Validation

In Figure 6-6, model fits for the rat tissue strips (Figure 6-6A) under different tonicity conditions and between WT and MRTF-A KO mice (Figure 6-6B) are shown. The results are shown in Table 6-1. For the alterations in tonicity, there was no statistically-significant change in Y_{ae} comparing hypertonic and hypotonic values to normal. However, Y_{be} increased by 211% from normal to hypotonic solution (p=0.03). Even though, for the hypertonic solution, there was no significant change (p=0.09), Y_{be} decreased by -60%, around 9 times more than the decrease in Y_{ae}. On the other hand, for the MRTF-A KO experiments, Y_{ae} decrease significantly (p=0.014) while there was no significant change in Y_{be}. Thus, the model predicted the expected changes which occur with the two different treatments of opposing outcomes. This further provides credibility to applying the model to fit experimental data.

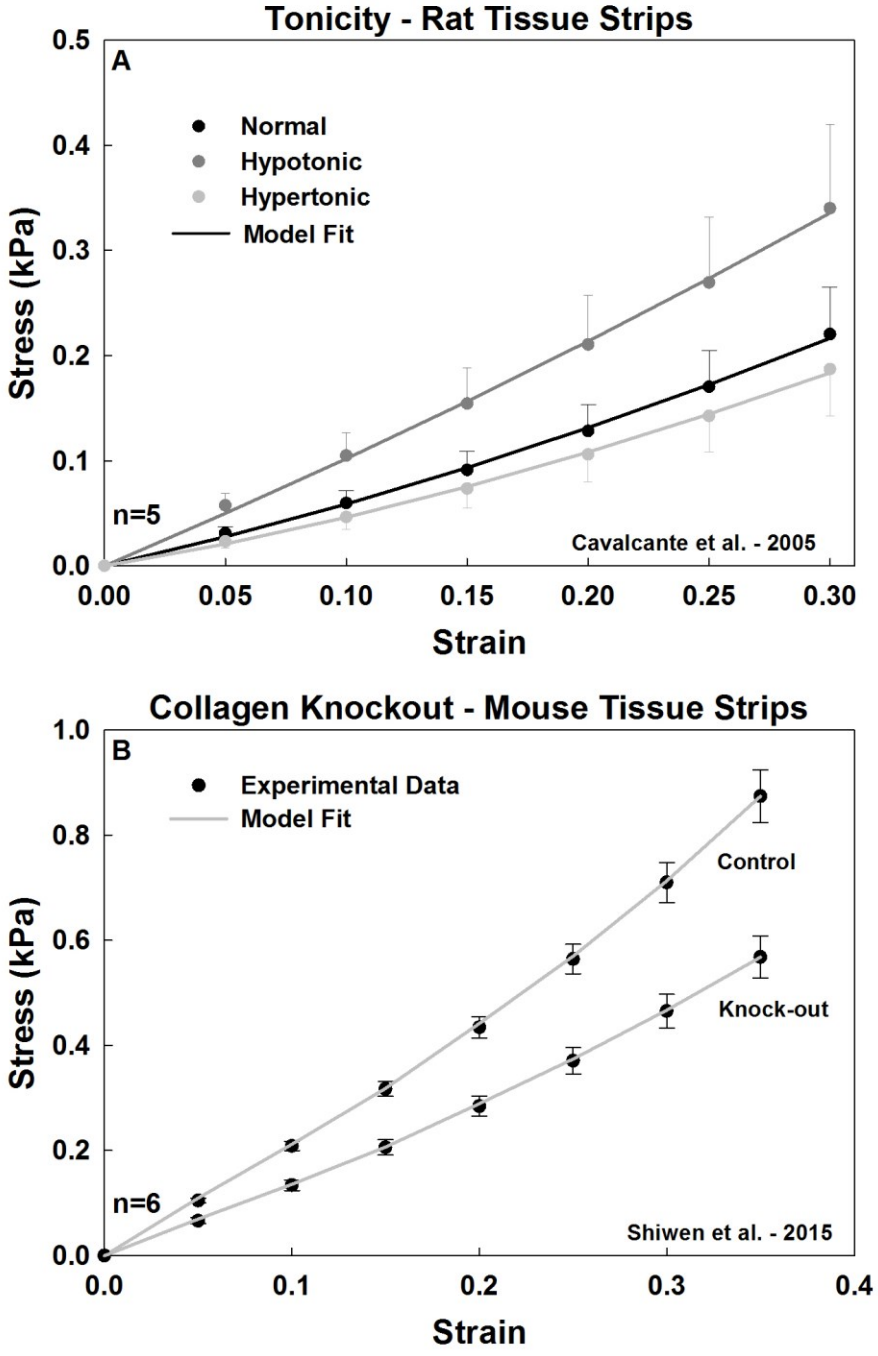

Figure 6-6: Experimental validation. Population mean and standard error, with model fits (solid lines) for the tissue strips for A) three different tonicities (normal, hypertonic, and hypotonic) and B) from WT and MRTF-A KO mice.

Table 6-1: Model validation experimental results. Y_{ae} and Y_{be} values are mean ± standard deviation. Δ is the percent difference with respect to the normal/control.

Tonicity - Rat Tissue Strips						
	Y_{ae} (kPa)	**%Δ**	**p-value**	**Y_{be} (kPa)**	**%Δ**	**p-value**
Normal	1.94 ± 1.07			0.27 ± 0.14		
Hypotonic	3.28 ± 1.75	69	0.11	0.84 ± 0.41	211	0.03
Hypertonic	1.78 ± 1.03	-8	0.11	0.11 ± 0.11	-60	0.09
Collagen Knockout - Mouse Tissue Strips						
	Y_{ae} (kPa)	**%Δ**	**p-value**	**Y_{be} (kPa)**	**%Δ**	**p-value**
Control	5.96 ± 1.39			1.28 ± 0.42		
Knock-out	3.94 ± 0.93	-34	0.014	0.84 ± 0.58	-34	0.165

6.3.3 Aging study

The mean of the tissue strip stress-strain curves from young and old mouse lungs as well as the model fits are shown in Figure 6-7. The estimated Y_{ae} and Y_{be} with the respective p-values are also shown in the inset. The average Y_a and Y_b as well as the fiber tensile elastic modulus (Y_f) were also estimated using literature values of tissue ($\delta_{V,w}$) and fiber density ($\delta_{V,f}$). Huang et al. [172] measured tissue density as well as fiber content for 2 and 20 months old C57BL/6 mice. The tissue fraction was 35% independent of age, while the total fiber content (collagen plus elastin) decreased with age from 4 to 2.75%. There was no significant change in Y_{be}. However, Y_{ae} increased from 4.4 to 5.9 kPa (p=0.043), a 34.4% increase. More interestingly, Y_f increased by 99.4% from 311 to 620 kPa from young to old mice (p=0.001).

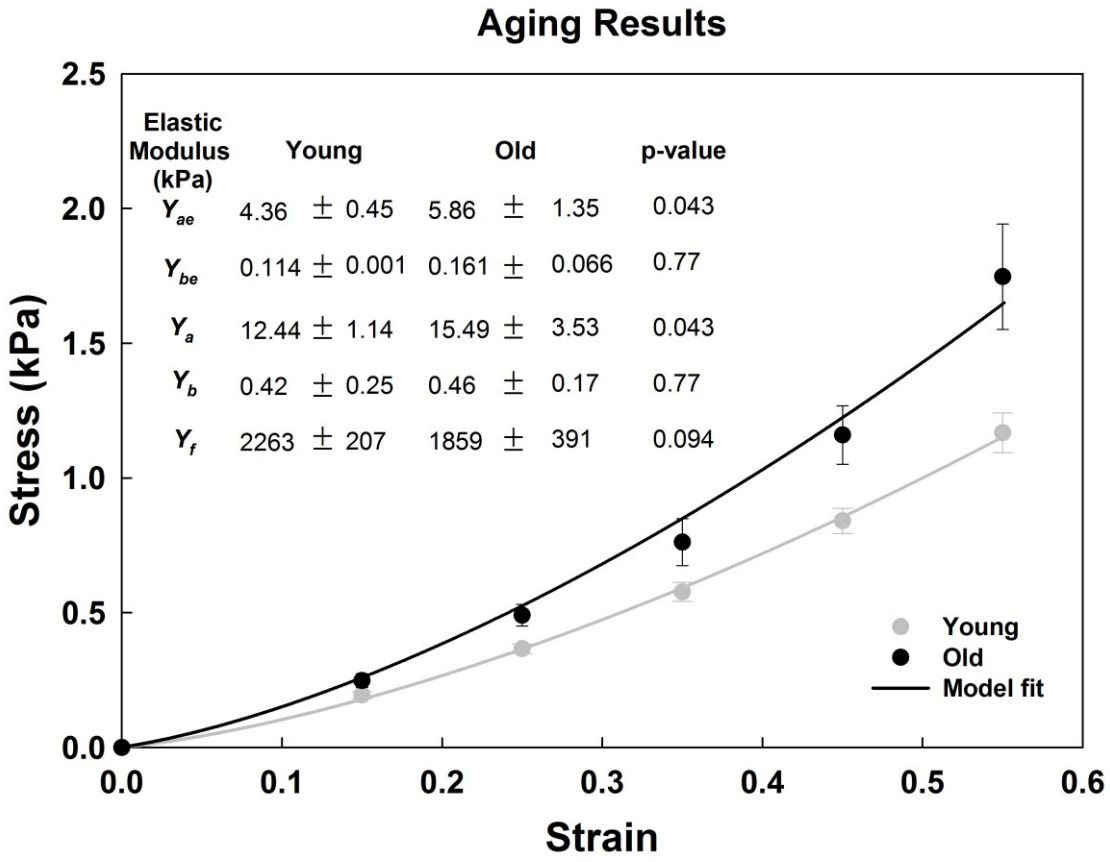

Figure 6-7: Stress-strain curves and parameter estimation results for the aging data. Experimental data mean and standard errors for young and old mice. Model fits are plotted in solid lines. Model fitted for Y_{ae} and Y_{be} which were used to derive Y_a, Y_b, and Y_f. Their value, standard deviation, and significance are shown. Y_a: average alveolar tensile elastic modulus. Y_b; average alveolar wall rotational elastic modulus. Y_f: average fiber tensile elastic modulus.

6.4 Discussion

The objective of the current study was to develop an analytical model of alveolar recruitment for uniaxially stretched lung tissue strips in order to estimate microscopic properties from macroscopic experimental stress-strain curves. We presented a mathematical model that can capture this behavior, demonstrated its ability to replicate physiologically observed experimental data, compared it to a numerical network model, and replicated expected model parameter changes with treatments of known outcomes. These steps of model validation showed that our analytical model could be used to fit experimental data to extract meaningful estimates of microscopic entities. Thus, our analytical model complements existing models in literature by providing separate estimates of alveolar wall tensional and rotational elastic modulus values together with alveolar stresses and strains.

The forward simulations indicated that the physiological ratio of tensile to rotational elastic modulus must exceed 1 in order to be able to replicate the experimentally observed convex nature of lung tissue stress-strain curve. The nonlinearity increases with higher ratios. This is consistent with the biological notion that the alveolar walls and the embedded fibers are the main load bearing elements in the lung parenchyma. Furthermore, the primary physiological role of the alveolar walls and fibers is to provide a structural framework for gas exchange while also protect the alveoli from over distension as they are stretching rather than rotating. Since the model attributes constant elastic modulus values during stretch, the nonlinearity of the stress strain curves in our model arises purely from the alveolar wall rotation, stretching, and alignment with the macroscopic strain.

For the additional forward simulations studying the effect of alveolar wall number and incremental strain (Appendix D.2), the key findings suggest that the model requires around 2000 alveolar walls and an incremental strain less than 0.01 to converge.

The basic assumption of our analytical model is that it is possible to partition the alveolar wall network into non-interacting segments. When the individual wall energies were minimized, the model provided estimates of elastic modulus values. Interestingly, these estimates compared well to the parameters used in the network model resulting in proper estimation of the network's parameters (Figure 6-4) as well as similar behavior in alveolar angles and strains (Figure 6-5). The slight discrepancy between the network and the analytical model predictions is likely due to network interactions affecting angles and strains in the network model. It is also important to mention that the model is sensitive to the assumed initial angle distribution. Indeed, attempting to fit the network simulations with any random distribution yielded very poor fits. This increases the specificity of the model and hence increases the accuracy of the estimated parameters.

A major assumption in the model is the linear stress-strain behavior of the alveolar wall with constant tensile elastic modulus. In particular, the model does not incorporate fiber waviness within the alveolar walls separating non-wavy elastin from wavy collagen fibers [173]. Since the elastin fibers are not wavy they should not presumably alter the alveolar stiffness with stretch. However, the straightening of wavy collagen fibers would increase the alveolar tensile stiffness with increasing alveolar and tissue strain. Future work can include an alveolar tensile stiffness as a function of alveolar strain to capture fiber waviness. This will lead to a higher degree polynomial in the energy equation. However,

the equation will still be a function of one parameter, the alveolar strain, and can be solved analytically. This can further provide insight into fiber properties by allowing the separation of non-wavy elastin fibers and wavy collagen fibers. It is worth noting that attempting to fit our model to data generated by a network of nonlinear springs yielded poor fits since the model assumes linear tensile elastic modulus. However, the model's ability to fit experimental data well within the tissue strain range suggests that the degree of nonlinearity in the alveolar wall stress-strain properties is not strong at least at low strains and hence our assumption of an average elastic modulus is fairly appropriate. Regardless of the assumption of average linear behavior, the parameters could still be physically interpreted; however, it should be noted that the estimates are thus an ensemble averaging of all these effects into two separated lumped elastic modulus parameters (tensile and rotational) which can be directly linked to an average behavior of tissue microscopic properties.

Another major assumption involves affine kinematics where the microscopic strains follow the macrostrains. While we require that the tissue microstrains follow tissue macrostrains, the individual wall segments do not have to follow the macrostrains. This is in agreement with experimental findings that alveolar segments violate the affine deformation assumption during uniaxial stretching [174]. Similarly, the network model does not assume affine transformations and the analytical model was able to estimate properly the parameters. Nevertheless, future work should further investigate experimentally how network effects influence the parameter estimation.

The estimated alveolar and fiber elastic modulus in aged mice indicated that even

though the fiber content decreases in aging C57BL/6 mice, the fibers actually become stiffer. This can be attributed to increased cross-linking with age [151,175]. This insight from the model fitting is important in that it suggests that despite the fact the overall lung compliance increases and hence lung elastance decreases in aging [153,176], both alveolar wall and fiber elastic modulus increase. This then suggests that the increase in lung compliance must be due to an observed increase in airspace dimensions [177]. More importantly however, this finding also suggests that in the aging lung cells will experience a gradually stiffening ECM which will have implications to cellular signaling and senescence [153].

Our estimated values of Y_{ae} and Y_f match those reported in literature. For example, Polio et al. [178], measured Y_{ae} using cavitation rheology (6.1±1.6 kPa), small amplitude oscillatory shear rheometry (3.3±0.5), micro-indentation (1.4±0.4), and uniaxial tension (3.4±0.4) and showed that all these techniques provided values in the same range. Using Atomic Force Microscopy, Liu and Tschumperlin [179] also estimated a value around 5 kPa. Using their network model, Cavalcante et al. [128] also estimated the effective alveolar wall stiffness to be ~5 kPa. Assuming that collagen fibers are the primary load bearing constituents of the wall, they also estimated fiber tensile elastic modulus to be ~300 kPa similar to our estimated average modulus in the mice even though ours is an ensemble value including elastin and collagen fibers. Furthermore, the elastic modulus of single elastin fibers has been evaluated to be around 410 kPa [180] which is close to our estimated Y_f values in mice. The fact that the estimated value is closer to that of elastin rather than collagen can be attributed to the delayed recruitment of wavy collagen fibers in comparison

to elastin which is thought to contribute mostly at low strains [181].

6.5 Conclusion

The analytical model developed in this study has the potential to estimate microscopic entities from macroscopic experimental measurements which can allow better understanding of the microscale changes which occur with age and disease. The model's estimation of alveolar tensile and rotational elastic modulus as well as alveolar stresses and strains are critical for mechanotransduction and can play a role in optimizing stresses during mechanical ventilation in order to avoid ventilation induced lung injury.

6.6 Acknowledgement

This study was supported by NIH grant U01 HL-139466. We are grateful to Ayuko Takahashi for collecting the mouse data used in the aging study.

Chapter 7: Conclusion

7.1 Summary of achievements

Linking accurate and clinically-feasible assessment of respiratory mechanics to microscopic information in order to provide personalized treatment of mechanically ventilated patients is far from being realized. Towards achieving this end, the presented work demonstrated the clinical feasibility of a novel strategy termed ZVV in its dual role as both a diagnostic and therapeutic tool for clinicians. We also provided the means to develop a flow sensor in order to properly obtain the required pressure-flow data and apply ZVV in a research-based setting. This makes ZVV an accessible technique to researchers interested in measuring respiratory mechanics and investigating the role of different ventilation strategies. On the other end of the scale, the study investigated how such macroscopic properties could emerge from microscopic entities at both the tissue and alveolar levels. Specifically, by proper modeling the individual constituents, mainly the fibers or alveolar walls, through their material properties and structural configuration, emergent physiological phenomena could be explained by micro-mechanics. For example, this allowed the quantitative assessment of alveolar and fiber stiffness and collagen organization in accordance to their roles. The general findings support our qualitative understanding of these roles as well as present non-classical insights which should be considered in future work such as the ability of linearly elastic collagen fibers to achieve inflation stability or their contribution at normal breathing pressures. Furthermore, linking the stresses and strains across different scales will improve the ability of cell and tissue level experiments to recreate correct physiology. Finally, while the two developed models

capture different mechanics between alignment of alveolar walls and recruitment of collagen fibers, they both demonstrated similar findings in aging. Thus, while some model predictions might be experimentally harder to validate such as the inflation of a single alveolus, other higher-level models could help extract data, verify, or provide experimental insight for smaller scale models. By constructing physiologically based and interlinked models through hierarchical levels, ultimately the macroscopic measurements can best capture microscopic mechanics and help explain emerging phenomena as well as reduce VILI.

7.2 Future directions

Future work should focus on further developing the presented and other methods on both the macroscopic and microscopic fronts under the overall objective of building a representative multiscale model. Due to their different nature, each scale presents a different type of challenge.

The analytical models presented in this work could be further enhanced to better represent microscopic mechanics. For the alveolar model, we propose the following:

1. **Surface tension**: Adding surface tension will allow the model to capture the two types of stabilities at both the inflation and deflation parts. To accomplish this new or already available models could be incorporated. This addition will not change the presented mathematical derivation but will only add an additional variable, surface tension (γ), in calculating the final pressure in Eq. 5.12. We hypothesize that this addition does not affect our findings concerning alveolar inflation stability but executing the investigation will provide the correct insight.

2. **Alveolar network and heterogeneity**: In reality the alveoli are interconnected and their mechanics are interdependent. In order to model this behavior, numerical simulations might be a better or even the only possible approach. While analytical solutions would be difficult to achieve in a network and not to mention across scales, they can still serve as inputs to single units as well as offer computational speed. On the other hand, it might actually be possible to use the derived analytical equations in a smaller network of alveoli such as an acinus. By assuming these units are all at same pressure but each is given a different fiber elastic modulus, we can compute the P-V curve for each alveolus and the difference in volumes at a prescribed pressure. This would also require solving the problem that several alveoli share septal walls and the alveoli must be space filling. Could the fact that the inextensible collagen fibers prevent the softer ones from over distension as the stiffer ones catch up in size? And if so under what conditions? Several questions on the small network scale concerning heterogeneity could be answered analytically. In addition, this will allow to study the effect of heterogeneous diseases on a small network scale.

Concerning the uniaxial model, we propose the following future work:

1. **Non-affine deformations**: Even though the alveolar wall has the ability to stretch and rotate, its ends still follow the microscopic tissue displacement which is modeled to behave in an affine fashion. Adding an energy expenditure term proportional to the square difference between the macroscopic and microscopic strain (similar to shear) will allow the wall to follow only a percentage of the macroscopic tissue strain and particularly the one that minimizes energy. Thus, this will lead to an additional stiffness

term in the energy equation. This term can represent the shear modulus and could be fitted with the other parameters as well.

2. **Wavy fibers embedded in alveolar walls**: As briefly discussed in chapter 6, we can model the alveolar stiffness, which is assumed to be constant, to be a function of fiber waviness by applying the equation derived for wavy fibers under uniaxial stretch presented in Appendix C.2. By deriving Eqs. C.76 and C.77 as a function of λ, we can obtain the incremental stiffness of the alveolar walls during and after full recruitment of the collagen fibers. Plugging that equation into the alveolar wall stiffness, it might be possible to further extract microscopic data (such as waviness) as well as separate elastin and collagen fibers at the level of the tissue.

ZVV's main challenge is to transition to clinical application. This would require further evidence on its potential as both a diagnostic and therapeutic tool. To this end, we propose these primary steps:

1. **ZVV vs. CV and degree of variability**: Even though ZVV requires variation in frequency and tidal volume to assess respiratory mechanics it can still be compared to CV by assuming that small variations in VV tidal volumes is closest to CV. In fact, different levels of tidal volume variability should be tested to determine its effect on the assessed parameters. Of course, CV and VV can always be compared on other basis (i.e. blood gas, inflammation…). However, comparison of respiratory mechanics using ZVV serves as new and direct assessment.
2. **Comprehensive respiratory assessment via ZVV**: By applying different positive-end expiratory pressures, tidal volumes, and breathing rates within physiological limits,

ZVV can assess respiratory resistance and elastance as a function of combined ventilation settings.

3. **ZVV feedback control**: A ventilator should be designed to construct Z_{RS} using ZVV and then determine, using these values, an optimal new combination of settings. This will present ZVV as an objective approach to determine ventilator settings on a personalized basis.

Point (1), being very similar to the human clinical trial presented, can be already integrated into a clinical trial. If the latter demonstrates the advantage of VV over CV, then this can lead to significant implications on current respiratory healthcare. Combining points (2) and (3) simultaneously, ZVV then will assess respiratory mechanics across different settings and select those which optimize a given objective function (i.e. compliance). This can be carried out automatically by the ventilator at specific time intervals. Furthermore, by integrating the multiscale models, the selection of ventilator parameters could be further enhanced based on microscopic estimates such as optimizing fiber stresses and reducing VILI leading to a technique that might be called the Smart Variable Ventilation, or SVV (Figure 7-1). Unlike point (1), these two points would require experimental support before clinical feasibility studies.

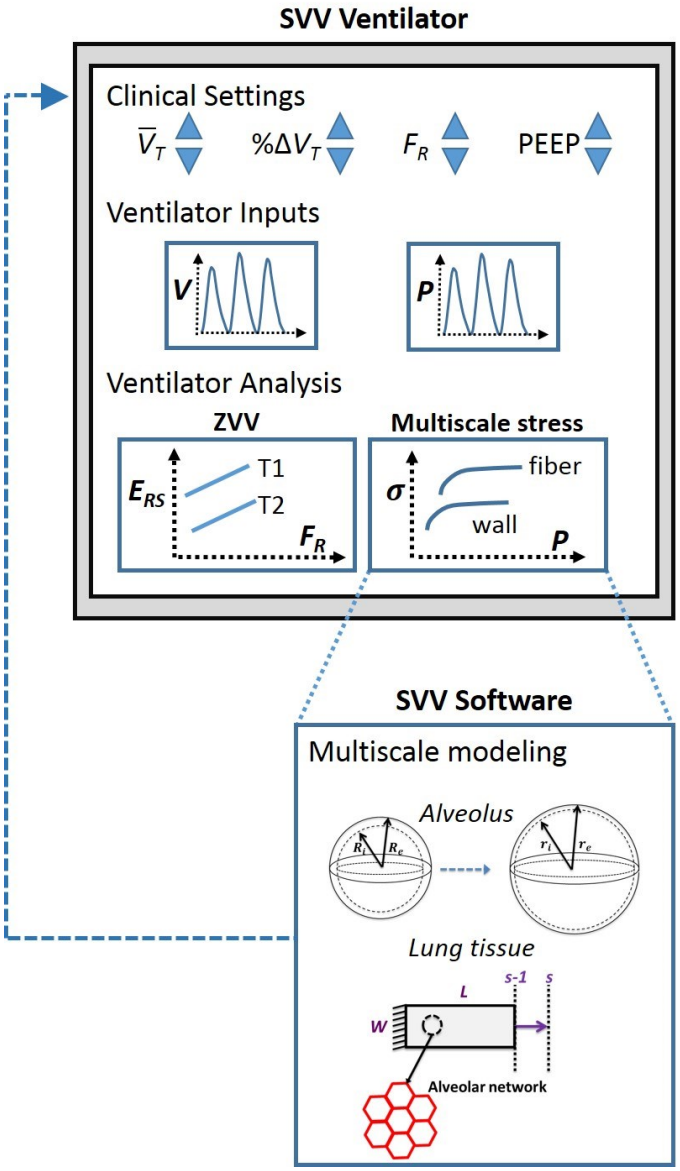

Figure 7-1: Future directions: Smart Variable Ventilation (SVV). First, the clinician selects the clinical settings such as mean tidal volume ($\overline{V}_T$), percent variation in tidal volume (%ΔV_T), respiratory frequency (F_R), and positive-end expiratory pressure (PEEP). Then the ventilator will deliver variable ventilation (VV) and the built-in software will continuously assess respiratory mechanics (i.e. respiratory elastance E_{RS}) across time (i.e. T1 and T2) from continuous volume (V) and pressure (P) recordings. The software would then be able to estimate microscopic alveolar and fiber stresses through research-based findings and integrated multiscale models. From these estimates, the software can provide automatic feedback control for the optimal clinical settings (i.e. settings which minimize E_{RS} and fiber stresses) in order to avoid or reduce ventilation-induced lung injury across time periods. The SVV approach would automatically track and adjust to the potentially time varying conditions of the patient providing the best adaptive ventilation possible.

Appendix A: Flow Sensor

Table A-1: Measured volumes and flow resistance for sensor parts.

Sensor Part	Length (mm)	Smaller Inner Radius (mm)	Larger Inner Radius (mm)	Volume (mm^3) (truncated cone)	Flow Resistance ($cmH_2O.s/ml$)
Inner Core	5.8	0.25	0.25	3.42	2.2937
Ventilator & Cannula Connection	3.5	1	1	11.00	0.0018
Between Inlet/Outlet and Inner core Section 1: Pressure drop measured	3.85	0.25	0.855	8.12	0.1363
Between Inlet/Outlet and Inner core Section 2: Pressure drop not measured	0.75	0.855	1	4.06	0.0011

Table A-2: Alternative flow sensor design.

Sensor Part	Length (mm)	Smaller Inner Radius (mm)	Larger Inner Radius (mm)	Volume (mm^3) (truncated cone)	Flow Resistance ($cmH_2O.s/ml$)
Inner Core	5.8	0.55	0.55	5.51	0.0326
Ventilator & Cannula Connection	3.5	1	1	21.99	0.0036
Between Inlet/Outlet and Inner core Section 1: Pressure drop measured	3.850	0.55	0.927	13.47	0.0167
Between Inlet/Outlet and Inner core Section 2: Pressure drop not measured	0.75	0.927	1	4.38	0.0009

Table A-3: Alternative flow sensor design characteristics.

Sensor Resistance ($cmH_2O.s/ml$)	0.0538
Sensor Dead Space (ml)	0.0454
% Dead space from Tidal Volume (0.2ml)	22.68
% of Mouse Resistance (0.5 $cmH_2O.s/ml$)	10.76
% of Mouse Resistance (0.8 $cmH_2O.s/ml$)	6.73
% Resistance across measured pressure drop	91.6
Inclination Angle (degrees)	5.6

Table A-4: Kernel values. 2nd and 3rd order kernel values.

h_2						
Index	**1**	**2**	**3**	**4**	**5**	**6**
1	-1.28	2.07	0.31	-1.60	0.03	0.50
2	2.07	-3.31	-1.88	4.89	-1.01	-0.95
3	0.31	-1.88	4.32	-2.50	-2.02	2.01
4	-1.60	4.89	-2.50	-6.74	10.28	-4.44
5	0.03	-1.01	-2.02	10.28	-11.95	4.68
6	0.50	-0.95	2.01	-4.44	4.68	-1.81
$h_3(i_1,i_2,6)$						
Index	**1**	**2**	**3**	**4**	**5**	**6**
1	6.33	-15.02	6.63	21.24	-28.84	5.34
2	-15.02	29.62	8.63	-98.91	115.69	-20.98
3	6.63	8.63	-111.74	252.70	-236.02	39.37
4	21.24	-98.91	252.70	-372.90	293.49	-46.42
5	-28.84	115.69	-236.02	293.49	-209.69	32.69
6	5.34	-20.98	39.37	-46.42	32.69	-7.01

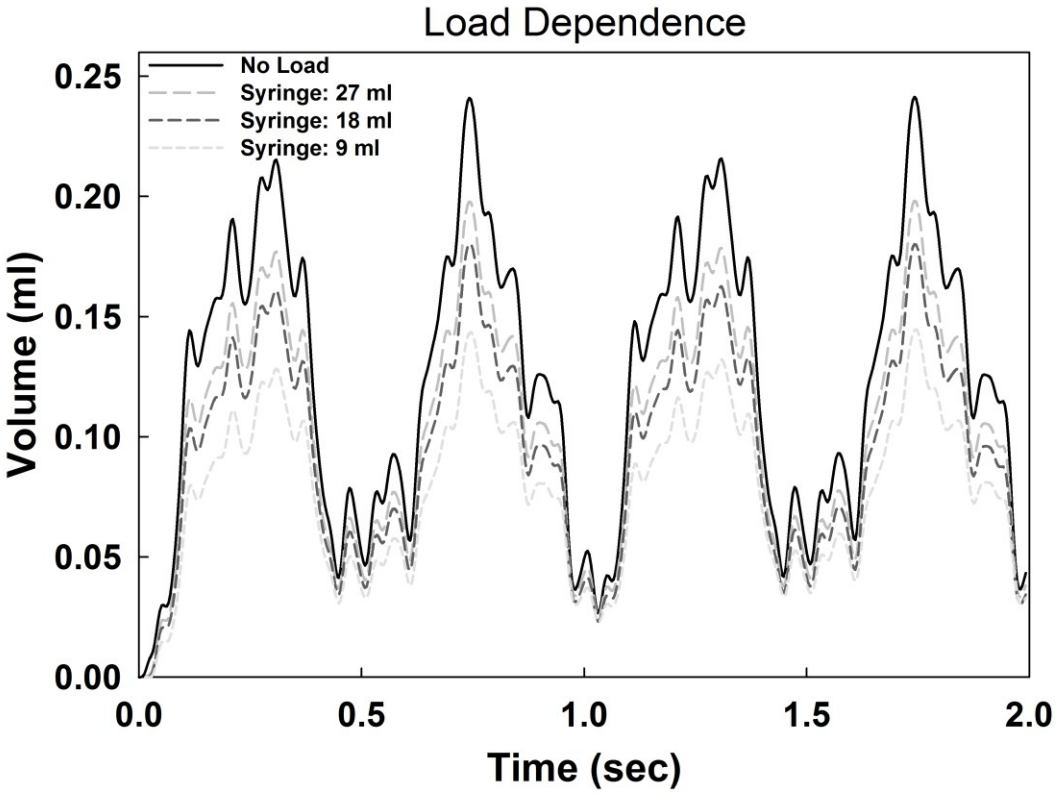

Figure A-1: Ventilation delivered volume load dependence. Using the composite volume perturbation signal with four different load conditions (no load, 9, 18, and 27 ml syringe volume) the delivered tidal volume showed load dependence.

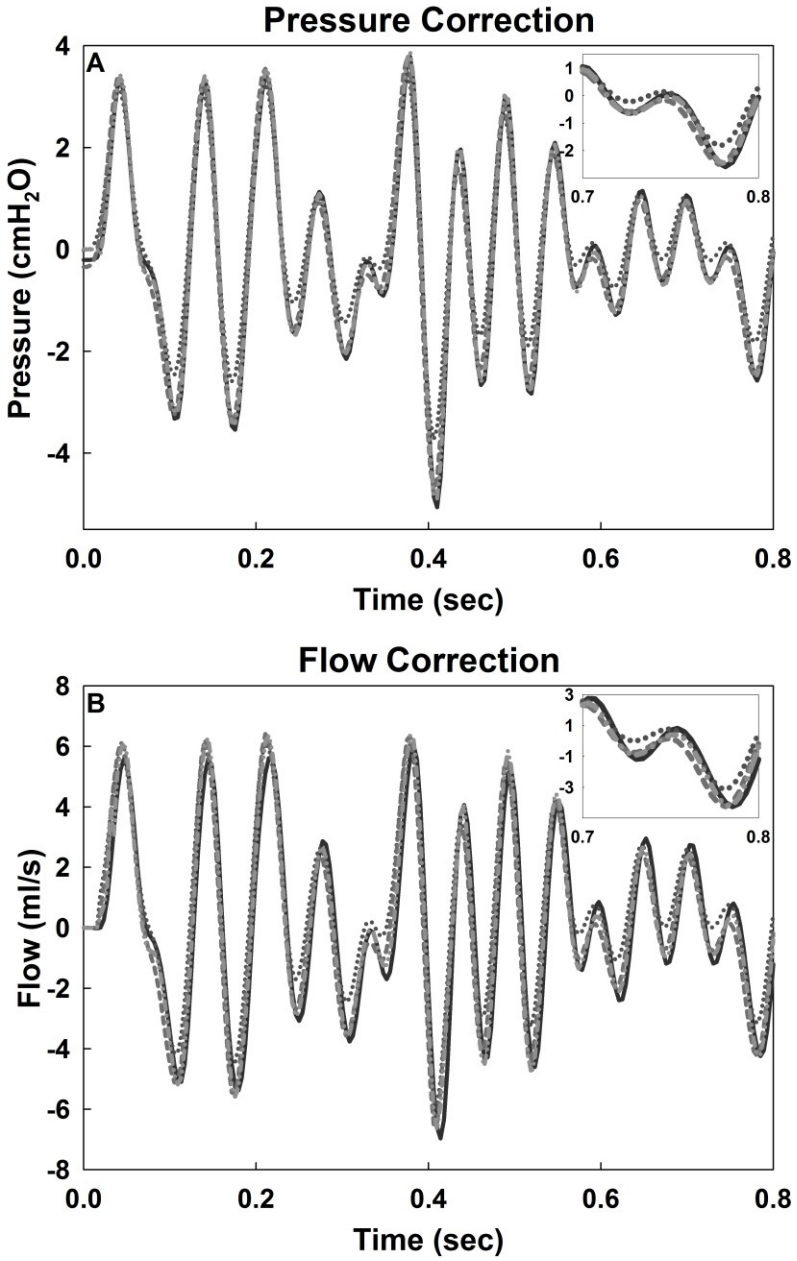

Figure A-2: Pressure and flow correction using Volterra series. A) The transducer's measured pressure (dotted) was corrected to match the pressure measured by the ventilator (solid) using two 1st order (O) Volterra series with a memory (*M*) of 1 and 6 (dash, $\bar{r}^2$=0.9635 and dash-dot, $\bar{r}^2$=0.9971 respectively). B) Then for each pressure signal a corresponding flow was plotted. Both the corrected flows, equated from the corrected pressures, with *M*=1 (dash, $\bar{r}^2$= 0.7941) and *M*=6 (dash-dot, $\bar{r}^2$=0.9355) improved the fit compared to the unadjusted flow (dotted, $\bar{r}^2$=0.6580) with the latter being superior.

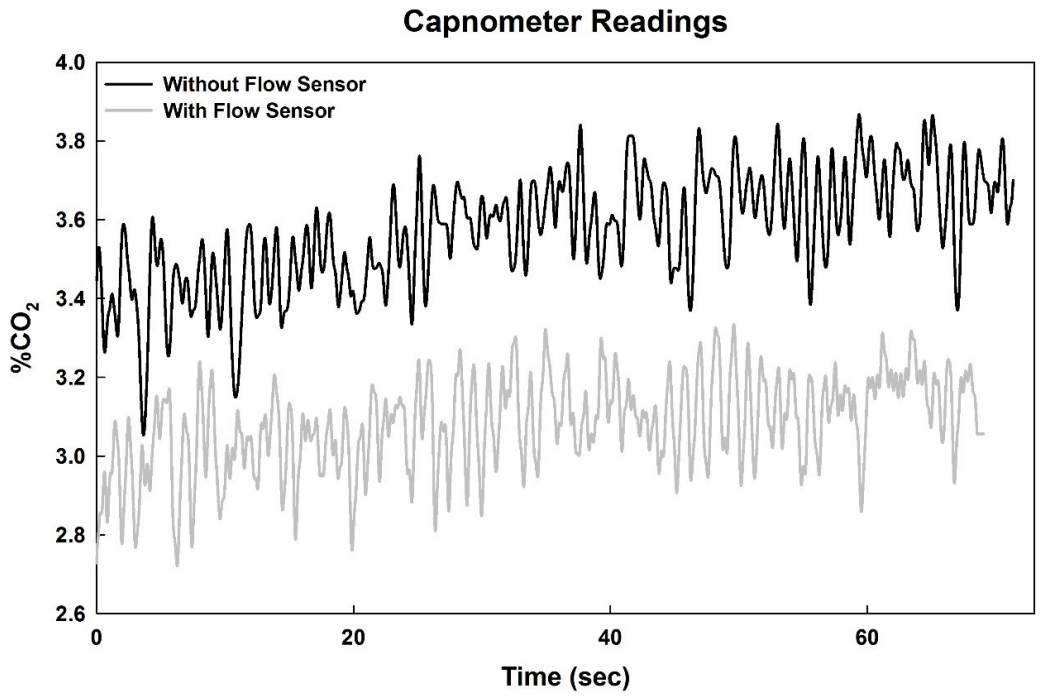

Figure A-3: Capnometer readings. Expired CO_2 in the presence or absence of the flow sensor.

Appendix B: ZVV

B.1 Human and mouse data

Table B-1: Patient biographic data.

Patient	Age (yrs)	Height (cm)	Weight (kg)	Ideal Body Weight (kg)	BMI	Respiratory Failure Etiology
1	38	187	89	80	25.5	pneumonia
2	61	179	68.2	71	21.3	pneumonia
3	31	186	79.2	77.1	22.9	non-pulmonary sepsis
4	63	170	119.9	66.1	41.5	pneumonia
5	41	160	61.5	56.9	24.0	pneumonia

Table B-2: Mouse summary results.

R_{RS} ($cmH_2O.s.mL^{-1}$) - Before Lavage							
		T1			T2		
Mouse	**Time (min)**	**Breath Number**	**Mean**	**Standard Error**	**Breath Number**	**Mean**	**Standard Error**
1	11.4	1220	2.56	0.005	1213	2.55	0.005
2	11.7	1245	1.71	0.002	1219	1.70	0.002
3	10.2	983	3.41	0.015	969	4.16	0.017
4	11.3	1211	1.60	0.002	1195	1.59	0.002
5	11.2	1189	1.91	0.003	1174	1.90	0.003
R_{RS} ($cmH_2O.s.mL^{-1}$) - After Lavage							
		T1			T2		
Mouse	**Time (min)**	**Breath Number**	**Mean**	**Standard Error**	**Breath Number**	**Mean**	**Standard Error**
1	10.4	1097	2.52	0.007	1124	2.49	0.006
2	10.3	1083	1.61	0.003	1068	1.63	0.003
3	10.4	1094	2.57	0.004	881	2.84	0.007
4	10.1	1072	2.46	0.007	1055	2.34	0.005
5	10.2	1090	1.92	0.003	1062	1.89	0.002
E_{RS} ($cmH_2O.mL^{-1}$) - Before Lavage							
		T1			T2		
Mouse	**Time (min)**	**Breath Number**	**Mean**	**Standard Error**	**Breath Number**	**Mean**	**Standard Error**
1	11.4	1220	25.05	0.162	1213	25.27	0.159
2	11.7	1245	38.50	0.084	1219	39.04	0.078
3	10.2	983	44.87	0.210	969	48.86	0.294
4	11.3	1211	38.19	0.083	1195	38.62	0.077
5	11.2	1189	38.37	0.072	1174	38.97	0.071
E_{RS} ($cmH_2O.mL^{-1}$) - After Lavage							
		T1			T2		
Mouse	**Time (min)**	**Breath Number**	**Mean**	**Standard Error**	**Breath Number**	**Mean**	**Standard Error**
1	10.4	1097	43.85	0.245	1124	39.53	0.195
2	10.3	1083	49.98	0.100	1068	49.26	0.091
3	10.4	1094	51.94	0.142	881	51.56	0.150
4	10.1	1072	51.94	0.166	1055	51.56	0.131
5	10.2	1090	51.39	0.100	1062	50.87	0.080

Table B-3: Multiple comparison test results for E_{RS} within T before and after lavage.

Mean E_{RS} ($cmH_2O.mL^{-1}$)								
Mouse	**Before lavage**			**After lavage**			**p value (T1 vs T2)**	
	T1	**T2**	**(T2-T1)/T1**	**T1**	**T2**	**(T2-T1)/T1**	**Before lavage**	**After lavage**
1	25.05	25.27	0.88%	43.85	39.53	-9.85%	0.462	**$<10^{-5}$**
2	38.50	39.04	1.40%	49.98	49.26	-1.45%	**$<10^{-5}$**	**$<10^{-5}$**
3	44.87	48.86	8.89%	51.94	51.56	-0.72%	**$<10^{-5}$**	0.60
4	38.19	38.62	1.11%	51.94	51.56	-0.73%	**0.0168**	**0.0004**
5	38.37	38.97	1.56%	51.39	50.87	-1.02%	**$<10^{-5}$**	**$<10^{-5}$**

B.2 OVW

The OVW [97] provides a composite forced oscillatory wave form at the airway opening with a peak-to-peak pressure amplitude that generates a volume signal matching the V_T delivered by the ventilator during mechanical ventilation. The frequencies present in the OVW waveform allows the computation of Z_{RS} as the ratio of the pressure-flow cross-power spectrum and the flow auto-power spectrum. The data obtained from OVW can then be used to fit the constant-phase model written as [35,182]:

$$Z_{RS} = R_N + I_{aw}j + \frac{G - jH}{\omega_n^{\alpha}} \tag{B.1}$$

where R_N, I_{aw}, G, and H are the Newtonian resistance, airway inertance, tissue damping, and tissue elastance, respectively, $\alpha = \frac{2}{\pi}\text{atan}(\frac{H}{G})$ and ω is the circular frequency (rad/s). Note that the circular frequency ω is normalized with $\omega_0 = 1$ radian so that $\omega_n = \frac{\omega}{\omega_0}$ is used in Eq. B.1 in order to obtain meaningful units for G and H [174]. For the range of frequencies applied, $I_{aw} \approx 0$. Thus, the equivalent 2-element R_{RS} and E_{RS} at the mean normalized frequency ω_m are written as:

$$R_{RS} = R_N + \frac{G}{\omega_m^{\alpha}} \tag{B.2}$$

$$E_{RS} = H\omega_m^{1-\alpha} \tag{B.3}$$

The constant-phase parameters were consequently used to calculate the equivalent R_{RS} and E_{RS} values from Eqs B.2 & B.3, respectively.

B.3 Computational study - Kelvin body and pressure transient adjustment

The equivalent resistance (R_k) and elastance (E_k) of the Kelvin body can be computed as follows [96]:

$$R_k = \frac{R_1 E_1^2}{R_1^2 \omega^2 + E_1^2} \tag{B.4}$$

$$E_k = \frac{R_1^2 E_1 \omega^2 + R_1^2 E_2 \omega^2 + E_1^2 E_2}{R_1^2 \omega^2 + E_1^2} \tag{B.5}$$

Using a minimum and a maximum F_R, and a sequence of V_T's similar to those in the human experiments, a time series of simulated VV was constructed by stitching the individual cycles together each having a different V_T and F_R creating a volume signal (V) of the form:

$$V(t) = -\frac{V_T}{2}\cos(2\pi F_R(\Delta t)) + \frac{V_T}{2} \tag{B.6}$$

where Δt represents the difference in time from the onset of each breath cycle. The flow ($\dot{V}$) was computed as the volume trace differentiated with respect to time. Next, the pressure difference (ΔP) with respect to the positive-end expiratory pressure (PEEP) was obtained for each breath using the analytical solution of the Kelvin body given by:

$$\begin{aligned} \Delta P(t) &= P(t) - PEEP \\ &= \Delta P_i e^{-\frac{E_1}{R_1}\Delta t} + \frac{V_o}{2}(E_2 - E_k)\left(1 - e^{-\frac{E_1}{R_1}\Delta t}\right) + R_k \dot{V} + E_k V \end{aligned} \tag{B.7}$$

where ΔP_i is the value of ΔP at the start of the current breath. Note that due to the variable nature of the ventilation, ΔP includes both steady-state and transient pressure contributions from previous breaths. In particular, the last 2 terms in Eq. B.7 are the conventional

resistive and elastic pressure drops respectively whereas the first 2 terms represent the transients.

In order to account for the transient effects, we approximate the transient part of ΔP, the first 2 terms in Eq. B.7 denoted by ΔP_T, to vary linearly from the beginning to the end of each breath as follows:

$$\Delta P_T(t) = 2\pi F_R\left(\Delta P_f - \Delta P_i\right)t \tag{B.8}$$

where ΔP_f is the value of ΔP at the end of the breath. Finally, the estimated steady-state pressure difference (ΔP_s) of the current breath is computed as:

$$\Delta P_s(t) = \Delta P(t) - \Delta P_T(t) \tag{B.9}$$

The concept behind this correction is that in the steady-state, the end of each breath should be the same; thus, any variation in pressure at the end of the breath is due to transients. While these transients might take different functional forms (e.g., not necessarily exponential as in the Kelvin body model), a linear approximation is the simplest. Applying this technique in several forward simulations was sufficient to reduce the error significantly (Table B-4). It is worth mentioning that for a pressure-controlled ventilation, a steady-state volume can be estimated in a similar fashion for the correction of transients.

Table B-4: Simulation results. The correction procedure was tested for 15 sets of simulations while varying different parameters. The error on E_{RS} was consistently low before and after the correction. Errors without pressure correction were very high for R_{RS}; however, the correction method consistently reduced errors as high as an order of magnitude, and the maximum error was only 3.4%.

	R_{RS}		E_{RS}	
	Maximum Error (%)		**Maximum Error (%)**	
Parameter Change*	ΔP	ΔP_s	ΔP	ΔP_s
Baseline**	-41.9	-1.9	1.50	-1.38
2Fs	-44.4	2.1	1.67	1.40
Fs/2	-35.2	1.7	2.12	2.03
$2N_b$	-37.5	-2.1	1.62	-1.38
$N_b/2$	-40.9	-2.3	1.48	-1.14
F_R = 12.5-17.5	-16.2	1.3	1.09	1.08
F_R = 7.5-22.5	-44.7	2.6	2.02	1.96
MTV = 5	-38.5	-2.2	1.56	-0.96
MTV = 10	-36.2	-1.9	1.45	-1.30
$1.25R_1$	-47.0	1.4	1.08	1.07
$0.75R_1$	-31.8	3.4	2.41	2.36
$1.25E_1$	-31.8	2.3	1.72	1.69
$0.75E_1$	-45.9	1.7	1.42	1.39
$1.25E_2$	-37.8	1.4	1.38	1.24
$0.75E_2$	-39.5	2.2	1.67	1.64

* Compared to baseline

**Baseline: Fs (sampling frequency) = 50 Hz, N_b (number of breath) = 500 breath, F_R=10-20 breath/min, MTV = 7.5 L/min, R_1 = 60 $cmH_2O.s.L^{-1}$, E_1 = 20 $cmH_2O.L^{-1}$, E_2 = 5 $cmH_2O.L^{-1}$

B.4 Time domain analysis

Using the breath-by-breath volume (V) and flow ($\dot{V}$) time data, R_{RS}, E_{RS}, and an offset (P_o) were estimated using linear regression applied to a two compartment model of the following form:

$$P(t) = R_{RS}\dot{V} + E_{RS}V + P_o \tag{B.10}$$

For finding R_{RS} and E_{RS} for the full breath, the entire period of each breath was used, whereas for inspiratory-only fitting, the inspiratory phase of the breath was used. The values of R_{RS} and E_{RS} were then binned as a function of time for both the human patients as well as the mice subjects (Figures B-1 & B-2 respectively). In general, the inspiratory-only analysis provided higher values. However, the R_{RS} and E_{RS} values in time (inspiratory-only and full cycle) and frequency (ZVV) domain were generally close to each other and showed similar trends across time. It is important to note that the advantage of binning the data as a function of F_R is that it provides frequency spectra of R_{RS} and E_{RS} which is not obtained when the data is binned in time. However, the ZVV technique can be used to bin data as a function of time as well when needed. Furthermore, similar to Figures 4-4A and 4-4B where a double binning process was applied, the binning can be done as function of F_R (primary bin) and V_T (secondary bin) that can reveal the nonlinear properties of the respiratory system for a particular V_T at a specific F_R.

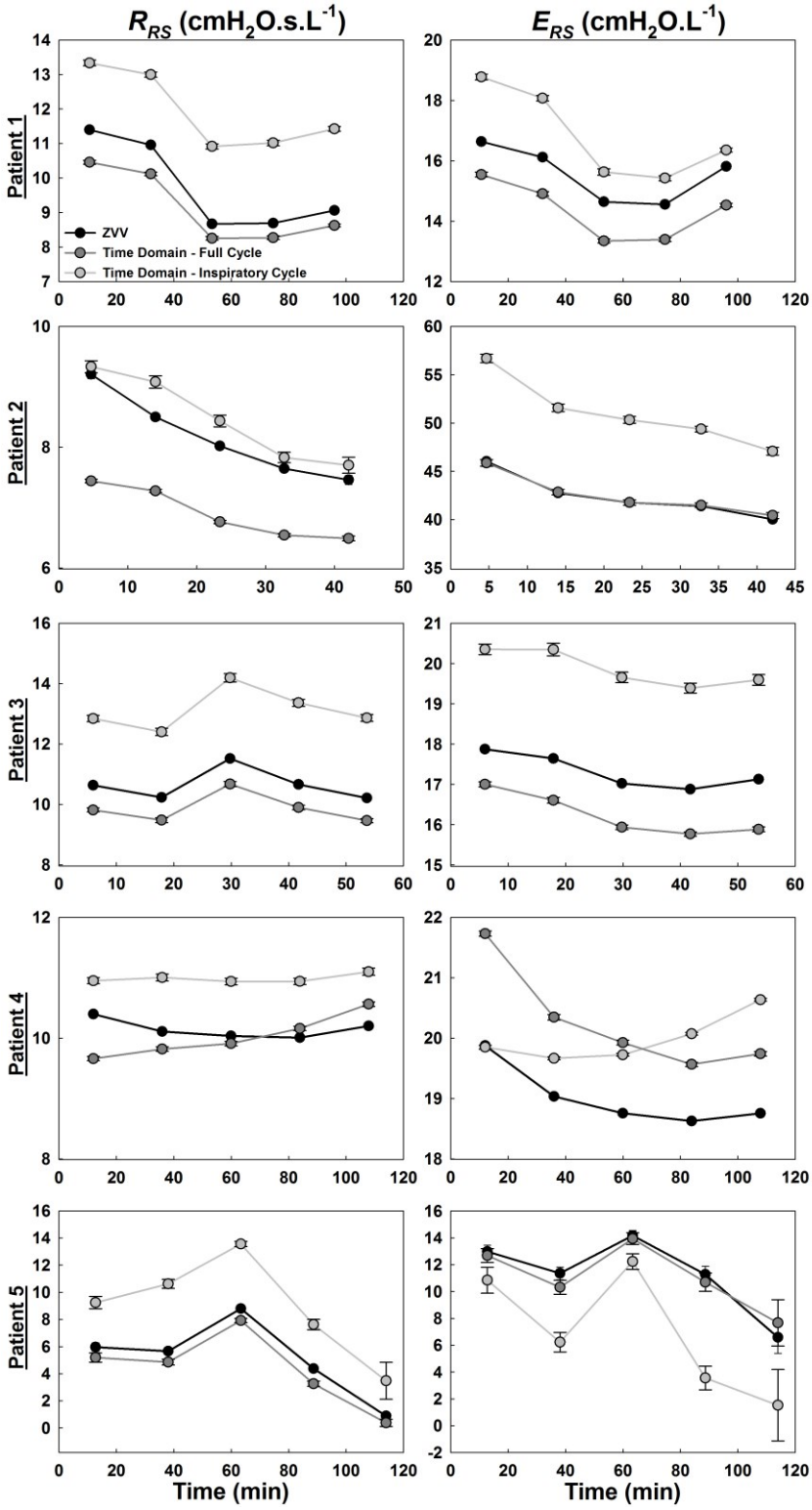

Figure B-1: Time binned human data. Fitting full cycle or inspiratory cycle in time domain.

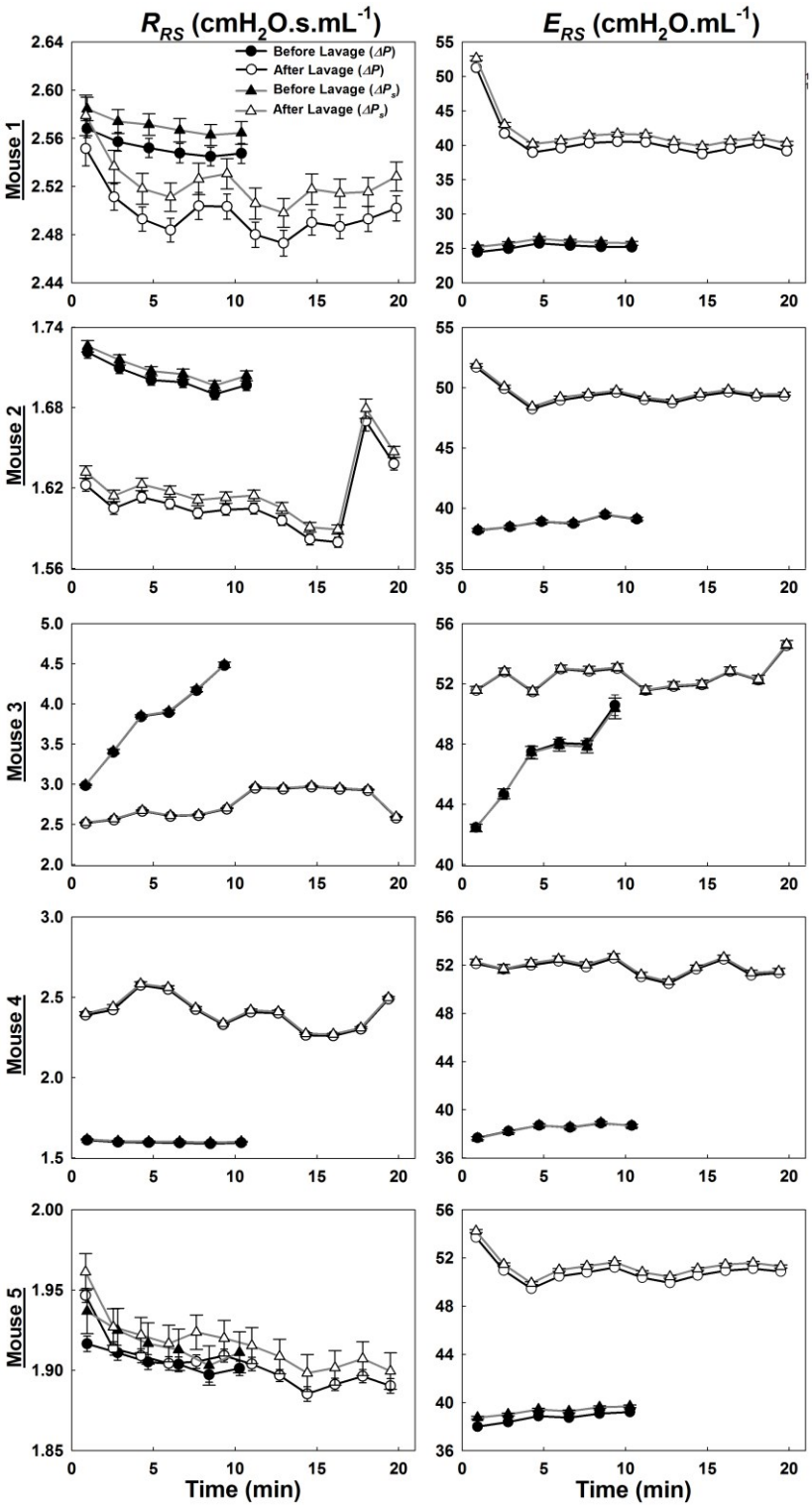

Figure B-2: Time domain mouse data using ZVV with ΔP_s and ΔP. There is an underestimation of the values with ΔP but the difference is minor.

Appendix C: Alveolar model

C.1 Model derivation

Model description

Alveolus: The model considers a thick-walled alveolus and assumes spherical geometry. The alveolar wall is described in terms of a spherical coordinate system with uppercase $(R_i \leq R \leq R_e, 0 \leq \Theta \leq 2\pi, 0 \leq \Phi \leq 2\pi)$ and lowercase $(r_i \leq r \leq r_e, 0 \leq \theta \leq 2\pi, 0 \leq \phi \leq \pi)$ symbols representing the undeformed and the deformed state, respectively. The inner and outer radii are denoted by R_i and R_e, which become r_i and r_e, respectively, during inflation. We define a general stretch ratio $\lambda = \frac{r}{R}$, an inner stretch ratio $\lambda_i = \frac{r_i}{R_i}$ and an outer stretch ratio $\lambda_e = \frac{r_e}{R_e}$. We also introduce a thickness mapping parameter $S = \frac{R}{R_i}$ to span across the alveolar thickness so that $S_i = 1 \leq S \leq \frac{R_e}{R_i} = S_e$. The wall is assumed to be incompressible, homogeneous isotropic, and deforms only in the radial direction $(\theta = \Theta, \phi = \Phi)$. Similarly, the alveolar expansion is isotropic and homogenous maintaining its spherical structure as its being inflated.

Wavy Fibers: The wall contains wavy fibers embedded in the extracellular matrix (ECM) and oriented in the circumferential direction. When the alveolus is inflated, the wavy fibers are gradually straightened and recruited. Fibers act as linear springs in parallel without any fiber-fiber or fiber-matrix interaction. Thus, nonlinearity in the mechanical behavior arises purely from the recruitment of wavy fibers. At any radius R in the undeformed state, the fibers are not stretched guaranteeing no residual stress across the wall, and the fibers contribute to force only when they are recruited (straightened). Let N_f

denote the total number of fibers in the alveolar wall with an average cross-sectional area A_f and average elastic modulus Y_f. The fractional area occupied by the fibers in the wall is $\delta_{A,f} = \frac{N_f A_f}{2\pi R_i(R_e - R_i)}$.

Next, we define the contour length or unstretched length of a fiber as $L_f = qR_f$ where R_f is the alveolar radius at which the fiber is recruited. The waviness of a fiber that is located at R is given as $w_f = \frac{qR_f(R)}{qR} = \frac{R_f(R)}{R}$. We define w_1 and w_2 as the minimum and maximum waviness at S_e, respectively. The probability distribution of R_f, denoted by $p_f(R_f, R)$, can be a function of R and is defined as the probability of finding fibers with R_f between R_f and $R_f + dR_f$ within the alveolar wall between radii R and $R + dR$, Θ and $+d\Theta$, and $\Phi + d\Phi$ such that:

$$\iint \iint p_f(R_f, R) dR_f dR d\Theta d\Phi = 1 \tag{C.1}$$

Since fiber waviness is independent of angles, p_f can be reduced to:

$$\iint p_f(R_f, R) dR_f dR = 1 \tag{C.2}$$

In terms of the dimensionless parameters waviness and S, the probability is written as:

$$\iint p_{w_f}(w_f, S) dw_f dS = 1 \tag{C.3}$$

Since the range of waviness may vary across the wall, we take this into account by using a function $G_o(S)$ such that $w_1 G_o(S) \leq w_f \leq w_2 G_o(S)$. When $G_o = 1$, the waviness distribution becomes independent of S and hence uniform throughout the wall thickness. For example, if we set $G_o(S) = \frac{S_e+1}{2S}$ such that $w_1 \frac{S_e+1}{2S} \leq w(S) \leq w_2 \frac{S_e+1}{2S}$, the waviness of

the fibers will decrease with *S*. $G_o = 1$ allows the fibers to have constant waviness but with linearly increasing fiber length across the alveolar wall, while $G_o(S) = \frac{S_e+1}{2S}$ implies a decrease in waviness but uniform fiber length across the wall. Note however, that for this specific case, the waviness of the middle layer ($S = \frac{S_e+1}{2}$) is the same for the two cases.

For a given *S*, we shall describe the waviness within the wall with the general beta distribution with its two shape parameters α and β where $B(\alpha, \beta)$ is the beta function with shape parameters α and β.Thus, by varying G_o, it is possible to shift the waviness range across *S*, while changing α and β, it is possible to create very different waviness distributions. For instance, when $\alpha = \beta = 1$, p_{w_f} becomes a uniform distribution. With these considerations, the general beta waviness distribution is:

$$p_{w_f}(w_f, S) = \frac{1}{S_e - 1} \frac{(w_f - w_1 G_o)^{\alpha-1} (w_2 G_o - w_f)^{\beta-1}}{B(\alpha, \beta)(w_2 G_o - w_1 G_o)^{\alpha+\beta-1}} \tag{C.4}$$

Matrix: If N_m is the total number of ECM units with average cross-sectional area and elastic modulus of A_m and Y_m, respectively, then the fractional area of the matrix is $\delta_{A,m} = \frac{N_m A_m}{2\pi R_i (R_e - R_i)}$. We assume these units are distributed throughout the tissue according to a uniform distribution $p_m(R) = \frac{1}{R_e - R_i}$.

The derivation is based on the model of Wuyts et al. [160] applied to a thick-walled cylindrical model of the aorta; however, using the beta distribution for fiber waviness, instead of the Lorentz function in their model, we are able to obtain analytic expressions for the true stress and the incremental stiffness across the thickness of an alveolus under large deformations.

Mass conservation

To derive the P-V curve, let us first consider a spherical shell with its inner radius R_i and thickness dR, $0 \leq \theta \leq 2\pi$, and $0 \leq \phi \leq \pi$. By applying the conservation of mass for a layer between R_i and $R = R_i + dR$, we obtain the following relations:

$$\frac{4}{3}\pi(R^3 - R_i^3) = \frac{4}{3}\pi(r^3 - r_i^3) \tag{C.5}$$

$$R = (r^3 - r_i^3 + R_i^3)^{1/3} \tag{C.6}$$

$$\frac{dR}{dr} = \frac{r^2}{(r^3 - r_i^3 + R_i^3)^{2/3}} = \frac{r^2}{R^2} = \lambda^2 \tag{C.7}$$

Note that Eq. C.7 is the inverse of the deformation gradient in r. Dividing Eq. C.6 with R_i, we can relate the general stretch ratio as a function of the internal stretch ratio (λ_i) and thickness mapping parameter (S):

$$\lambda^3(\lambda_i, S) = \frac{S^3 + \lambda_i^3 - 1}{S^3} \tag{C.8}$$

Wavy fiber circumferential stress

Let us now consider how the circumferential force at radius r arises in the deformed state. As the layer of tissue at R is stretched, a fiber with R_f is recruited when the layer is stretched to $r=R_f$. Further stretching the layer stretches the fiber to a linear strain of $(qr - qR_f)/qR_f$. The single fiber circumferential force ($f_{s,f}$) acting perpendicular to a small surface area element $rd\theta dr$ in the deformed state is thus:

$$f_{s,f} = \begin{cases} Y_f A_f \dfrac{r - R_f}{R_f} = Y_f A_f \left(\dfrac{\lambda - w_f}{w_f}\right) & for\ r > R_f\ or\ \lambda > w_f \\ 0\ otherwise \end{cases} \quad \text{(C.9)}$$

The total circumferential force due to all fibers (f_f) is thus given by:

$$d(df_f) = N_f p_{w_f}(w_f, S) Y_f A_f \left(\frac{\lambda - w_f}{w_f}\right) dw_f dS \quad \text{(C.10)}$$

The circumferential true stress in the wall is obtained by dividing the total force with the deformed area, $2\pi r dr$ $\left(\frac{2\pi R_i^2 S dS}{\lambda}\right)$ derived from Eqs. C.6, C.7, and C.8 .The true stress is written as:

$$d\sigma_{f,\theta\theta} = N_f p_{w_f}(w_f, S) Y_f A_f \left(\frac{\lambda - w_f}{w_f}\right) \frac{\lambda dw_f dS}{2\pi R_i^2 S dS} \quad \text{(C.11)}$$

If we divide the right hand side with $(R_e - R_i)$ and multiply it with $R_i(S_e - 1) = R_e - R_i$, we can use the fiber area fraction to simplify Eq. C.11 as follows:

$$d\sigma_{f,\theta\theta} = \frac{N_f A_f}{2\pi(R_e - R_i)R_i}\, p_{w_f}(w_f, S) Y_f (S_e - 1) \frac{\lambda}{S} \left(\frac{\lambda - w_f}{w_f}\right) dw_f \quad \text{(C.12)}$$

$$d\sigma_{f,\theta\theta} = \delta_f\, Y_f p_{w_f}(w_f, S)(S_e - 1) \frac{\lambda}{S} \left(\frac{\lambda - w_f}{w_f}\right) dw_f \quad \text{(C.13)}$$

we can replace $p_{w_f}(w_f, S)$ with the beta distribution:

$$d\sigma_{f,\theta\theta} = \delta_f\, Y_f \frac{\lambda}{S} \frac{(w_f - w_1 G_o)^{\alpha-1}(w_2 G_o - w_f)^{\beta-1}}{B(\alpha,\beta)(w_2 G_o - w_1 G_o)^{\alpha+\beta-1}} \left(\frac{\lambda - w_f}{w_f}\right) dw_f \quad \text{(C.14)}$$

Finally, to simplify the integration, the following transforms for w_f and λ are applied respectively:

$$w_t = \frac{w_f - w_1 G_o}{w_2 G_o - w_1 G_o} \quad \text{(C.15)}$$

$$\lambda_t = \frac{\lambda - w_1 G_o}{w_2 G_o - w_1 G_o} \tag{C.16}$$

When fibers are being recruited, $w_1 G_o < \lambda < w_2 G_o$ which is equivalent to $0 < w_t < \lambda_t$ and $0 < \lambda_t < 1$, whereas for fully recruited fibers, $\lambda > w_2 G_o$ which yields $0 < w_t < 1$ and $1 < \lambda_t < \infty$. The probability distribution function for $p_f(w_t)$ is now written as:

$$p_f(w_t) = \frac{1}{(S_e - 1)} \frac{1}{B(\alpha, \beta)} (w_t)^{\alpha - 1} (1 - w_t)^{\beta - 1} \tag{C.17}$$

where $0 < w_t < 1$ for any layer S as required by the beta distribution. Thus, the stress differential is written as:

$$d\sigma_{f,\theta\theta} = \delta_f Y_f \frac{\lambda_t (w_2 G_o - w_1 G_o) + w_1 G_o}{S} \frac{w_t^{\alpha-1}(1 - w_t)^{\beta-1}}{B(\alpha, \beta)} \left(\frac{\lambda_t - w_t}{w_t (w_2 G_o - w_1 G_o) + w_1 G_o} \right) (w_2 G_o - w_1 G_o) dw_t \tag{C.18}$$

Integrating Eq. C.18 through all waviness, the true circumferential stress due to the all fibers at a given layer S experiencing a stretch ratio λ is:

$$\sigma_{f,\theta\theta}(\lambda, S) = \frac{\delta_f Y_f}{B(\alpha, \beta)\alpha(\alpha + 1)} \frac{\lambda}{S} \frac{\lambda - w_1 G_o}{w_1 G_o} \left(\frac{\lambda - w_1 G_o}{w_2 G_o - w_1 G_o} \right)^{\alpha} \left((\alpha + 1) A_1 - \alpha B_1 \right), \; w_1 G_o < \lambda < w_2 G_o \tag{C.19}$$

$$\sigma_{f,\theta\theta}(\lambda, S) = \frac{\delta_f Y_f}{B(\alpha, \beta)\alpha(\alpha + 1)} \frac{\lambda}{S} \frac{\lambda - w_1 G_o}{w_1 G_o} \left((\alpha + 1) A_2 - \alpha B_2 \right), \; w_1 \lambda \geq w_2 G_o \tag{C.20}$$

where:

$$A_1 = F_1\left(\alpha; 1-\beta, 1\,; \alpha+1; \frac{\lambda - w_1 G_o}{w_2 G_o - w_1 G_o}, -\frac{\lambda - w_1 G_o}{w_1 G_o}\right) \tag{C.21}$$

$$B_1 = F_1\left(\alpha+1; 1-\beta, 1\,; \alpha+2; \frac{\lambda - w_1 G_o}{w_2 G_o - w_1 G_o}, -\frac{\lambda - w_1 G_o}{w_1 G_o}\right) \tag{C.22}$$

$$A_2 = F_1\left(\alpha; 1-\beta, 1\,; \alpha+1; 1, -\frac{w_2 - w_1}{w_1}\right) \tag{C.23}$$

$$B_2 = F_1\left(\alpha+1; 1-\beta, 1\,; \alpha+2; 1, -\frac{w_2 - w_1}{w_1}\right) \tag{C.24}$$

and F_1 is the Appell hypergeometric function of two variables defined as:

$$F_1(a; b, b'; c; x, y) = \sum_{m=0}^{\infty}\sum_{n=0}^{\infty} \frac{a_{m+n} b_m b'_n}{m!\, n!\, c_{m+n}} x^m y^n \tag{C.25}$$

which converges when $|x| < 1$, $|y| < 1$.

Since in most experimental cases, it is the engineering stress (σ_e) that is actually calculated, we can divide Eq. C.10 with the undeformed area ($2\pi R dR$) rather than the deformed area ($2\pi r dr$). Interestingly, this results in a factor of λ $\left(\sigma_e = \frac{\sigma}{\lambda}\right)$ for the stress equation as a consequence of the conservation of mass (Eq. C.5).

Uniform distribution stress and stiffness

For the special case of a uniform distribution of waviness ($\alpha = \beta = 1$), p_f is written as:

$$p_{w_f}(w_f, S) = \frac{1}{S_e - 1}\frac{1}{G_o}\frac{1}{w_2 - w_1} \tag{C.26}$$

Following the same procedure as above, the true stresses simplify to:

$$\sigma_{f,\theta\theta}(\lambda, S) = \frac{\delta_f Y_f}{w_2 - w_1}\frac{1}{G_o}\frac{\lambda^2}{S}\left[ln\left(\frac{\lambda}{w_1 G_o}\right) + \frac{w_1 G_o}{\lambda} - 1\right], \quad for\ \ w_1 G_o < \lambda < w_2 G_o \tag{C.27}$$

$$\sigma_{f,\theta\theta}(\lambda, S) = \frac{\delta_f Y_f}{w_2 - w_1}\frac{1}{G_o}\frac{\lambda^2}{S}\left[ln\left(\frac{w_2}{w_1}\right) + \frac{w_1 G_o}{\lambda} - \frac{w_2 G_o}{\lambda}\right], \quad for\ \lambda \geq w_2 G_o \tag{C.28}$$

Differentiating Eqs. C.27 and C.28 with respect to λ provides the incremental Young's modulus (E_f) for the thick-walled sphere:

$$E_{f,\theta\theta}(\lambda, S) = \frac{\delta_f Y_f}{w_2 - w_1}\frac{1}{G_o}\frac{\lambda}{S}\left[2ln\left(\frac{\lambda}{w_1 G_o}\right) + \frac{w_1 G_o}{\lambda} - 1\right], \quad for\ w_1 G_o < \lambda < w_2 G_o \tag{C.29}$$

$$E_{f,\theta\theta}(\lambda, S) = \frac{\delta_f Y_f}{w_2 - w_1}\frac{1}{G_o}\frac{\lambda}{S}\left[2ln(w_1) + \frac{w_1 G_o}{\lambda} - \frac{w_2 G_o}{\lambda}\right], \quad for\ \lambda \geq w_2 G_o \tag{C.30}$$

As for the engineering stress and incremental tissue stiffness (E_e) they are equal to:

$$\sigma_{ef,\theta\theta}(\lambda, S) = \frac{\delta_f Y_f}{w_2 - w_1}\frac{1}{G_o}\frac{\lambda}{S}\left[ln\left(\frac{\lambda}{w_1 G_o}\right) + \frac{w_1 G_o}{\lambda} - 1\right], for\ w_1 G_o < \lambda < w_2 G_o \tag{C.31}$$

$$\sigma_{ef,\theta\theta}(\lambda, S) = \frac{\delta_f Y_f}{w_2 - w_1}\frac{1}{G_o}\frac{\lambda}{S}\left[ln\left(\frac{w_2}{w_1}\right) + \frac{w_1 G_o}{\lambda} - \frac{w_2 G_o}{\lambda}\right], for\ \lambda \geq w_2 G_o \tag{C.32}$$

$$E_{ef,\theta\theta}(\lambda, S) = \frac{\delta_f Y_f}{w_2 - w_1}\frac{1}{G_o}\frac{1}{S}ln\left(\frac{\lambda}{w_1 G_o}\right), \quad for\ w_1 G_o < \lambda < w_2 G_o \tag{C.33}$$

$$E_{ef,\theta\theta}(\lambda, S) = \frac{\delta_f Y_f}{w_2 - w_1}\frac{1}{G_o}\frac{1}{S}ln\left(\frac{w_2}{w_1}\right), \quad for\ \lambda \geq w_2 G_o \tag{C.34}$$

Circumferential ECM stress

The circumferential force generated by the ECM can be derived similarly, but without considering waviness. Accordingly, the force is written as:

$$d(df_m) = N_m p_m(R) A_m Y_m \frac{r-R}{R} dR \tag{C.35}$$

Dividing by the deformed area $2\pi r dr$, the ECM true stress is given by:

$$\begin{aligned} \sigma_{m,\theta\theta}(r, R(r)) &= \frac{N_m A_m Y_m}{2\pi(R_e - R_i)} \frac{r-R}{R} \frac{dR}{rdr} \\ &= \frac{N_m A_m Y_m}{2\pi(R_e - R_i)} \left(\frac{r^2 - rR}{R^3} \right) \end{aligned} \tag{C.36}$$

Multiplying the numerator and denominator by R_i and writing the equation as a function of λ and S:

$$\sigma_{m,\theta\theta}(\lambda, S) = \delta_m Y_m \frac{\lambda}{S}(\lambda - 1) \tag{C.37}$$

Differentiating Eq. C.37 with respect to λ provides the incremental Young's modulus of the matrix:

$$E_{m,\theta\theta}(\lambda, S) = \delta_m Y_m \frac{1}{S}[2\lambda - 1] \tag{C.38}$$

While the engineering stress and stiffness are equal to:

$$\sigma_{e\,m,\theta\theta}(\lambda, S) = \delta_m Y_m \frac{1}{S}(\lambda - 1) \tag{C.39}$$

$$E_{e\,m,\theta\theta}(\lambda, S) = \delta_m Y_m \frac{1}{S} \tag{C.40}$$

Total circumferential stress

The total circumferential true stress $\sigma_{\theta\theta}$ and the corresponding stiffness $E_{\theta\theta}$ of the tissue is the summed combination of both the fibers and the matrix ($\sigma_{\theta\theta} = \sigma_{f,\theta\theta} + \sigma_{m,\theta\theta}$, $E_{\theta\theta} = E_{f,\theta\theta} + E_{m,\theta\theta}$). Furthermore, the fiber equation can be split into two or more entities (i.e. collagen and elastin) to account for fibers with different material and waviness properties.

Finally, the average circumferential stress across the wall at a given λ_i can be numerically calculated as :

$$\bar{\sigma}_{\theta\theta}(\lambda_i) = \frac{\int_{S_o}^{S_1} \sigma_{\theta\theta}(\lambda(S), S)dS \; + \; \int_{S_1}^{S_2} \sigma_{\theta\theta}(\lambda(S), S)dS}{S_e - 1} \tag{C.41}$$

where S_o to S_1 is the interval where the fibers are being recruited and S_1 to S_2 is the interval where the fibers are fully recruited.

Radial stress

The equations of equilibrium in spherical coordinates are given by:

$$\frac{\partial \sigma_{rr}}{\partial r} + \frac{1}{r}\frac{\partial \sigma_{r\theta}}{\partial \theta} + \frac{1}{r\,sin\,\theta}\frac{\partial \sigma_{r\phi}}{\partial \phi} + \frac{1}{r}(2\sigma_{rr} - \sigma_{\theta\theta} - \sigma_{\phi\phi} + \sigma_{r\theta}\,cot\,\theta) = 0 \tag{C.42}$$

$$\frac{\partial \sigma_{r\theta}}{\partial r} + \frac{1}{r}\frac{\partial \sigma_{\theta\theta}}{\partial \theta} + \frac{1}{r\,sin\,\theta}\frac{\partial \sigma_{\theta\phi}}{\partial \phi} + \frac{1}{r}\left[\left(\sigma_{\theta\theta} - \sigma_{\phi\phi}\right)cot\,\theta + 3\sigma_{r\theta}\right] = 0 \tag{C.43}$$

$$\frac{\partial \sigma_{r\phi}}{\partial r} + \frac{1}{r}\frac{\partial \sigma_{\theta\phi}}{\partial \theta} + \frac{1}{r\,sin\,\theta}\frac{\partial \sigma_{\phi\phi}}{\partial \phi} + \frac{1}{r}\left(2\sigma_{\theta\phi}\,cot\,\theta + 3\sigma_{r\phi}\right) = 0 \tag{C.44}$$

Due to the symmetry of the problem:

$$\frac{\partial}{\partial\theta} = \frac{\partial}{\partial\phi} = 0 \tag{C.45}$$

$$\sigma_{\theta\theta} = \sigma_{\phi\phi} \tag{C.46}$$

$$\sigma_{r\theta} = \sigma_{r\phi} \tag{C.47}$$

Thus, Eqs. 42-44 reduce to:

$$\frac{\partial\sigma_{rr}}{\partial r} + \frac{1}{r}(2\sigma_{rr} - 2\sigma_{\theta\theta} + \sigma_{r\theta}\,cot\,\theta) = 0 \tag{C.48}$$

$$\frac{\partial\sigma_{r\theta}}{\partial r} + \frac{3\sigma_{r\theta}}{r} = 0 \tag{C.49}$$

$$\frac{\partial\sigma_{r\phi}}{\partial r} + \frac{1}{r}\left(2\sigma_{\theta\phi}\,cot\,\theta + 3\sigma_{r\phi}\right) = 0 \tag{C.50}$$

Due to symmetry of the problem and comparing Eq. C.49 to Eq. C.50, $\sigma_{\theta\phi} = 0$. By employing Eq. C.6 , we can express r as $r = R_i(S^3 + \lambda_i^3 - 1)^{1/3}$, from which $dr = R_i \frac{S^2}{\left(S^3+\lambda_i^3-1\right)^{2/3}} dS$. Utilizing these and the relation $R = R_i S$, Eq. C.49 can be rewritten as:

$$\frac{\partial\sigma_{r\theta}}{\sigma_{r\theta}} + 3\frac{S^2}{S^3 + \lambda_i^3 - 1}dS = 0 \tag{C.51}$$

and the solution is given by:

$$\sigma_{r\theta}(\lambda_i, S) = \frac{C}{S^3 + \lambda_i^3 - 1} \tag{C.52}$$

where C is an arbitrary constant. Since $\sigma_{r\theta}(\lambda_i = 1) = 0$ for any S, $C = 0$ and hence $\sigma_{r\theta} = 0$. In a similar fashion, Eq. C.48 can be written as:

$$\frac{\partial\sigma_{rr}}{\partial S} + 2\frac{S^2}{S^3 + \lambda_i^3 - 1}\sigma_{rr} = 2\frac{S^2}{S^3 + \lambda_i^3 - 1}\sigma_{\theta\theta} \tag{C.53}$$

The solution is obtained by integration:

$$\sigma_{rr}(\lambda_i, S) = \frac{2}{(S^3 + \lambda_i^3 - 1)^{2/3}} \int_{S=1}^{S=S_e} \frac{S^2}{(S^3 + \lambda_i^3 - 1)^{\frac{1}{3}}} \sigma_{\theta\theta}(\lambda_i, S) dS \tag{C.54}$$

The mean radial pressure ($\bar{\sigma}_{rr}$) is calculated:

$$\bar{\sigma}_{rr}(\lambda_i) = \frac{\left[\int_{S=1}^{S=S_e} \frac{S^2}{(S^3 + \lambda_i^3 - 1)^{1/3}} \sigma_{\theta\theta}(\lambda_i, S) dS\right]\left[\int_{S=1}^{S=S_e} \frac{2}{(S^3 + \lambda_i^3 - 1)^{2/3}} dS\right]}{S_e - 1} \tag{C.55}$$

Alveolar pressure, volume, elastance, and tension

The alveolar pressure (P_{alv}) is evaluated as:

$$P_{alv} = \sigma_{rr}(\lambda_i, S = 1) = \frac{2}{\lambda_i^2} \int_{S=1}^{S_e} \frac{S^2}{(S^3 + \lambda_i^3 - 1)^{1/3}} \sigma_{\theta\theta}(\lambda_i, S) dS \tag{C.56}$$

The change in volume (ΔV) normalized by the initial volume (V_o) for an alveolus is:

$$\frac{\Delta V}{V_o} = \lambda_i^3 - 1 \tag{C.57}$$

The specific alveolar elastance E_s is defined as:

$$E_s = V_o \frac{dP_{alv}}{dV_{alv}} \tag{C.58}$$

The tension can be calculated from the circumferential stress:

$$T_{\theta\theta}(\lambda_i, S) = \int_{r=r_i}^{r_e} \sigma_{\theta\theta} dr = R_i \int_{S=1}^{S_e} \sigma_{\theta\theta} \frac{S^2}{(S^3 + \lambda_i^3 - 1)^{2/3}} dS \tag{C.59}$$

Analytical approximations for a thin-sphere model

Assuming a thin sphere, the average circumferential stress across the wall is equal to the stress in the middle layer $S_m = \frac{S_e+1}{2}$. Thus, the circumferential stress and all related quantities such as the circumferential stiffness, alveolar pressure, specific elastance and tension can be approximated from there thick-wall equations (Eqs. C.41, C.56, C.58, and C.59) as:

$$\bar{\sigma}_{\theta\theta} \cong \sigma_{\theta\theta}(\lambda_m, S_m) \tag{C.60}$$

$$\bar{E}_{\theta\theta} \cong E_{\theta\theta}(\lambda_m, S_m) \tag{C.61}$$

$$P_{alv}(\lambda_i) \cong \bar{\sigma}_{\theta\theta} \left[\frac{\lambda_e^2}{\lambda_i^2} S_e^2 - 1\right] \tag{C.62}$$

$$E_s \cong \frac{\bar{E}_{\theta\theta}(\lambda_i^2 \lambda_e^3 S_e^3 - \lambda_i^4 \lambda_e S_e) - \bar{\sigma}_{\theta\theta} \lambda_m^2 S_m^2 (S_e^3 - 1)}{\lambda_i^4 \lambda_e \lambda_m^2 S_e S_m^2} \tag{C.63}$$

$$\bar{T}_{\theta\theta}(\lambda_i, S) \cong \bar{\sigma}_{\theta\theta} R_i \lambda_i \left(\frac{\lambda_e}{\lambda_i} S_e - 1\right) \tag{C.64}$$

Finally, relating pressure to tension:

$$P_{alv}(\lambda_i) \cong \frac{\bar{T}_{\theta\theta}}{R_i \lambda_i \left(\frac{\lambda_e}{\lambda_i} S_e - 1\right)} \left[\frac{\lambda_e^2}{\lambda_i^2} S_e^2 - 1\right] \cong \frac{T_{\theta\theta}}{R_i \lambda_i} \left[\frac{\lambda_e}{\lambda_i} S_e + 1\right] \tag{C.65}$$

$$P_{alv}(\lambda_i) \cong \frac{\bar{T}_{\theta\theta}}{r_i} \left[\frac{\lambda_e R_e}{\lambda_i R_i} + 1\right] \cong \frac{\bar{T}_{\theta\theta}}{r_i} \left[\frac{r_e}{r_i} + 1\right] \cong 2 \frac{\bar{T}_{\theta\theta}(\lambda_i)}{r_i} \tag{C.66}$$

The latter relation is consistent with the Laplace equation. However, our formulation now relates $\bar{T}_{\theta\theta}$ to the components of the alveolar wall.

Fiber stress distribution

To find the probability distribution of the stress $p_\sigma(\lambda)$ we utilize the identity:

$$\left|p_\sigma(\lambda)d\sigma_f\right| = \left|p_{w_f}(w_f)dw_f\right| \tag{C.67}$$

Thus, we can write:

$$p_{\sigma_f}(\lambda) = p_{w_f}(w_f)\left|\frac{dw_f}{d\sigma\sigma_f}\right| \tag{C.68}$$

$$p_{\sigma_f}(\lambda) = \frac{Y_f\lambda}{S_e - 1}\frac{\left(Y_f\lambda - w_1G_o(\sigma_f + Y_f)\right)^{\alpha-1}\left(w_2G_o(\sigma_f + Y_f) - Y_f\lambda\right)^{\beta-1}}{B(\alpha,\beta)(w_2G_o - w_1G_o)^{\alpha+\beta-1}\left(\sigma_f + Y_f\right)^{\alpha+\beta}} \tag{C.69}$$

where the range of fiber stress on the single fibers, maximum ($\sigma_{f,max}$) and minimum ($\sigma_{f,min}$), are equal to:

$$\sigma_{f,max} = Y_f\left(\frac{\lambda - w_1G_o}{w_1G_o}\right) \text{ and } \sigma_{f,min} = Y_f\left(\frac{\lambda - w_2G_o}{w_2G_o}\right), \ \lambda > w_2G_o \tag{C.70}$$

$$\sigma_{f,max} = Y_f\left(\frac{\lambda - w_1G_o}{w_1G_o}\right) \text{ and } \sigma_{f,min} = 0, \qquad w_1G_o < \lambda < w_2G_o \tag{C.71}$$

C.2 Uniaxial stretching

Considering a rectangular geometry for the alveolar wall tissue strips. The tissue is stretched uniaxially in the Cartesian direction of *x* with a constant stretch ratio across the thickness ($\lambda = \frac{x}{X}$). Conservation of mass from initial dimensions *X*, *Y*, and *Z* to deformed *x*, *y*, and *z* provides:

$$XYZ = xyz \tag{C.72}$$

Noting that the deformed area is $A = yz = \frac{XYZ}{x} = \frac{YZ}{\lambda}$, the differential stress from Eq. C.10 for a rectangular tissue strip is:

$$d\sigma_{f,\theta\theta} = N_f p_f(w_f) Y_f A_f \left(\frac{\lambda - w_f}{w_f}\right) \frac{\lambda dw_f}{YZ} \tag{C.73}$$

$$d\sigma_{f,\theta\theta} = \frac{N_f A_f}{YZ} Y_f p_f(w_f) \left(\frac{\lambda - w_f}{w_f}\right) \lambda dw_f \tag{C.74}$$

$$d\sigma_{f,\theta\theta} = \delta_f Y_f p_f(w_f) \left(\frac{\lambda - w_f}{w_f}\right) \lambda dw_f \tag{C.75}$$

Which upon integration yields:

$$\sigma(\lambda) = \frac{\delta_f Y_f}{B(\alpha,\beta)\alpha(\alpha+1)} \lambda \frac{\lambda - w_1 G_o}{w_1 G_o} \left(\frac{\lambda - w_1 G_o}{w_2 G_o - w_1 G_o}\right)^{\alpha} \big((\alpha+1)A_1 - \alpha B_1\big) \quad w_1 G_o < \lambda < w_2 G_o \tag{C.76}$$

$$\sigma(\lambda, S) = \frac{\delta_f Y_f}{B(\alpha,\beta)\alpha(\alpha+1)} \lambda \frac{\lambda - w_1 G_o}{w_1 G_o} \big((\alpha+1)A_2 - \alpha B_2\big) \quad \lambda \geq w_2 G_o \tag{C.77}$$

Appendix D: Uniaxial model

D.1 Model derivation

Assume an alveolar wall of tensile elastic modulus Y_a and rotational elastic modulus Y_b embedded in a lung tissue strip with initial length X_i (Figure D-1 A). The alveolar wall has an initial angle θ_i with respect to the horizontal axis and an initial length l_i. As the macroscopic tissue is stretched by an incremental displacement dX from an arbitrary current position $s-1$ to a new position s ($s = 1,2,3$ ...), a microscopic tissue block, defined at every new step as the rectangular area whose diagonal is the wall's end-to-end distance, will deform and stretch by dx. Assuming affine transformations, the strain on the current tissue block will equal the strain on the whole tissue in the direction of stretch (Figure D-1 A). However, while the tissue block follows the affine transformation, the alveolar wall can rotate and/or stretch and thus the strain on the wall does not need to follow the affine deformation assumption (Figure D-1 B). Since the tissue block follows the alveolar wall at each step as the alveolar wall rotates, the new microscopic tissue block will have an initial length x_i ($x_i = l_i \cos\theta_{s-1}$) (Figure D-1 A).

Due to the small microscopic displacement dx from the arbitrary current position $s-1$ to the new position s (Figure D.1 B), the wall's incremental length (dl_{is}) and incremental angle change ($d\theta_{is}$) are given respectively as:

$$dl_{is} = l_s - l_{s-1} \tag{D.1}$$

$$d\theta_{is} = \theta_s - \theta_{s-1} \tag{D.2}$$

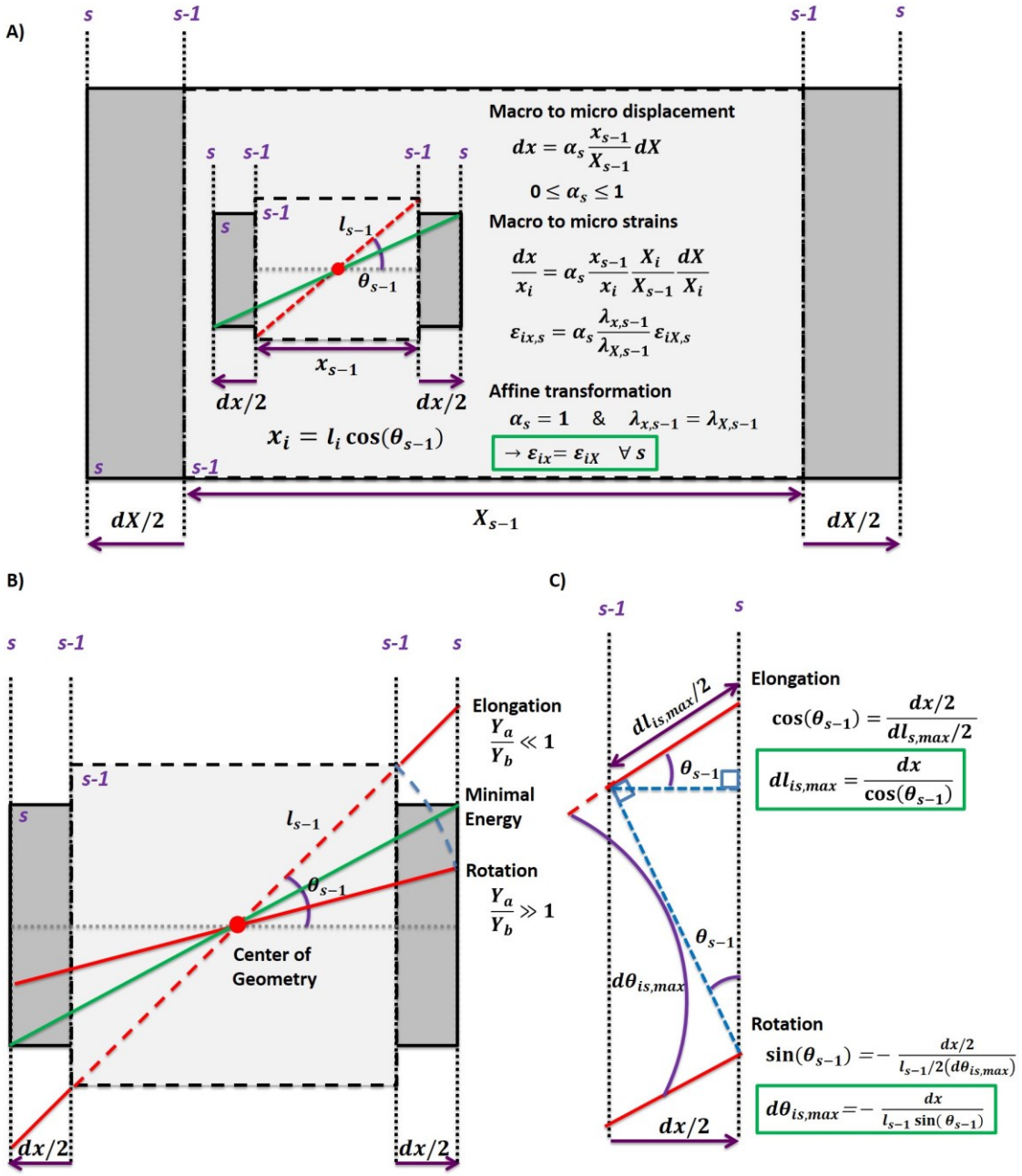

Figure D-1: Uniaxial model illustration. A) A microscopic rectangular block of tissue is defined as to confine an alveolar wall. Due to a macroscopic horizontal displacement dX, the combined microscopic tissue-wall entity will displace microscopically by dx. dx can follow an affine deformation where the incremental microscopic and macroscopic strains are equal ($\alpha = 1$), or it could not displace at all ($\alpha = 0$). We shall assume that the tissue block follows an affine transformation. This guarantees that a microscale tissue block follows the macroscale deformation. However, a single wall can have a different strain than the macroscopic strain imposed on the tissue strip because it has the ability to rotate. B) An

alveolar wall (dashed red line) with initial angle θ_{s-1} and length l_{s-1} is embedded within the microscopic lung tissue block which is stretched by a microscopic displacement *dx*. The wall has two extreme points governed by the ratio of tensile to rotational elastic modulus. If the ratio is much smaller than 1, the wall will elongate without any rotation but if the ratio is much larger than 1 the wall will rotate without any elongation. It is assumed that the wall will rotate around its center of geometry and elongate symmetrically from either end. The wall's new position (green solid line) must be on the vertical line connecting the two extreme points that either involve pure rotating or pure elongation. The actual position will involve both rotation and elongation and would be between these two extreme points at the location which minimizes total wall energy. C) For small displacements, the maximum rotation and elongation are a linear function of *dx*.

Under the assumptions that the wall will displace to a point of minimum alveolar wall energy, there are two extreme cases for the wall's new position; the wall either only elongates or only rotates (Figure D-1B).

For the case when $\frac{Y_a}{Y_b} \ll 1$, the wall will only elongate to minimize energy. Thus, the equations are written as:

$$d\theta_{is,min} = 0 \tag{D.3}$$

$$dl_{is,max} = \frac{dx}{\cos(\theta_{s-1})} \tag{D.4}$$

When $\frac{Y_a}{Y_b} \gg 1$, the wall will only rotate to minimize energy, and this is expressed by:

$$d\theta_{is,max} = \cos^{-1}\left(\frac{l_{s-1}cos(\theta_{s-1}) + dx}{l_{s-1}}\right) - \theta_{s-1} \tag{D.5}$$

$$dl_{is,min} = 0 \tag{D.6}$$

In reality, the alveolar wall can be located at any point on the vertical line connecting these two extremes (Figure D-1A). Assuming small displacements and maintaining a positive

slope, the relationship between the incremental change in length and angle can be represented as linear:

$$dl_{is} = -\frac{dl_{is,max}}{d\theta_{is,max}} d\theta_{is} + dl_{is,max} \tag{D.7}$$

due to small angle displacements (Figure A.1 B), the following approximations can be used:

$$\tan(\theta_{s-1}) \cong -\frac{dl_{is,max}}{l_{s-1} d\theta_{is,max}} \tag{D.8}$$

$$-\frac{dl_{is,max}}{d\theta_{is,max}} \cong l_{s-1}\tan(\theta_{s-1}) \tag{D.9}$$

and

$$d\theta_{is} \cong \Delta\theta_{is} \tag{D.10}$$

Therefore, the relation between incremental angle and incremental length is:

$$dl_{is} \cong l_{s-1}\tan(\theta_{s-1})\Delta\theta_{is} + dl_{is,max} \tag{D.11}$$

$$dl_{is} \cong l_{s-1}\tan(\theta_{s-1})\Delta\theta_{is} + \frac{dx}{\cos(\theta_{s-1})} \tag{D.12}$$

Dividing by the initial length of the wall (l_i) we can write the expression:

$$\varepsilon_{is} \cong (1+\varepsilon_{s-1})\tan(\theta_{s-1})\Delta\theta_{is} + \varepsilon_{ix} \tag{D.13}$$

where ε_{is} is the incremental strain of the wall:

$$\varepsilon_{is} = \frac{dl_s}{l_i} = \frac{l_s - l_{s-1}}{l_i} \tag{D.14}$$

and ε_s is the wall's strain defined as:

$$\varepsilon_s = \frac{l_s - l_i}{l_i} = \frac{l_s - l_{s-1}}{l_i} + \frac{l_{s-1} - l_i}{l_i} = \varepsilon_{is} + \varepsilon_{s-1} \tag{D.15}$$

and ε_{ix} is the incremental microscopic strain of the tissue block in the direction of stretch

$$\varepsilon_{ix} = \frac{dx}{l_i \cos(\theta_{s-1})} = \frac{dx}{x_i} \tag{D.16}$$

which is assumed to equal the incremental macrostrain for affine deformations.

Let p_1 and p_2 represent the slope and y-intercept of the relation between Δl_{is} and $\Delta\theta_{is}$ respectively:

$$p_1 = (1 + \varepsilon_{s-1}) \tan(\theta_{s-1}) \tag{D.17}$$

$$p_2 = \varepsilon_{ix} \tag{D.18}$$

Thus:

$$\varepsilon_{is} = p_1 \, \Delta\theta_{is} + p_2 \tag{D.19}$$

and let ε_{is}^* and $\Delta\theta_{is}^*$ be the actual incremental strain and incremental angle for the wall which minimize the total elastic energy of the wall.

For a linearly elastic wall with a tensile spring constant k and a rotational spring constant b, the energy (E_s) at a given stretch is given by:

$$E_s = \frac{k(l_s - l_i)^2}{2} + \frac{b(\theta_s - \theta_i)^2}{2} \tag{D.20}$$

By introducing the cross-sectional area of the alveolar wall A_s and its volume V_s at step s, the intrinsic energy e_s is:

$$e_s = \frac{E_s}{V_s} = \frac{k(l_s - l_i)^2}{2A_s l_s} + \frac{b(\theta_s - \theta_i)^2}{2V_s} \tag{D.21}$$

Introducing the initial cross-sectional area of the alveolar wall A_i and its volume V_i, assuming incompressible wall, and applying the conservation of mass for the wall ($V_s = V_i = A_s l_s = A_i l_i$) Eq. D.21 can be written as:

$$e_s = \frac{Y_a(\varepsilon_s)^2}{2} + \frac{Y_b(\theta_s - \theta_i)^2}{2} \tag{D.22}$$

where Y_a and Y_b are the tensile and rotational elastic modulus of the wall defined respectively as:

$$Y_a = \frac{kl_i}{A_i} \tag{D.23}$$

$$Y_b = \frac{b}{V_i} \tag{D.24}$$

Using Eq. D.22 and introducing the optimal strain and angle:

$$e_s = \frac{Y_a(\varepsilon_{is}^* + \varepsilon_{s-1})^2}{2} + \frac{Y_b(\Delta\theta_{is}^* + \Delta\theta_{s-1})^2}{2} \tag{D.25}$$

$$e_s = e_{s-1} + \frac{Y_a(\varepsilon_{is}^*)^2}{2} + \frac{Y_b(\Delta\theta_{is}^*)^2}{2} + Y_a\varepsilon_{is}^*\varepsilon_{s-1} + Y_b\Delta\theta_{is}^*\Delta\theta_{s-1} \tag{D.26}$$

$$e_s = e_{s-1} + \frac{Y_a(\varepsilon_{is}^*)^2}{2} + \frac{Y_b\left(\frac{\varepsilon_{is}^* - p_2}{p_1}\right)^2}{2} + Y_a\varepsilon_{is}^*\varepsilon_{s-1} + Y_b\left(\frac{\varepsilon_{is}^* - p_2}{p_1}\right)\Delta\theta_{s-1} \tag{D.27}$$

The position of the wall at *s* can be found by minimizing the intrinsic energy through setting its derivative with respect to the incremental strain to zero:

$$\frac{de_s}{d\varepsilon_{is}^*} = 0 \tag{D.28}$$

$$\frac{de_s}{d\varepsilon_{is}^*} = Y_a(\varepsilon_{is}^*) + Y_b\left(\frac{\varepsilon_{is}^* - p_2}{p_1^2}\right) + Y_a\varepsilon_{s-1} + \frac{Y_b\Delta\theta_{s-1}}{p_1} \tag{D.29}$$

Thus:

$$\varepsilon_{is}^{*} = \frac{p_2 - p_1^2 \frac{Y_a}{Y_b}\varepsilon_{s-1} - \Delta\theta_{s-1} p_1}{1 + \frac{Y_a}{Y_b} p_1^2} \tag{D.30}$$

$$\varepsilon_{is}^{*} = \frac{\varepsilon_{ix} - \frac{Y_a}{Y_b}(1+\varepsilon_{s-1})^2 \varepsilon_{s-1} \tan^2(\theta_{s-1}) - (1+\varepsilon_{s-1})\Delta\theta_{s-1}\tan(\theta_{s-1})}{1 + \frac{Y_a}{Y_b}(1+\varepsilon_{s-1})^2 \tan^2(\theta_{s-1})} \tag{D.31}$$

And from Eq. D.19:

$$\Delta\theta_{is}^{*} = -\frac{\frac{Y_a}{Y_b} p_1 p_2 + \frac{Y_a}{Y_b}\varepsilon_{s-1} p_1 + \Delta\theta_{s-1}}{1 + \frac{Y_a}{Y_b} p_1^2} \tag{D.32}$$

$$\Delta\theta_{is}^{*} = -\frac{\frac{Y_a}{Y_b}[\varepsilon_{ix} + \varepsilon_{s-1}](1+\varepsilon_{s-1})\tan(\theta_{s-1}) + \Delta\theta_{s-1}}{1 + \frac{Y_a}{Y_b}(1+\varepsilon_{s-1})^2 \tan^2(\theta_{s-1})} \tag{D.33}$$

And the intrinsic energy equation D.25 for a single alveolar wall becomes:

$$e_s = e_{s-1} + \frac{Y_a}{2}\left[\frac{p_2^2}{1 + \frac{Y_a}{Y_b} p_1^2}\right]\left[1 + 2\frac{\varepsilon_{s-1}}{p_2} - 2\Delta\theta_{s-1}\frac{p_1}{p_2} - \frac{1}{p_2^2}\frac{Y_a}{Y_b}\left(\varepsilon_{s-1} p_1 + \frac{Y_b}{Y_a}\Delta\theta_{s-1}\right)^2\right] \tag{D.34}$$

$$e_s = e_{s-1} + \frac{Y_a}{2}\left[\frac{1}{1+\frac{Y_a}{Y_b}(1+\varepsilon_{s-1})^2 tan^2(\theta_{s-1})}\right]\Big[\varepsilon_{ix}^2 + 2\varepsilon_{ix}[\varepsilon_{s-1} - (1+\varepsilon_{s-1})\tan(\theta_{s-1})\Delta\theta_{s-1}] - \frac{Y_a}{Y_b}\left(\varepsilon_{s-1}(1+\varepsilon_{s-1})\tan(\theta_{s-1}) + \frac{Y_b}{Y_a}\Delta\theta_{s-1}\right)^2\Big] \quad \text{(D.35)}$$

This can be written as effective terms of alveolar strain ($\varepsilon_{s,eff}$) and an effective alveolar stiffness ($Y_{eff,s}$):

$$e_s = e_{s-1} + \frac{1}{2}Y_{eff,s}\varepsilon_{s,eff}^2 \quad \text{(D.36)}$$

where the effective alveolar strain $\varepsilon_{s,eff}$ is related to the alveolar strain, alveolar angle, and incremental macroscopic strain:

$$\varepsilon_{s,eff}^2 = [\varepsilon_{ix} + \varepsilon_{s-1} - (1+\varepsilon_{s-1})\tan(\theta_{s-1})\Delta\theta_{s-1}]^2 - [\varepsilon_{s-1} - (1+\varepsilon_{s-1})\tan(\theta_{s-1})\,\Delta\theta_{s-1}]^2 - \left[\sqrt{\frac{Y_a}{Y_b}}\varepsilon_{s-1}(1+\varepsilon_{s-1})\tan(\theta_{s-1}) + \sqrt{\frac{Y_b}{Y_a}}\Delta\theta_{s-1}\right]^2 \quad \text{(D.37)}$$

and the wall's effective stiffness $Y_{eff,s}$ is:

$$Y_{eff,s} = \frac{Y_a}{1+\frac{Y_a}{Y_b}(1+\varepsilon_{s-1})^2\tan^2(\theta_{s-1})} \quad \text{(D.38)}$$

The stress on an individual wall (σ_a) in the direction of stretch is:

$$\sigma_a(s) = \frac{de_s(s)}{d\varepsilon_{ix}} \quad \text{(D.39)}$$

$$\sigma_a(s) = Y_{eff,s}\,[\varepsilon_{ix} + \varepsilon_{s-1} - (1+\varepsilon_{s-1})\tan(\theta_{s-1})\Delta\theta_{s-1}] \quad \text{(D.40)}$$

And the alveolar wall's incremental modulus (Y_{ia}) is:

$$Y_{ia}(s) = \frac{d\sigma_a(s)}{d\varepsilon_{ix}} = Y_{eff,s} \tag{D.41}$$

Finally, the total energy of the tissue (E_T) is calculated by summing up the energy of each wall:

$$E_T = \sum_{n=1}^{N} E_{n,s} \tag{D.42}$$

and the total tissue stress (σ_T) is equated as:

$$\begin{aligned} \sigma_T(s) = \frac{d}{d\varepsilon_{ix}}\left(\frac{E_T(s)}{V_T}\right) = \frac{1}{V_T}\frac{dE_T(s)}{d\varepsilon_{ix}} = \sum_{n=1}^{N}\frac{1}{V_T}\frac{dE_{n,s}}{d\varepsilon_{ix}} \\ = \sum_{f=n}^{N}\frac{V_i}{V_T}\sigma_a(s) \end{aligned} \tag{D.43}$$

$$\begin{aligned} \sigma_T(s) = \sum_{n=1}^{N}\delta_{n,a}Y_{n,a}\alpha_{n,s-1}\left[\varepsilon_{ix} + \varepsilon_{n,s-1}\right. \\ \left. + \left(1+\varepsilon_{n,s-1}\right)\left(\theta_{n,i} - \theta_{n,s-1}\right)\tan(\theta_{n,s-1})\right] \end{aligned} \tag{D.44}$$

where δ_a is the volume fraction of a single alveolar wall and V_T is the total tissue volume. We can simplify this expression by replacing individual alveolar volume fraction and stiffness in the summation with their average value and defining δ_T as the total volume fraction of the alveolar walls or alveoli in the tissue:

$$\delta_T = N\delta_a \tag{D.45}$$

Thus:

$$\sigma_T(s) = \delta_T Y_a \frac{1}{N}\sum_{n=1}^{N} \frac{\varepsilon_{ix} + \ \varepsilon_{n,s-1} + \left(1+\varepsilon_{n,s-1}\right)\left(\theta_{n,i} - \theta_{n,s-1}\right)\tan(\theta_{n,s-1})}{1 + \frac{Y_a}{Y_b}(1+\varepsilon_{s-1})^2\tan^2(\theta_{s-1})} \tag{D.46}$$

Furthermore, assuming an effective tensile and rotational elastic modulus given as:

$$Y_{ae} = \delta_T Y_a \tag{D.47}$$

$$Y_{be} = \delta_T Y_b \tag{D.48}$$

the final expression of stress is written as follows:

$$\sigma_T(s) = Y_{ae} \frac{1}{N}\sum_{n=1}^{N} \frac{\varepsilon_{ix} + \ \varepsilon_{n,s-1} + \left(1+\varepsilon_{n,s-1}\right)\left(\theta_{n,i} - \theta_{n,s-1}\right)\tan(\theta_{n,s-1})}{1 + \frac{Y_{ae}}{Y_{be}}(1+\varepsilon_{s-1})^2\tan^2(\theta_{s-1})} \tag{D.49}$$

Note that the individual wall's incremental strain and angle are a function of the elastic modulus ratio values, so they can simply be written as a ratio of either the absolute or effective elastic modulus values. Thus, the model can be used to fit stress-strain data and extract the effective values. However, with the knowledge of the total wall volume fraction, the absolute elastic modulus values can also be estimated. Finally, the tissue's incremental modulus (Y_T) is:

$$\begin{aligned} Y_T(s) = \frac{d\sigma_T}{d\varepsilon_{ix}} &= \frac{1}{N}\sum_{n=1}^{N} Y_{eff,s} \\ &= \frac{1}{N}\sum_{n=1}^{N} \frac{Y_a}{1 + \frac{Y_a}{Y_b}(1+\varepsilon_{s-1})^2\tan^2(\theta_{s-1})} \end{aligned} \tag{D.50}$$

D.2 Forward simulations (alveolar number and incremental strain)

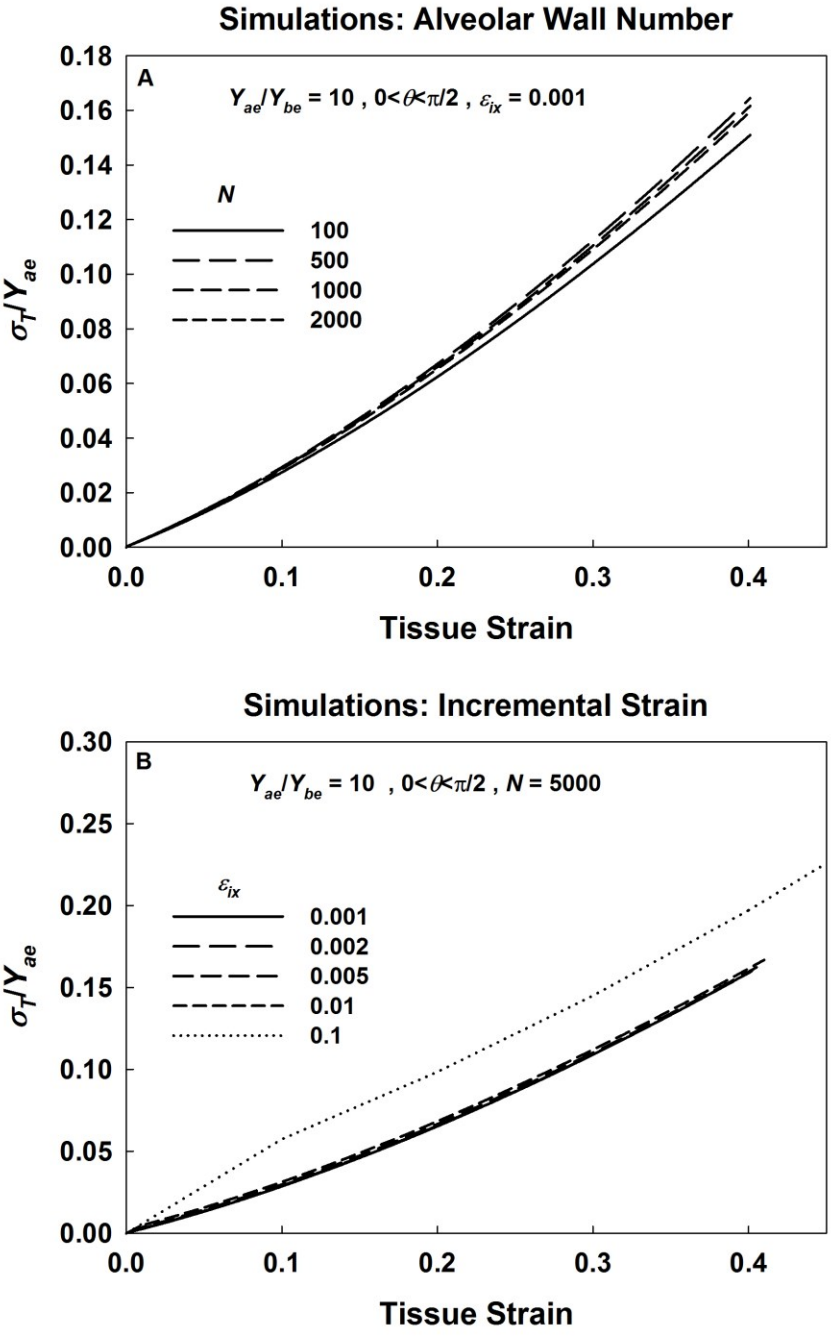

Figure D-2: Effects of alveolar wall number and model strain.

D.3 Model to network comparison

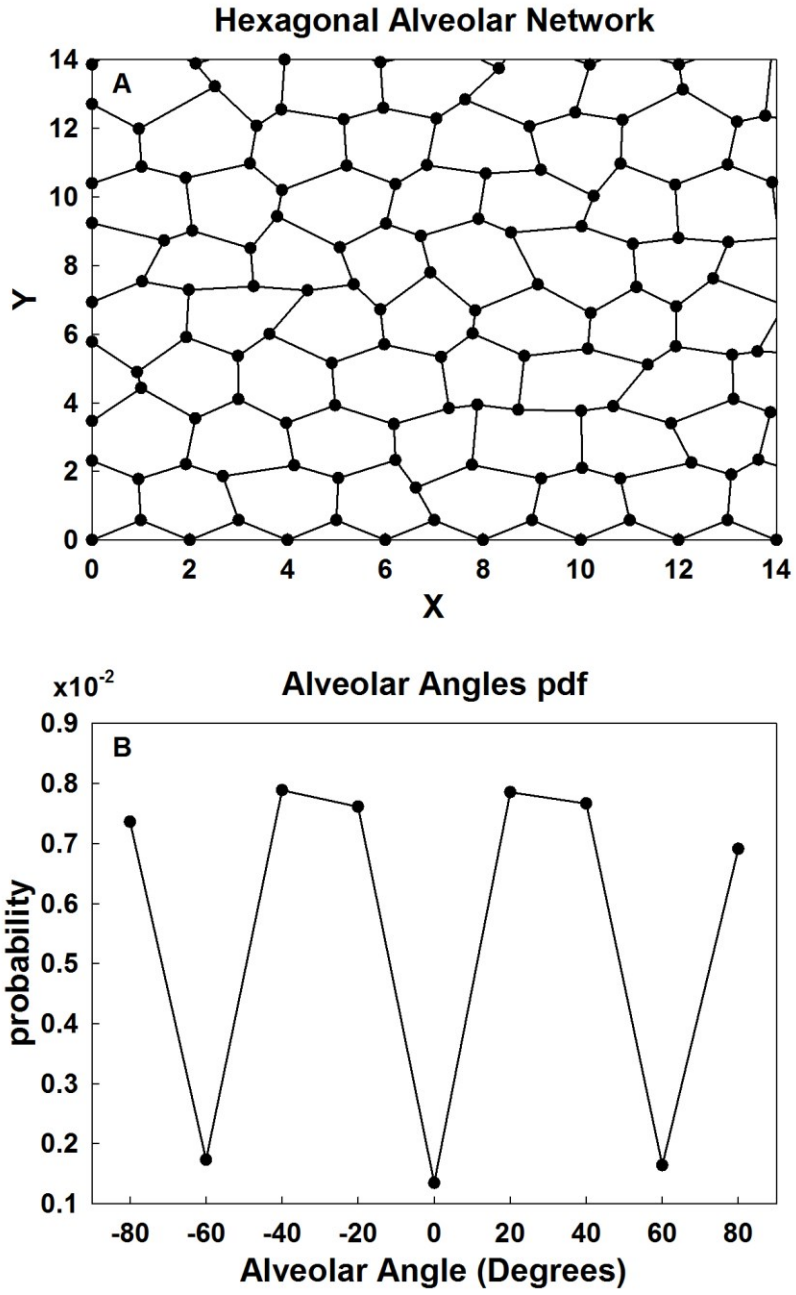

Figure D-3: Hexagonal network. A) Selected 14 x 14 alveolar region from a 180 x 30 network. B) Probability distribution function (pdf) of the initial alveolar angle distribution.

In brief, the network model by Cavalcante et al. [128] is a hexagonal network model which represents the alveoli where each side of the hexagon is an alveolar wall. Initially, a network of equal sided hexagons is created and then the angles are perturbed in order to form a heterogeneous network (Figure D-4). In particular, each alveolar wall represents a spring with a spring constant (k) and initial length (l_i), and the rotation of alveolar walls is captured by the bond-bending constant (b) such that the spring energy and the rotational energy are respectively:

$$E_k = \frac{k l_i^2 (\varepsilon)^2}{2} \tag{D.51}$$

$$E_b = \frac{b(\Delta\theta)^2}{2} \tag{D.52}$$

where ε is the strain on the spring and $\Delta\theta$ is the change in angle between two neighboring alveolar walls at a node. Thus, the total network energy (E_{nT}) is written as:

$$E_{nT} = \frac{1}{2} k l_i^2 \sum_{j=1}^{Springs} \varepsilon_j^2 + \frac{1}{2} b \sum_{i=1}^{Nodes} (\Delta\theta_j)^2 \tag{D.53}$$

At each tissue strain, the total network energy is minimized to find the new configuration instead of minimizing the energy of a single alveolar wall as in our model. Thus, unlike our model, the network includes interactions and does not assume affine transformations.

In the network model, the number of springs is N_s and the network's volume is defined as the number of hexagons N_h. For large network systems, the number of springs per hexagon (N_s/N_h) is equal to 3 [128]. In order to compare the network model and the current analytical model, we set $N_s = N$ and $N_h = uV_T$, where u [1/m^3] is a unity constant that will allow the correct dimensional analysis of both models. Furthermore, the initial

mean length of the springs which represents also the length of the alveolar walls in the model is $\bar{l}_i$.

In order to find the equation relating k to Y_{ae} and b to Y_{be} we equate the energies of a single hexagon in the numerical network model to that in the analytical uniaxial model. Consider a network formed with a homogenous pattern of regular equal-sided hexagons (Figure D-5). Assume that the hexagonal network is stretched uniaxially perpendicular to two parallel sides of the hexagons. Thus, for all hexagons, these two sides will not bend but the other four will bend producing a change of $\Delta\theta$ with the direction of stretch.

In order to find a relationship between k and Y_{ae}, we note that the strains are defined similarly in both models and the network accounts for all springs in calculating the energy yet sets the compressive strains to zero. The total linear spring energy of a hexagon ($E_{nh,k}$) is the number of springs per hexagon (N_s/N_h) multiplied by the spring energy of a single spring:

$$E_{nh,k} = \frac{N_s}{N_h}\frac{k\bar{l}_i^2(\varepsilon_s)^2}{2} \tag{D.54}$$

Noting that only 4 out of 6 walls/springs are stretching within each hexagon, the corresponding energy $E_{ah,k}$ for the analytical model is:

$$E_{ah,k} = 4\frac{Y_{ae}V_T(\varepsilon_s)^2}{2N} = 4\frac{N_h}{uN_s}\frac{Y_{ae}(\varepsilon_s)^2}{2} \tag{D.55}$$

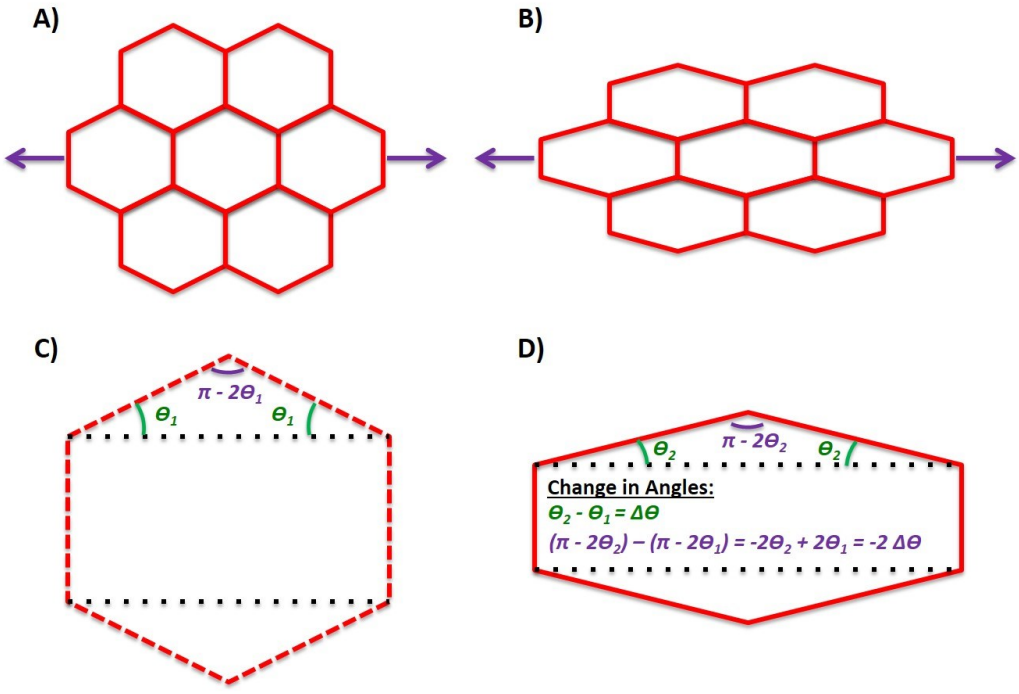

Figure D-4: Model comparison. A) A pattern of homogeneous hexagons stretched uniaxially. B) During stretch, the hexagons collapse laterally as 4 out of 6 sides rotate inwards and stretch while the other two compress inwards without any rotation. C) A hexagon before stretch has an acute angle of θ_1 between a rotating side and the direction of stretch. The obtuse angle between the two rotating sides is equal to π-2θ_1 D) After stretch these two angles become θ_1 and π-2θ_2 respectively. The change in angle is $\Delta\theta$ (θ_2-θ_1) and -2$\Delta\theta$ respectively.

Equating both energies:

$$4\frac{N_h}{uN_s}\frac{Y_{ae}(\varepsilon_s)^2}{2} = \frac{N_s}{N_h}\frac{k\bar{l}_i^2(\varepsilon_s)^2}{2} \tag{D.56}$$

$$Y_{ae} = u\left(\frac{N_s}{N_h}\right)^2\frac{1}{4}\bar{l}_i^2 k \cong u\frac{9}{4}\bar{l}_i^2 k \tag{D.57}$$

To obtain a relationship between b and Y_{be}, we note that the network applies the rotational energy at each node and thus has a different definition for $\Delta\theta$ than the analytic model (Figure D-5). The total rotational energy $E_{nh,b}$ of a hexagon in the network is:

$$E_{nh,b} = \left[4\frac{1}{2}b\Delta\theta^2 + 2\frac{1}{2}b(2\Delta\theta)^2\right] = 6b\Delta\theta^2 \tag{D.58}$$

Noting that only 4 out of 6 walls are rotating within each hexagon, our analytical model's corresponding rotating energy ($E_{ah,b}$) is equated as:

$$E_{ah,b} = \left(\frac{4}{6}\frac{N_s}{N_h}\right)\frac{1}{2}\frac{Y_{be}V_T}{N}\Delta\theta^2 = \frac{\Delta\theta^2}{3u}Y_{be} \tag{D.59}$$

Equating both energies:

$$\frac{\Delta\theta^2}{3u}Y_{be} = 6b\Delta\theta^2 \tag{D.60}$$

$$Y_{be} = u18b \tag{D.61}$$

Despite using a specific illustration to calculate the relationships in Eqs. D.57 and D.61, k, b, Y_{ae}, and Y_{be} are material properties independent of geometry and therefore the relationship is valid in all cases.

BIBLIOGRAPHY

[1] West JB. History of respiratory mechanics prior to World War II. Comprehensive Physiology 2012;2:609–619. doi:10.1002/cphy.c080112.

[2] Mitzner W. Mechanics of the lung in the 20th century. Comprehensive Physiology 2011;1:2009–2027. doi:10.1002/cphy.c100067.

[3] Oostveen E, MacLeod D, Lorino H, Farré R, Hantos Z, Desager K, et al. The forced oscillation technique in clinical practice: methodology, recommendations and future developments. European Respiratory Journal 2003;22:1026–1041. doi:10.1183/09031936.03.00089403.

[4] Nieman GF, Satalin J, Andrews P, Aiash H, Habashi NM, Gatto LA. Personalizing mechanical ventilation according to physiologic parameters to stabilize alveoli and minimize ventilator induced lung injury (VILI). Intensive Care Medicine Experimental 2017;5. doi:10.1186/s40635-017-0121-x.

[5] Carney D, DiRocco J, Nieman G. Dynamic alveolar mechanics and ventilator-induced lung injury. Critical Care Medicine 2005;33. doi:10.1097/01.CCM.0000155928.95341.BC.

[6] Mercer RR, Laco JM, Crapo JD. Three-dimensional reconstruction of alveoli in the rat lung for pressure-volume relationships. Journal of Applied Physiology 1987;62:1480–1487. doi:10.1152/jappl.1987.62.4.1480.

[7] Carney DE, Bredenberg CE, Schiller HJ, Picone AL, McCANN UG, Gatto LA, et al. The Mechanism of Lung Volume Change during Mechanical Ventilation. American Journal of Respiratory and Critical Care Medicine 1999;160:1697–1702. doi:10.1164/ajrccm.160.5.9812031.

[8] Namati E, Thiesse J, de Ryk J, McLennan G. Alveolar Dynamics during Respiration. American Journal of Respiratory Cell and Molecular Biology 2008;38:572–578. doi:10.1165/rcmb.2007-0120OC.

[9] Needham DM, Bronskill SE, Calinawan JR, Sibbald WJ, Pronovost PJ, Laupacis A. Projected incidence of mechanical ventilation in Ontario to 2026: Preparing for the aging baby boomers. Critical Care Medicine 2005;33:574–579.

[10] Meltzer MI, Patel A, Ajao A, Nystrom SV, Koonin LM. Estimates of the Demand for Mechanical Ventilation in the United States During an Influenza Pandemic. Clinical Infectious Diseases 2015;60:S52–57. doi:10.1093/cid/civ089.

[11] Pham T, Brochard LJ, Slutsky AS. Mechanical Ventilation: State of the Art. Mayo Clinic Proceedings 2017;92:1382–400. doi:10.1016/j.mayocp.2017.05.004.

[12] Lassen HCA. A preliminary report on the 1952 epidemic of poliomyelitis in Copenhagen with special reference to the treatment of acute respiratory insufficiency. Lancet (London, England) 1953;1:37–41.

[13] Engström C-G. Treatment of Severe Cases of Respiratory Paralysis by the Engström Universal Respirator. British Medical Journal 1954;2:666–669.

[14] Rubinson L, Vaughn F, Nelson S, Giordano S, Kallstrom T, Buckley T, et al. Mechanical ventilators in US acute care hospitals. Disaster Medicine and Public Health Preparedness 2010;4:199–206. doi:10.1001/dmp.2010.18.

[15] Chacko B, Peter JV, Tharyan P, John G, Jeyaseelan L. Pressure-controlled versus volume-controlled ventilation for acute respiratory failure due to acute lung injury (ALI) or acute respiratory distress syndrome (ARDS). The Cochrane Database of Systematic Reviews 2015;1:CD008807. doi:10.1002/14651858.CD008807.pub2.

[16] Hess DR. Approaches to Conventional Mechanical Ventilation of the Patient With Acute Respiratory Distress Syndrome. Respiratory Care 2011;56:1555–1572. doi:10.4187/respcare.01387.

[17] Zambon M, Vincent J-L. Mortality rates for patients with acute lung injury/ARDS have decreased over time. Chest 2008;133:1120–1127. doi:10.1378/chest.07-2134.

[18] Maca J, Jor O, Holub M, Sklienka P, Bur a F, Burda M, et al. Past and Present ARDS Mortality Rates: A Systematic Review. Respiratory Care 2017;62:113–122. doi:10.4187/respcare.04716.

[19] Bein T, Grasso S, Moerer O, Quintel M, Guerin C, Deja M, et al. The standard of care of patients with ARDS: ventilatory settings and rescue therapies for refractory hypoxemia. Intensive Care Medicine 2016;42:699–711. doi:10.1007/s00134-016-4325-4.

[20] Jash D, Chaudhry D, Bhutani J, Bg M, Chaudhry A. Ventilatory strategy in ARDS: Transpulmonary pressure vs conventional ARDS net protocol in management of ARDS. European Respiratory Journal 2018;52:PA328. doi:10.1183/13993003.congress-2018.PA328.

[21] Henriques I, Padilha GA, Huhle R, Wierzchon C, Miranda PJB, Ramos IP, et al. Comparison between Variable and Conventional Volume-Controlled Ventilation on Cardiorespiratory Parameters in Experimental Emphysema. Frontiers in Physiology 2016;7. doi:10.3389/fphys.2016.00277.

[22] Wang C, Wang X, Chi C, Guo L, Guo L, Zhao N, et al. Lung ventilation strategies for acute respiratory distress syndrome: a systematic review and network meta-analysis. Scientific Reports 2016;6. doi:10.1038/srep22855.

[23] Valipour A, Shah PL, Gesierich W, Eberhardt R, Snell G, Strange C, et al. Patterns of Emphysema Heterogeneity. Respiration; International Review of Thoracic Diseases 2015;90:402–411. doi:10.1159/000439544.

[24] Iotti GA, Braschi A, Brunner JX, Smits T, Olivei M, Palo A, et al. Respiratory mechanics by least squares fitting in mechanically ventilated patients: applications during paralysis and during pressure support ventilation. Intensive Care Medicine 1995;21:406–413.

[25] Brunner JX, Laubscher TP, Banner MJ, Iotti G, Braschi A. Simple method to measure total expiratory time constant based on the passive expiratory flow-volume curve. Critical Care Medicine 1995;23:1117–1122.

[26] Brunner JX, Langenstein H, Wolff G. A simple method for estimating compliance. Critical Care Medicine 1985;13:675–678.

[27] Lourens MS, van den Berg B, Aerts JG, Verbraak AF, Hoogsteden HC, Bogaard JM. Expiratory time constants in mechanically ventilated patients with and without COPD. Intensive Care Medicine 2000;26:1612–1618.

[28] Beydon N, Davis SD, Lombardi E, Allen JL, Arets HGM, Aurora P, et al. An Official American Thoracic Society/European Respiratory Society Statement: Pulmonary Function Testing in Preschool Children. American Journal of Respiratory and Critical Care Medicine 2007;175:1304–1345. doi:10.1164/rccm.200605-642ST.

[29] DuBois AB, Brody AW, Lewis DH, Burgess BF. Oscillation Mechanics of Lungs and Chest in Man. Journal of Applied Physiology 1956;8:587–594.

[30] Hantos Z, Daróczy B, Suki B, Galgóczy G, Csendes T. Forced oscillatory impedance of the respiratory system at low frequencies. Journal of Applied Physiology (Bethesda, Md: 1985) 1986;60:123–132. doi:10.1152/jappl.1986.60.1.123.

[31] Fredberg JJ, Stamenovic D. On the imperfect elasticity of lung tissue. Journal of Applied Physiology 1989;67:2408–2419. doi:10.1152/jappl.1989.67.6.2408.

[32] Fredberg JJ, Keefe DH, Glass GM, Castile RG, Frantz ID. Alveolar pressure nonhomogeneity during small-amplitude high-frequency oscillation. Journal of Applied Physiology: Respiratory, Environmental and Exercise Physiology 1984;57:788–800. doi:10.1152/jappl.1984.57.3.788.

[33] Bates JH, Ludwig MS, Sly PD, Brown K, Martin JG, Fredberg JJ. Interrupter resistance elucidated by alveolar pressure measurement in open-chest normal dogs. Journal of Applied Physiology 1988;65:408–414. doi:10.1152/jappl.1988.65.1.408.

[34] Lutchen KR, Hantos Z, Jackson AC. Importance of low-frequency impedance data for reliably quantifying parallel inhomogeneities of respiratory mechanics. IEEE Transactions on Biomedical Engineering 1988;35:472–481. doi:10.1109/10.2118.

[35] Hantos Z, Daroczy B, Suki B, Nagy S, Fredberg JJ. Input impedance and peripheral inhomogeneity of dog lungs. Journal of Applied Physiology 1992;72:168–78.

[36] Csorba Z, Petak F, Nevery K, Tolnai J, Balogh AL, Rarosi F, et al. Capnographic Parameters in Ventilated Patients: Correspondence with Airway and Lung Tissue Mechanics. Anesthesia & Analgesia 2016;122:1412. doi:10.1213/ANE.0000000000001185.

[37] Navajas D, Farré R. Forced oscillation assessment of respiratory mechanics in ventilated patients. Critical Care 2001;5:3. doi:10.1186/cc972.

[38] Babik B, Asztalos T, Peták F, Deák ZI, Hantos Z. Changes in Respiratory Mechanics During Cardiac Surgery. Anesthesia & Analgesia 2003;96:1280. doi:10.1213/01.ANE.0000055363.23715.40.

[39] LaPrad AS, Lutchen KR. Respiratory impedance measurements for assessment of lung mechanics: focus on asthma. Respiratory Physiology & Neurobiology 2008;163:64–73. doi:10.1016/j.resp.2008.04.015.

[40] Lefevre GR, Kowalski SE, Girling LG, Thiessen DB, Mutch WA. Improved arterial oxygenation after oleic acid lung injury in the pig using a computer-controlled mechanical ventilator. American Journal of Respiratory and Critical Care Medicine 1996;154:1567–1572. doi:10.1164/ajrccm.154.5.8912782.

[41] Rostig S, Kantelhardt JW, Penzel T, Cassel W, Peter JH, Vogelmeier C, et al. Nonrandom variability of respiration during sleep in healthy humans. Sleep 2005;28:411–417.

[42] Tobin MJ, Mador MJ, Guenther SM, Lodato RF, Sackner MA. Variability of resting respiratory drive and timing in healthy subjects. Journal of Applied Physiology 1988;65:309–317. doi:10.1152/jappl.1988.65.1.309.

[43] Brack T, Jubran A, Tobin MJ. Dyspnea and Decreased Variability of Breathing in Patients with Restrictive Lung Disease. American Journal of Respiratory and Critical Care Medicine 2002;165:1260–1264. doi:10.1164/rccm.2201018.

[44] Wysocki M, Cracco C, Teixeira A, Mercat A, Diehl J-L, Lefort Y, et al. Reduced breathing variability as a predictor of unsuccessful patient separation from mechanical ventilation. Critical Care Medicine 2006;34:2076–2083. doi:10.1097/01.CCM.0000227175.83575.E9.

[45] Amin SD, Majumdar A, Alkana P, Walkey AJ, O'Connor GT, Suki B. Modeling the effects of stretch-dependent surfactant secretion on lung recruitment during variable

ventilation. Journal of Biomedical Science and Engineering 2013;06:61. doi:10.4236/jbise.2013.612A008.

[46] Suki B, Alencar AM, Sujeer MK, Lutchen KR, Collins JJ, Andrade Jr JS, et al. Life-support system benefits from noise. Nature 1998;393:127–128. doi:10.1038/30130.

[47] Thammanomai A, Hueser LE, Majumdar A, Bartolák-Suki E, Suki B. Design of a new variable-ventilation method optimized for lung recruitment in mice. Journal of Applied Physiology 2008;104:1329–1340. doi:10.1152/japplphysiol.01002.2007.

[48] Mutch WA, Harms S, Lefevre GR, Graham MR, Girling LG, Kowalski SE. Biologically variable ventilation increases arterial oxygenation over that seen with positive end-expiratory pressure alone in a porcine model of acute respiratory distress syndrome. Critical Care Medicine 2000;28:2457–2464.

[49] Mutch WA, Eschun GM, Kowalski SE, Graham MR, Girling LG, Lefevre GR. Biologically variable ventilation prevents deterioration of gas exchange during prolonged anaesthesia. British Journal of Anaesthesia 2000;84:197–203.

[50] Bellardine CL, Hoffman AM, Tsai L, Ingenito EP, Arold SP, Lutchen KR, et al. Comparison of variable and conventional ventilation in a sheep saline lavage lung injury model. Critical Care Medicine 2006;34:439–445.

[51] Boker A, Graham MR, Walley KR, McManus BM, Girling LG, Walker E, et al. Improved arterial oxygenation with biologically variable or fractal ventilation using low tidal volumes in a porcine model of acute respiratory distress syndrome. American Journal of Respiratory and Critical Care Medicine 2002;165:456–462. doi:10.1164/ajrccm.165.4.2108006.

[52] Arold SP, Mora R, Lutchen KR, Ingenito EP, Suki B. Variable Tidal Volume Ventilation Improves Lung Mechanics and Gas Exchange in a Rodent Model of Acute Lung Injury. American Journal of Respiratory and Critical Care Medicine 2002;165:366–371. doi:10.1164/ajrccm.165.3.2010155.

[53] Berry CA, Suki B, Polglase GR, Pillow JJ. Variable ventilation enhances ventilation without exacerbating injury in preterm lambs with respiratory distress syndrome. Pediatric Research 2012;72:384–392. doi:10.1038/pr.2012.97.

[54] Arold SP, Suki B, Alencar AM, Lutchen KR, Ingenito EP. Variable ventilation induces endogenous surfactant release in normal guinea pigs. American Journal of Physiology Lung Cellular and Molecular Physiology 2003;285:L370-375. doi:10.1152/ajplung.00036.2003.

[55] Bartolák-Suki E, Noble PB, Bou Jawde S, Pillow JJ, Suki B. Optimization of Variable Ventilation for Physiology, Immune Response and Surfactant Enhancement in Preterm Lambs. Frontiers in Physiology 2017;8. doi:10.3389/fphys.2017.00425.

[56] Thammanomai A, Hamakawa H, Bartolák-Suki E, Suki B. Combined Effects of Ventilation Mode and Positive End-Expiratory Pressure on Mechanics, Gas Exchange and the Epithelium in Mice with Acute Lung Injury. PLoS ONE 2013;8:e53934. doi:10.1371/journal.pone.0053934.

[57] Güldner A, Huhle R, Beda A, Kiss T, Bluth T, Rentzsch I, et al. Periodic Fluctuation of Tidal Volumes Further Improves Variable Ventilation in Experimental Acute Respiratory Distress Syndrome. Frontiers in Physiology 2018;9. doi:10.3389/fphys.2018.00905.

[58] Fontela PC, Prestes RB, Forgiarini Jr. LA, Friedman G. Variable mechanical ventilation. Revista Brasileira de Terapia Intensiva 2017;29:77–86. doi:10.5935/0103-507X.20170012.

[59] Spieth PM, Carvalho AR, Pelosi P, Hoehn C, Meissner C, Kasper M, et al. Variable Tidal Volumes Improve Lung Protective Ventilation Strategies in Experimental Lung Injury. American Journal of Respiratory and Critical Care Medicine 2009;179:684–693. doi:10.1164/rccm.200806-975OC.

[60] Kiss T, Silva PL, Huhle R, Moraes L, Santos RS, Felix NS, et al. Comparison of different degrees of variability in tidal volume to prevent deterioration of respiratory system elastance in experimental acute lung inflammation. British Journal of Anaesthesia 2016;116:708–715. doi:10.1093/bja/aew093.

[61] Boker A, Haberman CJ, Girling L, Guzman RP, Louridas G, Tanner JR, et al. Variable ventilation improves perioperative lung function in patients undergoing abdominal aortic aneurysmectomy. Anesthesiology 2004;100:608–616.

[62] Spieth PM, Güldner A, Huhle R, Beda A, Bluth T, Schreiter D, et al. Short-term effects of noisy pressure support ventilation in patients with acute hypoxemic respiratory failure. Critical Care 2013;17:R261. doi:10.1186/cc13091.

[63] Wang R, Chen J, Wu G. Variable lung protective mechanical ventilation decreases incidence of postoperative delirium and cognitive dysfunction during open abdominal surgery. International Journal of Clinical and Experimental Medicine 2015;8:21208–21214.

[64] Smith BJ, Bates JHT. Variable Ventilation as a Diagnostic Tool for the Injured Lung. IEEE Transactions on Bio-Medical Engineering 2015;62:2106–2113. doi:10.1109/TBME.2014.2315964.

[65] Weibel ER. Morphometry of the Human Lung. Berlin Heidelberg: Springer-Verlag; 1963.

[66] Ochs M, Nyengaard JR, Jung A, Knudsen L, Voigt M, Wahlers T, et al. The Number of Alveoli in the Human Lung. American Journal of Respiratory and Critical Care Medicine 2004;169:120–124. doi:10.1164/rccm.200308-1107OC.

[67] Knudsen L, Ochs M. The micromechanics of lung alveoli: structure and function of surfactant and tissue components. Histochemistry and Cell Biology 2018;150:661–676. doi:10.1007/s00418-018-1747-9.

[68] Hamlington KL, Bates JHT, Roy GS, Julianelle AJ, Charlebois C, Suki B, et al. Alveolar leak develops by a rich-get-richer process in ventilator-induced lung injury. PLoS ONE 2018;13. doi:10.1371/journal.pone.0193934.

[69] Knudsen L, Lopez-Rodriguez E, Berndt L, Steffen L, Ruppert C, Bates JHT, et al. Alveolar Micromechanics in Bleomycin-induced Lung Injury. American Journal of Respiratory Cell and Molecular Biology 2018;59:757–769. doi:10.1165/rcmb.2018-0044OC.

[70] Kononov S, Brewer K, Sakai H, Cavalcante FS, Sabayanagam CR, Ingenito EP, et al. Roles of mechanical forces and collagen failure in the development of elastase-induced emphysema. American Journal of Respiratory and Critical Care Medicine 2001;164:1920–1926. doi:10.1164/ajrccm.164.10.2101083.

[71] Hansen JE, Ampaya EP. Human air space shapes, sizes, areas, and volumes. Journal of Applied Physiology 1975;38:990–995. doi:10.1152/jappl.1975.38.6.990.

[72] Lopez-Rodriguez E, Gay-Jordi G, Mucci A, Lachmann N, Serrano-Mollar A. Lung surfactant metabolism: early in life, early in disease and target in cell therapy. Cell and Tissue Research 2017;367:721–735. doi:10.1007/s00441-016-2520-9.

[73] Bachofen H, Schürch S. Alveolar surface forces and lung architecture. Comparative Biochemistry and Physiology Part A, Molecular & Integrative Physiology 2001;129:183–193.

[74] Andreassen S, Steimle KL, Mogensen ML, Serna JB de la, Rees S, Karbing DS. The effect of tissue elastic properties and surfactant on alveolar stability. Journal of Applied Physiology 2010;109:1369–1377. doi:10.1152/japplphysiol.00844.2009.

[75] Boccafoschi F, Bosetti M, Gatti S, Cannas M. Dynamic Fibroblast Cultures. Cell Adhesion & Migration 2007;1:124–128.

[76] Cui Y, Hameed FM, Yang B, Lee K, Pan CQ, Park S, et al. Cyclic stretching of soft substrates induces spreading and growth. Nature Communications 2015;6. doi:10.1038/ncomms7333.

[77] Bates JHT, Irvin CG. Measuring lung function in mice: the phenotyping uncertainty principle. Journal of Applied Physiology 2003;94:1297–1306. doi:10.1152/japplphysiol.00706.2002.

[78] Irvin CG, Bates JHT. Measuring the lung function in the mouse: the challenge of size. Respiratory Research 2003;4:4.

[79] Schuessler TF, Bates JHT, Maksym GN. Estimating tracheal flow in small animals. Proceedings of the 15th Annual International Conference of the IEEE Engineering in Medicine and Biology Society, 1993, p. 560–561. doi:10.1109/IEMBS.1993.978689.

[80] Schuessler TF, Bates JH. A computer-controlled research ventilator for small animals: design and evaluation. IEEE Transactions on Bio-Medical Engineering 1995;42:860–866. doi:10.1109/10.412653.

[81] Thammanomai A, Majumdar A, Bartolák-Suki E, Suki B. Effects of reduced tidal volume ventilation on pulmonary function in mice before and after acute lung injury. Journal of Applied Physiology 2007;103:1551–1559. doi:10.1152/japplphysiol.00006.2007.

[82] Giannella-Neto A, Bellido C, Barbosa RB, Melo MFV. Design and calibration of unicapillary pneumotachographs. Journal of Applied Physiology 1998;84:335–343.

[83] Korenberg MJ, Hunter IW. The identification of nonlinear biological systems: Volterra kernel approaches. Annals of Biomedical Engineering 1996;24:250–268.

[84] Mitzner W, Brown R, Lee W. In vivo measurement of lung volumes in mice. Physiological Genomics 2001;4:215–221.

[85] Vanoirbeek JAJ, Rinaldi M, De Vooght V, Haenen S, Bobic S, Gayan-Ramirez G, et al. Noninvasive and invasive pulmonary function in mouse models of obstructive and restrictive respiratory diseases. American Journal of Respiratory Cell and Molecular Biology 2010;42:96–104. doi:10.1165/rcmb.2008-0487OC.

[86] McGovern TK, Robichaud A, Fereydoonzad L, Schuessler TF, Martin JG. Evaluation of Respiratory System Mechanics in Mice using the Forced Oscillation Technique. JoVE: Journal of Visualized Experiments 2013:e50172–e50172. doi:10.3791/50172.

[87] Tang Y, Turner MJ, Yem JS, Baker AB. Calibration of pneumotachographs using a calibrated syringe. Journal of Applied Physiology 2003;95:571–576. doi:10.1152/japplphysiol.00196.2003.

[88] Korenberg MJ, Hunter IW. The identification of nonlinear biological systems: Wiener kernel approaches. Annals of Biomedical Engineering 1990;18:629–654. doi:10.1007/BF02368452.

[89] Rice J. A Theory of Condition. SIAM Journal on Numerical Analysis 1966;3:287–310. doi:10.1137/0703023.

[90] Suki B, Lutchen KR. Pseudorandom signals to estimate apparent transfer and coherence functions of nonlinear systems: applications to respiratory mechanics.

IEEE Transactions on Biomedical Engineering 1992;39:1142–1151. doi:10.1109/10.168693.

[91] Zehendner CM, Luhmann HJ, Yang J-W. A Simple and Novel Method to Monitor Breathing and Heart Rate in Awake and Urethane-Anesthetized Newborn Rodents. PLoS ONE 2013;8:e62628. doi:10.1371/journal.pone.0062628.

[92] Farré R, Navajas D, Peslin R, Rotger M, Duvivier C. A correction procedure for the asymmetry of differential pressure transducers in respiratory impedance measurements. IEEE Transactions on Bio-Medical Engineering 1989;36:1137–1140. doi:10.1109/10.40822.

[93] Peslin R, Jardin P, Duvivier C, Begin P. In-phase rejection requirements for measuring respiratory input impedance. Journal of Applied Physiology 1984;56:804–809.

[94] Thal SC, Plesnila N. Non-invasive intraoperative monitoring of blood pressure and arterial pCO2 during surgical anesthesia in mice. Journal of Neuroscience Methods 2007;159:261–267. doi:10.1016/j.jneumeth.2006.07.016.

[95] Fung YC. Biomechanics: Mechanical Properties of Living Tissues. 2nd ed. New York: Springer-Verlag; 1993.

[96] Bates JHT. Lung Mechanics by Jason H. T. Bates. Cambridge Core 2009. doi:10.1017/CBO9780511627156.

[97] Lutchen KR, Yang K, Kaczka DW, Suki B. Optimal ventilation waveforms for estimating low-frequency respiratory impedance. Journal of Applied Physiology 1993;75:478–488. doi:10.1152/jappl.1993.75.1.478.

[98] Daróczy B, Hantos Z. Generation of optimum pseudorandom signals for respiratory impedance measurements. International Journal of Bio-Medical Computing 1990;25:21–31.

[99] Kim CW, Kim JS, Park JW, Hong C-S. Clinical Applications of Forced Oscillation Techniques (FOT) in Patients with Bronchial Asthma. The Korean Journal of Internal Medicine 2001;16:80–86. doi:10.3904/kjim.2001.16.2.80.

[100] Eissa NT, Ranieri VM, Corbeil C, Chasse M, Robatto FM, Braidy J, et al. Analysis of behavior of the respiratory system in ARDS patients: effects of flow, volume, and time. Journal of Applied Physiology 1991;70:2719–2729. doi:10.1152/jappl.1991.70.6.2719.

[101] Spieth PM, Güldner A, Uhlig C, Bluth T, Kiss T, Conrad C, et al. Variable versus conventional lung protective mechanical ventilation during open abdominal surgery (PROVAR): a randomised controlled trial. British Journal of Anaesthesia 2018;120:581–591. doi:10.1016/j.bja.2017.11.078.

[102] Barnas GM, Mills PJ, Mackenzie CF, Fletcher SJ, Green MD. Effect of Tidal Volume on Respiratory System Elastance and Resistance during Anesthesia and Paralysis. American Review of Respiratory Disease 1992;145:522–526. doi:10.1164/ajrccm/145.3.522.

[103] Bates JHT, Shardonofsky F, Stewart DE. The low-frequency dependence of respiratory system resistance and elastance in normal dogs. Respiration Physiology 1989;78:369–382. doi:10.1016/0034-5687(89)90111-4.

[104] Zimmermann SC, Watts JC, Bertolin A, Jetmalani K, King GG, Thamrin C. Discrepancy between in vivo and in vitro comparisons of forced oscillation devices. Journal of Clinical Monitoring and Computing 2018;32:509–512. doi:10.1007/s10877-017-0050-y.

[105] Dellacà RL, Zannin E, Kostic P, Andersson Olerud M, Pompilio PP, Hedenstierna G, et al. Optimisation of positive end-expiratory pressure by forced oscillation technique in a lavage model of acute lung injury. Intensive Care Medicine 2011;37:1021. doi:10.1007/s00134-011-2211-7.

[106] Zannin E, Dellaca RL, Kostic P, Pompilio PP, Larsson A, Pedotti A, et al. Optimizing positive end-expiratory pressure by oscillatory mechanics minimizes tidal recruitment and distension: an experimental study in a lavage model of lung injury. Critical Care 2012;16:R217. doi:10.1186/cc11858.

[107] Szlavecz A, Chiew YS, Redmond D, Beatson A, Glassenbury D, Corbett S, et al. The Clinical Utilisation of Respiratory Elastance Software (CURE Soft): a bedside software for real-time respiratory mechanics monitoring and mechanical ventilation management. BioMedical Engineering OnLine 2014;13. doi:10.1186/1475-925X-13-140.

[108] Lutchen KR, Gillis H. Relationship between heterogeneous changes in airway morphometry and lung resistance and elastance. Journal of Applied Physiology 1997;83:1192–1201. doi:10.1152/jappl.1997.83.4.1192.

[109] Eidelman DH, Ghezzo H, Kim WD, Hyatt RE, Cosio MG. Pressure-Volume Curves in Smokers: Comparison with Alpha-1-Antitrypsin Deficiency. American Review of Respiratory Disease 1989;139:1452–1458. doi:10.1164/ajrccm/139.6.1452.

[110] Harris RS. Pressure-volume curves of the respiratory system. Respiratory Care 2005;50:78–98; discussion 98-99.

[111] Oliveira CLN, Araújo AD, Bates JHT, Andrade JSJ, Suki B. Entropy Production and the Pressure–Volume Curve of the Lung. Frontiers in Physiology 2016;7. doi:10.3389/fphys.2016.00073.

[112] Jonson B, Richard J-C, Straus C, Mancebo J, Lemaire F, Brochard L. Pressure–Volume Curves and Compliance in Acute Lung Injury. American Journal of

Respiratory and Critical Care Medicine 1999;159:1172–1178. doi:10.1164/ajrccm.159.4.9801088.

[113] Suki B, Stamenovic D, Hubmayr R. Lung Parenchymal Mechanics. Comprehensive Physiology 2011;1:1317–1351. doi:10.1002/cphy.c100033.

[114] Abraham T, Hogg J. Extracellular matrix remodeling of lung alveolar walls in three dimensional space identified using second harmonic generation and multiphoton excitation fluorescence. Journal of Structural Biology 2010;171:189–196. doi:10.1016/j.jsb.2010.04.006.

[115] Pena A-M, Fabre A, Débarre D, Marchal-Somme J, Crestani B, Martin J-L, et al. Three-dimensional investigation and scoring of extracellular matrix remodeling during lung fibrosis using multiphoton microscopy. Microscopy Research and Technique 2007;70:162–170. doi:10.1002/jemt.20400.

[116] Suki B, Bates JHT. Extracellular matrix mechanics in lung parenchymal diseases. Respiratory Physiology & Neurobiology 2008;163:33–43. doi:10.1016/j.resp.2008.03.015.

[117] Mercer RR, Crapo JD. Spatial distribution of collagen and elastin fibers in the lungs. Journal of Applied Physiology 1990;69:756–765. doi:10.1152/jappl.1990.69.2.756.

[118] Suki B, Bates JHT. Lung tissue mechanics as an emergent phenomenon. Journal of Applied Physiology 2011;110:1111–1118. doi:10.1152/japplphysiol.01244.2010.

[119] Suki B, Ito S, Stamenović D, Lutchen KR, Ingenito EP. Biomechanics of the lung parenchyma: critical roles of collagen and mechanical forces. Journal of Applied Physiology 2005;98:1892–1899. doi:10.1152/japplphysiol.01087.2004.

[120] Alexander H. Tensile instability of initially spherical balloons. International Journal of Engineering Science 1971;9:151–160. doi:10.1016/0020-7225(71)90017-6.

[121] Xin-chun S. Tensile instability of nonlinear spherical membrane with large deformation. Applied Mathematics and Mechanics 1991;12:993–1000. doi:10.1007/BF02451485.

[122] Clements JA, Hustead RF, Johnson RP, Gribetz I. Pulmonary surface tension and alveolar stability. Journal of Applied Physiology 1961;16:444–450. doi:10.1152/jappl.1961.16.3.444.

[123] Gil J, Bachofen H, Gehr P, Weibel ER. Alveolar volume-surface area relation in air- and saline-filled lungs fixed by vascular perfusion. Journal of Applied Physiology 1979;47:990–1001. doi:10.1152/jappl.1979.47.5.990.

[124] Gehr P, Bachofen M, Weibel ER. The normal human lung: ultrastructure and morphometric estimation of diffusion capacity. Respiration Physiology 1978;32:121–140. doi:10.1016/0034-5687(78)90104-4.

[125] Mercer RR, Russell ML, Crapo JD. Alveolar septal structure in different species. Journal of Applied Physiology 1994;77:1060–6. doi:10.1152/jappl.1994.77.3.1060.

[126] Lutfi MF. The physiological basis and clinical significance of lung volume measurements. Multidisciplinary Respiratory Medicine 2017;12. doi:10.1186/s40248-017-0084-5.

[127] Sugihara T, Martin CJ, Hildebrandt J. Length-tension properties of alveolar wall in man. Journal of Applied Physiology 1971;30:874–878. doi:10.1152/jappl.1971.30.6.874.

[128] Cavalcante FSA, Ito S, Brewer K, Sakai H, Alencar AM, Almeida MP, et al. Mechanical interactions between collagen and proteoglycans: implications for the stability of lung tissue. Journal of Applied Physiology 2005;98:672–679. doi:10.1152/japplphysiol.00619.2004.

[129] Karrobi K, Tank A, Tabassum S, Pera V, Roblyer D. Diffuse and nonlinear imaging of multiscale vascular parameters for in vivo monitoring of preclinical mammary tumors. Journal of Biophotonics n.d.;0:e201800379. doi:10.1002/jbio.201800379.

[130] Schindelin J, Arganda-Carreras I, Frise E, Kaynig V, Longair M, Pietzsch T, et al. Fiji: an open-source platform for biological-image analysis. Nature Methods 2012;9:676–682. doi:10.1038/nmeth.2019.

[131] Edwards YS. Stretch stimulation: its effects on alveolar type II cell function in the lung. Comparative Biochemistry and Physiology Part A, Molecular & Integrative Physiology 2001;129:245–260.

[132] Sanchez-Esteban J, Cicchiello LA, Wang Y, Tsai S-W, Williams LK, Torday JS, et al. Mechanical stretch promotes alveolar epithelial type II cell differentiation. Journal of Applied Physiology 2001;91:589–595. doi:10.1152/jappl.2001.91.2.589.

[133] Arold SP, Bartolák-Suki E, Suki B. Variable stretch pattern enhances surfactant secretion in alveolar type II cells in culture. American Journal of Physiology-Lung Cellular and Molecular Physiology 2009;296:L574–581. doi:10.1152/ajplung.90454.2008.

[134] Desai LP, Chapman KE, Waters CM. Mechanical stretch decreases migration of alveolar epithelial cells through mechanisms involving Rac1 and Tiam1. American Journal of Physiology - Lung Cellular and Molecular Physiology 2008;295:L958–965. doi:10.1152/ajplung.90218.2008.

[135] Roan E, Waters CM. What do we know about mechanical strain in lung alveoli? American Journal of Physiology-Lung Cellular and Molecular Physiology 2011;301:L625–635. doi:10.1152/ajplung.00105.2011.

[136] Sherratt MJ, Baldock C, Haston JL, Holmes DF, Jones CJP, Shuttleworth CA, et al. Fibrillin microfibrils are stiff reinforcing fibres in compliant tissues. Journal of Molecular Biology 2003;332:183–193.

[137] Dutov P, Antipova O, Varma S, Orgel JPRO, Schieber JD. Measurement of Elastic Modulus of Collagen Type I Single Fiber. PLoS ONE 2016;11:e0145711. doi:10.1371/journal.pone.0145711.

[138] Guthold M, Liu W, Sparks EA, Jawerth LM, Peng L, Falvo M, et al. A Comparison of the Mechanical and Structural Properties of Fibrin Fibers with Other Protein Fibers. Cell Biochemistry and Biophysics 2007;49:165–181. doi:10.1007/s12013-007-9001-4.

[139] Sherebrin MH, Song SH, Roach MR. Mechanical anisotropy of purified elastin from the thoracic aorta of dog and sheep. Canadian Journal of Physiology and Pharmacology 1983;61:539–545.

[140] Maksym GN, Bates JHT. A distributed nonlinear model of lung tissue elasticity. Journal of Applied Physiology 1997;82:32–41. doi:10.1152/jappl.1997.82.1.32.

[141] Haut RC, Little RW. A constitutive equation for collagen fibers. Journal of Biomechanics 1972;5:423–430. doi:10.1016/0021-9290(72)90001-2.

[142] Gattinoni L, Pesenti A. The concept of "baby lung." Intensive Care Medicine 2005;31:776–784. doi:10.1007/s00134-005-2627-z.

[143] Watkins J, Mathieson I. CHAPTER 4 - Connective tissues. In: Watkins J, Mathieson I, editors. Pocket Podiatry Guide Funct. Anat., Edinburgh: Churchill Livingstone; 2009, p. 107–156. doi:10.1016/B978-0-7020-3032-1.00004-4.

[144] Smith JC, Stamenovic D. Surface forces in lungs. I. Alveolar surface tension-lung volume relationships. Journal of Applied Physiology 1986;60:1341–1350. doi:10.1152/jappl.1986.60.4.1341.

[145] Szapiel SV, Fulmer JD, Hunninghake GW, Elson NA, Kawanami O, Ferrans VJ, et al. Hereditary emphysema in the tight-skin (Tsk/+) mouse. The American Review of Respiratory Disease 1981;123:680–685. doi:10.1164/arrd.1981.123.6.680.

[146] Ito S, Bartolák-Suki E, Shipley JM, Parameswaran H, Majumdar A, Suki B. Early Emphysema in the Tight Skin and Pallid Mice: Roles of Microfibril-Associated Glycoproteins, Collagen, and Mechanical Forces. American Journal of Respiratory Cell and Molecular Biology 2006;34:688–694. doi:10.1165/rcmb.2006-0002OC.

[147] D'Errico A, Scarani P, Colosimo E, Spina M, Grigioni WF, Mancini AM. Changes in the alveolar connective tissue of the ageing lung: An immunohistochemical study. Virchows Archiv A Pathological Anatomy and Histopathology 1989;415:137–144. doi:10.1007/BF00784351.

[148] Michel R, Zwikler M, Bates JHT. Effect of severe experimental fibrosis on lung resistance and elastance. American Review of Respiratory Disease 1993;147:A595.

[149] O'Donnell MD, O'Connor CM, FitzGerald MX, Lungarella G, Cavarra E, Martorana PA. Ultrastructure of lung elastin and collagen in mouse models of spontaneous emphysema. Matrix Biology 1999;18:357–360. doi:10.1016/S0945-053X(99)00031-1.

[150] Matsuda M, Fung YC, Sobin SS. Collagen and elastin fibers in human pulmonary alveolar mouths and ducts. Journal of Applied Physiology 1987;63:1185–1194. doi:10.1152/jappl.1987.63.3.1185.

[151] Reiser KM, Hennessy SM, Last JA. Analysis of age-associated changes in collagen crosslinking in the skin and lung in monkeys and rats. Biochimica et Biophysica Acta (BBA) - General Subjects 1987;926:339–348. doi:10.1016/0304-4165(87)90220-0.

[152] Last JA, King TE, Nerlich AG, Reiser KM. Collagen Cross-linking in Adult Patients with Acute and Chronic Fibrotic Lung Disease: Molecular Markers for Fibrotic Collagen. American Review of Respiratory Disease 1990;141:307–313. doi:10.1164/ajrccm/141.2.307.

[153] Suki B, Bartolák-Suki E. Biomechanics of the Aging Lung Parenchyma. In: Derby B, Akhtar R, editors. Mech. Prop. Aging Soft Tissues, Cham: Springer International Publishing; 2015, p. 95–133. doi:10.1007/978-3-319-03970-1_5.

[154] Yuan H, Kononov S, Cavalcante FSA, Lutchen KR, Ingenito EP, Suki B. Effects of collagenase and elastase on the mechanical properties of lung tissue strips. Journal of Applied Physiology 2000;89:3–14. doi:10.1152/jappl.2000.89.1.3.

[155] Wilson TA, Bachofen H. A model for mechanical structure of the alveolar duct. Journal of Applied Physiology 1982;52:1064–1070. doi:10.1152/jappl.1982.52.4.1064.

[156] Schürch S, Goerke J, Clements JA. Direct determination of surface tension in the lung. Proceedings of the National Academy of Sciences of the United States of America 1976;73:4698–4702.

[157] Yamamoto N. Tensile Strength of Single Collagen Fibrils Isolated from Tendons. European Journal of Biophysics 2017;5:1. doi:10.11648/j.ejb.20170501.11.

[158] Shen ZL, Dodge MR, Kahn H, Ballarini R, Eppell SJ. Stress-Strain Experiments on Individual Collagen Fibrils. Biophysical Journal 2008;95:3956–3963. doi:10.1529/biophysj.107.124602.

[159] Mijailovich SM, Stamenovic D, Fredberg JJ. Toward a kinetic theory of connective tissue micromechanics. Journal of Applied Physiology 1993;74:665–681. doi:10.1152/jappl.1993.74.2.665.

[160] Wuyts FL, Vanhuyse VJ, Langewouters GJ, Decraemer WF, Raman ER, Buyle S. Elastic properties of human aortas in relation to age and atherosclerosis: A structural model. Physics in Medicine and Biology 1995;40:1577–1597.

[161] Lanir Y. A structural theory for the homogeneous biaxial stress-strain relationships in flat collagenous tissues. Journal of Biomechanics 1979;12:423–436.

[162] Liao H, Belkoff SM. A failure model for ligaments. Journal of Biomechanics 1999;32:183–188.

[163] Decraemer WF, Maes MA, Vanhuyse VJ. An elastic stress-strain relation for soft biological tissues based on a structural model. Journal of Biomechanics 1980;13:463–468.

[164] Sacks MS. Incorporation of experimentally-derived fiber orientation into a structural constitutive model for planar collagenous tissues. Journal of Biomechanical Engineering 2003;125:280–287.

[165] Ritter MC, Jesudason R, Majumdar A, Stamenovic D, Buczek-Thomas JA, Stone PJ, et al. A zipper network model of the failure mechanics of extracellular matrices. Proceedings of the National Academy of Sciences of the United States of America 2009;106:1081–1086. doi:10.1073/pnas.0808414106.

[166] Black LD, Brewer KK, Morris SM, Schreiber BM, Toselli P, Nugent MA, et al. Effects of elastase on the mechanical and failure properties of engineered elastin-rich matrices. Journal of Applied Physiology 2005;98:1434–1441. doi:10.1152/japplphysiol.00921.2004.

[167] Maksym GN, Fredberg JJ, Bates JHT. Force heterogeneity in a two-dimensional network model of lung tissue elasticity. Journal of Applied Physiology 1998;85:1223–1229. doi:10.1152/jappl.1998.85.4.1223.

[168] Takahashi A, Majumdar A, Parameswaran H, Bartolák-Suki E, Suki B. Proteoglycans maintain lung stability in an elastase-treated mouse model of emphysema. American Journal of Respiratory Cell and Molecular Biology 2014;51:26–33. doi:10.1165/rcmb.2013-0179OC.

[169] Maroudas A, Bannon C. Measurement of swelling pressure in cartilage and comparison with the osmotic pressure of constituent proteoglycans. Biorheology 1981;18:619–632.

[170] Chalmers GW, Gosline JM, Lillie MA. The hydrophobicity of vertebrate elastins. The Journal of Experimental Biology 1999;202:301–14.

[171] Shiwen X, Stratton R, Nikitorowicz-Buniak J, Ahmed-Abdi B, Ponticos M, Denton C, et al. A Role of Myocardin Related Transcription Factor-A (MRTF-A) in Scleroderma Related Fibrosis. PLoS ONE 2015;10. doi:10.1371/journal.pone.0126015.

[172] Huang K, Mitzner W, Rabold R, Schofield B, Lee H, Biswal S, et al. Variation in senescent-dependent lung changes in inbred mouse strains. Journal of Applied Physiology 2007;102:1632–1639. doi:10.1152/japplphysiol.00833.2006.

[173] Toshima M, Ohtani Y, Ohtani O. Three-dimensional architecture of elastin and collagen fiber networks in the human and rat lung. Archives of Histology and Cytology 2004;67:31–40. doi:10.1679/aohc.67.31.

[174] Brewer KK, Sakai H, Alencar AM, Majumdar A, Arold SP, Lutchen KR, et al. Lung and alveolar wall elastic and hysteretic behavior in rats: effects of in vivo elastase treatment. Journal of Applied Physiology (Bethesda, Md: 1985) 2003;95:1926–1936. doi:10.1152/japplphysiol.00102.2003.

[175] Snedeker JG, Gautieri A. The role of collagen crosslinks in ageing and diabetes - the good, the bad, and the ugly. Muscles, Ligaments and Tendons Journal 2014;4:303–308.

[176] Knudson RJ, Clark DF, Kennedy TC, Knudson DE. Effect of aging alone on mechanical properties of the normal adult human lung. Journal of Applied Physiology 1977;43:1054–1062. doi:10.1152/jappl.1977.43.6.1054.

[177] Thurlbeck WM. The Internal Surface Area of Nonemphysematous Lungs. American Review of Respiratory Disease 1967;95:765–773. doi:10.1164/arrd.1967.95.5.765.

[178] Polio SR, Kundu AN, Dougan CE, Birch NP, Aurian-Blajeni DE, Schiffman JD, et al. Cross-platform mechanical characterization of lung tissue n.d.:17.

[179] Liu F, Tschumperlin DJ. Micro-Mechanical Characterization of Lung Tissue Using Atomic Force Microscopy. JoVE: Journal of Visualized Experiments 2011. doi:10.3791/2911.

[180] Aaron BB, Gosline JM. Elastin as a random-network elastomer: A mechanical and optical analysis of single elastin fibers. Biopolymers 1981;20:1247–1260. doi:10.1002/bip.1981.360200611.

[181] Mead J. Mechanical Properties of Lungs. Physiological Reviews 1961;41:281–330. doi:10.1152/physrev.1961.41.2.281.

[182] Hantos Z, Suki B, Csendes T, Daroczy B. Constant-phase modelling of pulmonary tissue impedance. Bulletin Européen de Physiopathologie Respiratoire 1987;23.

CURRICULUM VITAE